



## **Terms and Conditions of Use of Digitised Theses from Trinity College Library Dublin**

### **Copyright statement**

All material supplied by Trinity College Library is protected by copyright (under the Copyright and Related Rights Act, 2000 as amended) and other relevant Intellectual Property Rights. By accessing and using a Digitised Thesis from Trinity College Library you acknowledge that all Intellectual Property Rights in any Works supplied are the sole and exclusive property of the copyright and/or other IPR holder. Specific copyright holders may not be explicitly identified. Use of materials from other sources within a thesis should not be construed as a claim over them.

A non-exclusive, non-transferable licence is hereby granted to those using or reproducing, in whole or in part, the material for valid purposes, providing the copyright owners are acknowledged using the normal conventions. Where specific permission to use material is required, this is identified and such permission must be sought from the copyright holder or agency cited.

### **Liability statement**

By using a Digitised Thesis, I accept that Trinity College Dublin bears no legal responsibility for the accuracy, legality or comprehensiveness of materials contained within the thesis, and that Trinity College Dublin accepts no liability for indirect, consequential, or incidental, damages or losses arising from use of the thesis for whatever reason. Information located in a thesis may be subject to specific use constraints, details of which may not be explicitly described. It is the responsibility of potential and actual users to be aware of such constraints and to abide by them. By making use of material from a digitised thesis, you accept these copyright and disclaimer provisions. Where it is brought to the attention of Trinity College Library that there may be a breach of copyright or other restraint, it is the policy to withdraw or take down access to a thesis while the issue is being resolved.

### **Access Agreement**

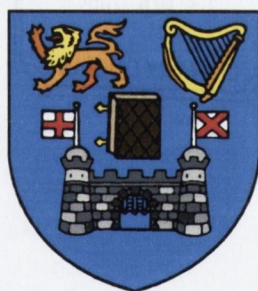
By using a Digitised Thesis from Trinity College Library you are bound by the following Terms & Conditions. Please read them carefully.

I have read and I understand the following statement: All material supplied via a Digitised Thesis from Trinity College Library is protected by copyright and other intellectual property rights, and duplication or sale of all or part of any of a thesis is not permitted, except that material may be duplicated by you for your research use or for educational purposes in electronic or print form providing the copyright owners are acknowledged using the normal conventions. You must obtain permission for any other use. Electronic or print copies may not be offered, whether for sale or otherwise to anyone. This copy has been supplied on the understanding that it is copyright material and that no quotation from the thesis may be published without proper acknowledgement.

**Electron-Hole Excitations  
and  
Optical Spectra  
of Rare Gas Solids**

Svjetlana Galamić-Mulaomerović

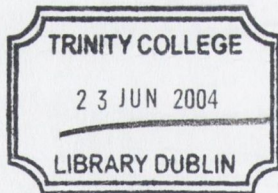
A Thesis submitted to  
The University of Dublin  
Trinity College  
for the degree of  
Doctor of Philosophy



DEPARTMENT OF PHYSICS  
TRINITY COLLEGE  
UNIVERSITY OF DUBLIN

February 2004

©S. Galamić-Mulaomerović & University of Dublin



THESIS  
8037  
7549

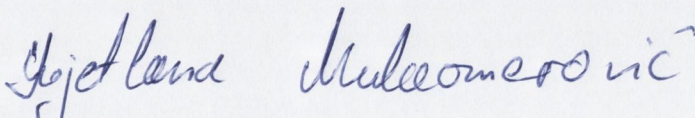
## Declaration

This thesis is submitted by the undersigned to the University of Dublin for examination for the degree of Doctor of Philosophy.

This thesis has not been submitted as an exercise for a degree to any other university.

With the exceptions of the assistance noted in the acknowledgments, this thesis is entirely my own work.

I agree that the Library of the University of Dublin may lend or copy this thesis upon request.



Svjetlana Galamić-Mulaomerović

February 2004

Dublin

## Acknowledgements

I would like to thank everyone that has supported me during this work:

Foremost, I am extremely grateful to my supervisor, Dr. Charles Patterson for his continual guidance and support, for taking an active interest in all aspects of this research, for all his ideas and suggestions that made this work possible and for his patience with me in lieu of frustration.

This work would never be so successful without the scientific support and suggestions I received from my colleagues, Dr. Conor Hogan and Dr. Michael Kuzmin, and for that I am very grateful. I am indebted to Prof. Nicholas Harrison and Prof. Vic Saunders for letting me to change their CRYSTAL code and helping me with that. I would also like to acknowledge Dr. Donal Mackernan and Andrew Rowan for some proof-reading. I owe my thanks to Dr. Simon Cox, Dr. Simon Elliot and Dr. Marco Nicastro for discussions on various scientific issues.

Many thanks to the staff of Trinity Center for High Performance Computing, in particular Dr. Geoff Bradley and Robert Crosbie for much help and advice with computational matters and for providing me with extra accounts and CPU time on their computer facilities. I would also like to thank to my husband, Ernad for his professional advises with programming issues.

For financial support I would like to acknowledge the following Enterprise Ireland grants: SC/99/255 on "Numerical study of excitons and plasmons in materials" and SC/00/267 on "Electronic structure of strongly correlated materials manganites and cuprates".

Many thanks to my husband for all his support and encouragements, especially at times when things did not work very well and to my daughter as she was source of my motivation. I would also like to use this opportunity to apologize them for many nights and weekends they had to spend in my absence. I wish to thank to my parents for all their support during my education, and to my parents-in-law for their encouragement.

Finally, thanks to all inhabitants of the lab over the years for living up the place: Wiebke, Lorenzo, Andrew, James, Gemma, Joanne, Garry, Paul, Donal, Nikos, Lola, Marco, Gosia, Przemek, Finn, Conor, Geoff, Michael, Simon E., Simon C., Sadhbh, and Kate.

## List of Publications

1. M. Nicastro, S. Galamić-Mulaomerović and C. H. Patterson, *Multipolar contributions to electron self-energies: extreme tight binding model*. J. Phys.: Condens. Matter **13**, 1212-1231 (2001).
2. S. Galamić-Mulaomerović C. H. Patterson, *Eigenfunctions of the Inverse Dielectric Functions and Response Functions of Silicon and Argon*, Phys. Stat. Sol. (a) **188**, No. 4. 1291-1296 (2001)
3. S. Galamić-Mulaomerović and C. H. Patterson *Optical spectra of rare gas solids* - in preparation

## Summary

This thesis is a theoretical study of the optical and dielectric properties of semiconductors and insulators. The quantity that defines the relationship between measurable optical properties and electronic structure of materials is the macroscopic dielectric function  $\epsilon_{\alpha\beta}(\mathbf{q}, \omega)$ . The aim of this thesis is accurate calculation and interpretation of the longitudinal dielectric function by highly reliable *ab initio* techniques. In order to achieve this, two types of excitations of an electronic system are relevant: single-particle excitations and electron-hole excitations. The key concept in our approach is to describe these excitations with the corresponding one- and two-particle Green's functions. A recently developed approach, which combines three computational techniques, was employed in the study. Firstly, density functional and Hartree-Fock methods were used in ground state calculations to generate non-interacting single-particle Green's functions. In the second step, single-particle excitations were studied using the *GW* approximation to the electron self-energy operator. Finally, the electron-hole interaction was calculated and a Bethe-Salpeter equation solved, leading to coupled electron-hole excitations. This approach allows bound exciton states to be studied and entire optical spectra calculated. In addition, the influence of local field effects and single-particle excitations was examined separately. The importance of including both single-particle and electron-hole excitations in calculations of the dielectric function is highlighted.

Ground state calculations were carried out using density functional theory for silicon and rare gas solids: neon, argon, krypton and xenon. The Hartree-Fock method was used for the calculation of non-interacting Green's functions of  $\text{Cu}_2\text{O}$ . The formalism adopted in these calculations is the linear combination of atomic orbitals (LCAO) scheme, in which the electronic Bloch functions are expressed in a basis of localised Gaussian orbitals.

The reliability of *GW* calculations within LCAO approach is carefully checked by comparing calculated band structure for Si with earlier calculations and experimental data. Comparison is made between all-electron Gaussian orbital basis sets and our pseudopotential calculation for Si. Both types of basis sets gave accurate band structures for

the states around the band gap. The valence band width was described very accurately by the all electron basis set for Si. A detailed analysis of the *GW* band structure is given for the rare gas solids. The *GW* self-energy correction improved DFT band structures in all rare gas solids yielding band gaps and valence band widths in very good agreement with experimental data. The *GW* self-energy calculation was applied to  $\text{Cu}_2\text{O}$  and significant improvement of the Hartree-Fock band structure was obtained, however quantitative agreement with the experimental band structure was not achieved due to exaggerated Hartree-Fock eigenvalues.

Two-particle excitations and optical spectra are given for Si and the rare gas solids. It is shown that inclusion of local field effects and quasiparticle energies yields poor agreement with experimental spectra for all materials studied. Inclusion of the electron-hole interaction (excitonic effects) in optical properties calculations improved agreement between the computed macroscopic dielectric functions and experimental data. It is also shown that local field effects may correct energy loss functions and improve agreement with experiment at a higher energies.





# Contents

<b>1</b>	<b>Introduction</b>	<b>1</b>
<b>2</b>	<b>Many-Body Perturbation Theory</b>	<b>5</b>
2.1	What is the many-body problem? . . . . .	5
2.2	Hartree and Hartree-Fock Theories . . . . .	6
2.3	Density Functional Theory . . . . .	7
2.4	Green's Function Techniques . . . . .	9
<b>3</b>	<b>Theory of Single-Particle Excitations</b>	<b>13</b>
3.1	Hedin's Equations . . . . .	13
3.2	Quasiparticles . . . . .	15
3.3	The <i>GW</i> Approximation . . . . .	16
3.3.1	<i>GW</i> -DFT . . . . .	17
3.3.2	<i>GW</i> -HFA . . . . .	18
3.4	Basis Sets . . . . .	19
3.5	The Self-Energy Matrix Element . . . . .	21
3.5.1	Plasmon-pole model . . . . .	22
3.6	Determination of Quasiparticle Energies . . . . .	27
3.7	Beyond $G_0W_0$ . . . . .	28
<b>4</b>	<b>Quasiparticle Band Structure of Bulk Materials</b>	<b>31</b>
4.1	<i>GW</i> -DFT Calculations . . . . .	31
4.1.1	Details of the DFT-LDA calculation . . . . .	32
4.1.2	Details of the <i>GW</i> calculation . . . . .	34

4.1.3	Results for Si . . . . .	37
4.1.4	Results for rare gas solids . . . . .	43
4.2	Quasiparticle band structure for $\text{Cu}_2\text{O}$ . . . . .	50
4.2.1	Crystal structure . . . . .	51
4.2.2	Self-energy calculation . . . . .	52
4.2.3	Results . . . . .	53
<b>5</b>	<b>Optical Spectra and Electron-Hole Excitations</b>	<b>57</b>
5.1	Linear Dielectric Response . . . . .	58
5.2	The Bethe-Salpeter Equation . . . . .	61
5.3	The Electron-Hole Interaction Kernel . . . . .	64
5.4	The Spin Structure of the Excitons . . . . .	65
5.5	Optical Spectra . . . . .	67
5.6	Numerical Details . . . . .	69
<b>6</b>	<b>Calculation of the Optical Properties in Bulk Materials</b>	<b>71</b>
6.1	Convergence Parameters . . . . .	72
6.1.1	RPA calculation . . . . .	72
6.1.2	Exciton calculation . . . . .	72
6.2	Calculated Optical Spectra and Local Field Effects . . . . .	74
6.3	Optical Spectrum for Si . . . . .	77
6.4	Macroscopic Dielectric Function and Exciton Effects of RGS . . . . .	79
6.4.1	Neon . . . . .	80
6.4.2	Argon . . . . .	82
6.4.3	Krypton . . . . .	85
6.4.4	Xenon . . . . .	87
6.4.5	Summary . . . . .	89
6.5	Electron-hole wave functions for Argon . . . . .	91
6.6	The Static Dielectric Constant . . . . .	93
6.7	Electron Energy Loss Function . . . . .	96

<b>7</b>	<b>Conclusions</b>	<b>99</b>
7.1	Single-particle Excitations . . . . .	99
7.2	Electron-hole Correlation and Optical Spectra . . . . .	100
7.3	Outlook . . . . .	102
<b>A</b>	<b>Computer Code Manual</b>	<b>105</b>
A.1	User Guide . . . . .	105
A.1.1	Getting Started . . . . .	106
A.1.2	Preliminary tasks . . . . .	108
A.1.3	General input task . . . . .	110
A.1.4	Optional Blocks . . . . .	113
A.2	Programming Guidelines . . . . .	124
A.2.1	The code structure . . . . .	124
A.2.2	User defined data types . . . . .	128
A.2.3	Global data . . . . .	130
<b>B</b>	<b>Static RPA Dielectric Matrix</b>	<b>135</b>
B.1	Dielectric Band Structure . . . . .	135
B.2	The RPA Response Function and Local Field Effects . . . . .	137
B.3	Convergence Parameters . . . . .	137
B.4	Results and Discussion . . . . .	140
<b>C</b>	<b>Gaussian Orbital Basis Set</b>	<b>145</b>
C.1	Optical Properties and GO Basis Set . . . . .	145
C.2	Optimisation and Basis Set Tables . . . . .	150



# List of Figures

3.1	Dielectric matrix: plasmon-pole model vs. direct calculation for Si at $\mathbf{q} \rightarrow 0$ limit. . . . .	25
3.2	Dielectric matrix: plasmon-pole model vs. direct calculation for Si in the L point. . . . .	26
3.3	Same as Figure 3.1 for Ar. . . . .	26
3.4	Same as Figure 3.3, at the L point. . . . .	27
3.5	Diagrammatic expansion for the self-energy operator. . . . .	29
4.1	The $GW$ and LDA band structure for Silicon. . . . .	38
4.2	Convergence of the band gaps for Si with respect to the number of conduction bands . . . . .	41
4.3	Dynamic self-energy matrix element for Si at $\Gamma$ point . . . . .	42
4.4	The $GW$ and LDA band structure for Ne, Ar, Kr and Xe . . . . .	45
4.5	Calculated band gap energies (in eV) for the RGS (symbols) vs. experimental values . . . . .	49
4.6	Theoretical energies (in eV) at $L'_{2v}$ for the RGS compared with experiment . . . . .	50
4.7	Crystal structure of $\text{Cu}_2\text{O}$ . . . . .	52
4.8	Electronic band structure for $\text{Cu}_2\text{O}$ : Hartree-Fock and $GW$ . . . . .	53
4.9	Electronic valence band structure for $\text{Cu}_2\text{O}$ . . . . .	55
5.1	Feynman diagrams of the irreducible electron-hole interaction $\Xi$ . . . . .	64
6.1	RPA $\epsilon_2$ for Si as a function of photon energy . . . . .	74
6.2	RPA absorption spectra for the rare gas solids . . . . .	75

6.3	Local field effects in $\epsilon_2$ for solid Ar . . . . .	76
6.4	$\epsilon_2$ for Si as a function of photon energy:excitonic effects included . . . . .	78
6.5	The macroscopic dielectric function for FCC Ne: excitonic effects included	81
6.6	The macroscopic dielectric function for solid Ar with excitonic effects included . . . . .	83
6.7	The macroscopic dielectric function for solid Kr with excitonic effects included . . . . .	86
6.8	Macroscopic dielectric function for solid Xe . . . . .	88
6.9	Real space distribution of the first electron-hole wave function for Ar . . . . .	90
6.10	Same as Figure 6.9 along the lines . . . . .	91
6.11	Energy loss spectra for Ne, Ar and Kr, RPA and experiment . . . . .	97
A.1	The computational flow of smexciton executable . . . . .	107
A.2	Computational flow of the preliminary task. . . . .	109
B.1	DBS for bulk Si and FCC Ar . . . . .	141
B.2	The most screened dielectric eigenpotentials for Si at $\mathbf{q} \rightarrow 0$ . . . . .	142
B.3	The response eigenfunctions which correspond to eigenpotentials dis- played at Figure B.2 . . . . .	143
B.4	Three the most screened dielectric eigenpotentials and corresponding re- sponse eigenfunctions at $\mathbf{q} \rightarrow 0$ for Ar . . . . .	144
C.1	Energy eigenvalues as a function of conduction band number for different basis sets for Si . . . . .	147
C.2	As Figure C.1 for $\text{Cu}_2\text{O}$ . . . . .	147
C.3	Energy eigenvalues vs. conduction band number for the RGS. . . . .	148
C.4	Convergence of the Dielectric constant and some selected dielectric ma- trix elements with respect to the number of conduction bands for 52 AO basis set . . . . .	149
C.5	As Figure C.4 for the largest, 88 AO all electron basis set for Si. . . . .	150

# List of Tables

4.1	Experimental lattice constants in Å. . . . .	33
4.2	Auxiliary functions, $g(\mathbf{q})$ and their integrals over the Brillouin zone for the cubic lattices . . . . .	36
4.3	Calculated LDA eigenenergies at points of high symmetry for Si. . . . .	39
4.4	Calculated $GW$ quasiparticle energies at points of high symmetry for Si. . . . .	40
4.5	Quasiparticle energies at high-symmetry points for solid neon . . . . .	46
4.6	Quasiparticle energies (eV) at high-symmetry points for solid Ar . . . . .	46
4.7	Quasiparticle energies (eV) at high-symmetry points for solid Kr . . . . .	47
4.8	LDA and $GW$ energies (eV) at high-symmetry points for solid Xe . . . . .	47
4.9	Hartree-Fock (HF) and $GW$ energies for $\text{Cu}_2\text{O}$ . . . . .	55
6.1	Energy positions of the maxima detected in $\epsilon_2(\omega)$ of solid Ne . . . . .	81
6.2	Energy positions of the maxima detected in $\epsilon_2(\omega)$ for triplet and singlet excitons in solid Ar . . . . .	84
6.3	Peak positions detected in $\epsilon_2(\omega)$ for triplet and singlet excitons in solid Kr . . . . .	87
6.4	peak positions detected in $\epsilon_2(\omega)$ for triplet and singlet excitons in solid Xe . . . . .	89
6.5	The Static dielectric constant, $\epsilon_0$ for different materials . . . . .	94
6.6	Convergence of $\epsilon_0$ for Ar and Kr with respect to $N_c$ and $N_k$ including excitonic effects. . . . .	96
6.7	Energy loss function - calculated (RPA) and measured peak positions for solid Ne, Ar and Kr . . . . .	98
A.1	Output files written by CRYSTAL95 used to generate the auxiliary input file Crystal.data. . . . .	110



A.2	Notation used in the description of the input data. . . . .	111
A.3	List of the task identification optional keywords. . . . .	114
B.1	Selected elements of DM for Si calculated using different basis sets . . .	138
B.2	Convergence of some selected DM elements and dielectric constant with respect to the number of <b>k</b> -points . . . . .	139
B.3	Convergence of the dielectric constant for different materials with respect to the size of the dielectric matrix . . . . .	140
B.4	Smallest inverse eigenvalues of $\epsilon_{\mathbf{G}\mathbf{G}'}(\mathbf{q} \rightarrow 0)$ . . . . .	140

# Chapter 1

## Introduction

The interaction of light with matter, manifested in optical spectra, plays a central role in physics and chemistry. Optical spectra are used to characterise and manipulate materials and they form basis for a vast variety of spectroscopic methods and technological applications. On this basis, a detailed understanding and calculation of excited electronic states in materials and corresponding optical spectra are of great importance. Calculated spectral data can help to interpret experimental spectra, to develop a more detailed understanding of the structure of materials and identify some specific features in the structure e.g. defect levels. This is particularly important for novel materials under specific conditions e.g. high pressure, and for systems that are of technological interest such as light-emitting devices, opto-electronic applications, or photovoltaics. Moreover, spectral data allow for the identification of fundamental physical processes in the electronic structure of materials and for careful analysis and understanding of interaction, correlation and coupling effects in the electronic system.

The quantity that defines the relationship between the measurable optical properties and electronic structure of materials is the macroscopic dielectric function,  $\epsilon_{\alpha\beta}(\mathbf{q}, \omega)$ . The aim of this thesis is accurate calculation and interpretation of the longitudinal dielectric function by highly reliable *ab initio* techniques. In order to achieve this, two types of excitations of an electronic system are relevant: single-particle excitations and electron-hole excitations. The electron-hole excitations are formed from the quasiparticles (single-particle excitations) due to electron-hole correlation effects. They correspond to the transition of the  $N$ -electron system from the ground state to an excited state. The

excitations interact with external electromagnetic fields and so they are of central importance for the optical properties of the system. These include the absorption and emission of light from individual excited states—excitons and linear optical response from all photon energies, excluding the infrared range where the spectra is dominated by phonons. Both types of excitations, quasiparticles and electron-hole are described by many-body perturbation theory, expressed in terms of equations of motion for corresponding Green's functions.

The main advantage of many-body perturbation theory is that it reduces the unsolvable many-body problem to an effective one- or two-particle problem, where all many-body processes are included in an effective interaction kernel. In most cases, the interaction kernel cannot be calculated exactly, and reliable approximations ought to be employed. Accurate description of single-particle excitations and corresponding spectrum requires approximation of electron self-energy which includes all exchange and correlation effects. One very successful approach is given by Hedin's *GW* approximation [1]. The *GW* method has turned out to yield very accurate quasiparticle energies in excellent agreement with experimental data [2, 3, 4, 5, 6, 7] and become a standard tool for predicting quasiparticle band structure. The electron-hole excitations are due to two-particle correlation and so they are described by two-particle Green's functions. These are given as solutions of the Bethe-Salpeter equation (BSE) [8]. Solving BSE involves calculation of an electron-hole interaction kernel. In the current approach the interaction kernel is given in basis of quasiparticle states.

The key concept of the present approach is the systematic inclusion of the single-particle excitations and electron-hole interaction in the calculation of the dielectric function. A major achievement of the approach lies in its realisation within *ab initio* framework, going far beyond the empirical techniques employed in the past. The approach was introduced by Hanke and Sham [9, 10] more than two decades ago, however due to its computationally complex nature it had been limited to simple situations until recently. The approach allows systematic investigation of a role of two-particle correlation effects in different classes of materials ranging from single atoms and molecules to crys-

tals. In implementation adopted in this work, proposed by several groups [11, 12, 13], calculation is contained from the three major successive steps: (1) Firstly, the ground state calculation is performed using either the density functional theory (DFT) with local density approximation (LDA) or Hartree-Fock approximation (HFA) then the 'non-interacting' single-particle Green's functions were generated from DFT (HFA). (2) In the second step, the non-interacting single-particle Green's functions are employed to generate self-energy operator and then the quasiparticle states were determined by solving corresponding equation of motion. (3) Finally, electron-hole interaction kernel can be calculated and BSE solved yielding electron-hole excitations (transition energies, electron-hole wave function) and macroscopic dielectric function is obtained which provides absorption spectrum, dielectric constant, reflectivity, etc.

This thesis is organised as follows: Chapter 2 introduces the reader in the many-body problem and outlines the fundamental concepts behind the *ab initio* formalism: The Hartree approach, which neglects all exchange and correlation effects, the Hartree-Fock theory and finally modern and efficient density functional theory which has become a standard tool for ground state calculations. The latter two were used in the present context. The chapter concludes with general definitions of one- and two-particle Green's functions in the limit of zero temperature.

Chapter 3 gives detailed formalism of single-particle Green's function calculation. Hedin's equations and a definition of quasiparticles are presented in the chapter. The chapter gives detailed formalism on *GW* self-energy calculations and numerical aspects of the calculations such as basis set and plasmon-pole model. Some remarks on the self-consistent *GW* calculations are given in the final section of the chapter. Some practical applications of the *GW* theory are presented in Chapter 4. The approach is applied to semiconductors and wide gap insulators. Comparison with experimental data and earlier calculations is presented where available.

Introduction to linear dielectric response and dielectric function is presented in Chapter 5. Formalism for two-particle correlation function and Bethe-Salpeter equation is

presented in detail as well as numerical aspects of the macroscopic dielectric function calculation with and without electron-hole interaction included. Optical properties for various materials are presented in Chapter 6. The chapter begins with brief discussion of optical spectra within the random phase approximation (RPA) optical and investigate influence of local field effects, then continues with optical spectra with electron-hole interaction included. This order was chosen to highlight importance of the electron-hole interaction in the optical properties of the studied materials. The electron-hole wave functions, static dielectric constant and energy loss spectra are discussed as well in the chapter. Finally, Chapter 7 summarizes all conclusions and gives a short proposal for possible future work.

Some additional relevant information is provided in several appendices. These include in the first place manual of the computer code which was developed as a part of this project. The manual is written in order to provide guidelines for future users and to aid further development. The manual is presented in Appendix A. RPA dielectric matrix calculation and its graphical representation in a form of the dielectric band structure (DBS) and eigenpotentials and response function eigenvectors are presented in Appendix B. Finally Gaussian orbital basis set applicability and optimisation are discussed in Appendix C. The appendix provides the tables of basis sets used in the calculations.

## Chapter 2

# Many-Body Perturbation Theory

### 2.1 What is the many-body problem?

The  $N$ -electron system is described by the Hamiltonian<sup>1</sup>

$$H = \sum_{i=1}^N \left[ -\frac{\hbar^2}{2m} \nabla^2(\mathbf{r}_i) + V(\mathbf{r}_i) \right] + \frac{e^2}{2} \sum_{i \neq j}^N \frac{1}{|\mathbf{r}_i - \mathbf{r}_j|} \quad (2.1)$$

where  $V$  is a local external potential such as the field from a nucleus in an atom or the periodic potential of the ion cores in a solid. The last term in the Hamiltonian is the long range Coulomb interaction which ensures that each electron interacts with many others in its neighbourhood. This form of the Hamiltonian provides a rigorous starting point for the calculation of many-electron properties for non-relativistic interactions. Relativistic effects are negligible for most of the calculations carried out in this work. It is clear that this Hamiltonian presents a problem which is too complicated to solve directly, unless the number of electrons is very small. Fortunately, most physical properties do not require the full information of the many-particle wave-function, but can be described by correlation functions that involve the physics of only one or two particles. The key idea of many-body perturbation theory is to transform the many-particle problem into an equation of motion for such few-particle correlation functions, thus the many-body problem would lead to a single or two-particle problem. All many-particle effects would be included in corresponding interaction kernel.

---

<sup>1</sup>The form of the Hamiltonian given here treats the nuclei as if they are fixed and neglects their kinetic energy and Coulomb repulsion term between nuclei. This approximation is known as the Born-Oppenheimer approximation.

One and two particle correlation functions are defined by Green's functions, which are the central quantities of many-body perturbation theory. Special attention is given to them in the Section 2.4 and Chapter 3. In the next two sections, different *ab initio* schemes for the approximation of the Coulomb electron-electron term of the Hamiltonian (2.1) with a single-particle potential are outlined.

## 2.2 Hartree and Hartree-Fock Theories

The earliest of these theories was suggested by Hartree [14] (1928). He suggested that an effective potential energy for the electron is determined by the average motion of the other electrons. In that approximation the many-electron wave function is expressed as a product of single-particle functions, i.e.,

$$\Psi(\mathbf{r}_1, \mathbf{r}_2, \dots) = \psi_1(\mathbf{r}_1) \psi_2(\mathbf{r}_2) \dots \quad (2.2)$$

Each of the functions  $\psi_\lambda(\mathbf{r}_\lambda)$  satisfies one electron Schrödinger equation:

$$H \psi_\lambda = E_\lambda \psi_\lambda \quad (2.3)$$

$$H = -\frac{\hbar^2}{2m} \nabla^2 + V(\mathbf{r}) + V_H(\mathbf{r}) \quad (2.4)$$

$$V_H(\mathbf{r}) = e^2 \int \frac{d\mathbf{r}' n(\mathbf{r}')}{|\mathbf{r} - \mathbf{r}'|} \quad (2.5)$$

where  $n(\mathbf{r})$  is the density

$$n(\mathbf{r}) = \sum_i^{occ} |\psi_i(\mathbf{r})|^2$$

of all electrons in the system. This approximation is known as the *Hartree approximation*. The Coulomb interaction is now replaced by an average local Coulomb potential,  $V_H$  (Hartree potential). While the approximation is computationally simple and intuitively attractive, it does not produce reasonable results in many cases. One of the problems with the Hartree approximation is that the density of electrons includes the electron whose wave function,  $\psi_\lambda$  is being calculated. This means that that electron is included in the Hartree potential, so it is interacting with itself.

Fock [15] (1930) pointed out that the Hartree approximation does not take the fermionic nature of the electrons into account. Antisymmetric many-electron wave functions give

rise to an extra potential in equation (2.3) which is called *exchange* and the equation then becomes:

$$\left[-\frac{\hbar^2}{2m}\nabla^2 + V(\mathbf{r}) + V_H(\mathbf{r})\right]\psi_\lambda + \sum_{\lambda',\sigma'=\sigma} V_{\lambda\lambda'}(\mathbf{r})\psi_{\lambda'}(\mathbf{r}) = E_\lambda\psi_\lambda. \quad (2.6)$$

The notation  $\sigma' = \sigma$  means that the sum runs only over states with parallel spin.  $V_{\lambda\lambda'}(\mathbf{r})$  is the Hartree-Fock exchange term:

$$V_{\lambda\lambda'}(\mathbf{r}) = -e^2 \int \frac{d\mathbf{r}'}{|\mathbf{r} - \mathbf{r}'|} \psi_{\lambda'}^\dagger(\mathbf{r}')\psi_\lambda(\mathbf{r}'). \quad (2.7)$$

The exchange potential ensures that the Pauli exclusion principle is satisfied. This approximation has been called the *Hartree-Fock approximation* (HFA). The physical meaning of equation (2.6) is clear, an electron is moving in an average potential which is a sum of three terms: A potential due to the ions or nucleus, a potential corresponding to the classical Coulomb interaction between the electron and the average electronic charge density and a nonlocal exchange potential which arises due to the fermionic nature of the electrons. Equations (2.6) and (2.7) are solved self-consistently.

For many atomic systems, the Hartree-Fock approximation works quite well. However, for insulating solids the fundamental energy gap is generally overestimated by the approximation. This is essentially due to neglect of the the polarisability of the surrounding electronic gas that produces correlation or screening, which is not too important in atoms, but crucial in solids. Two electrons of opposite spin are allowed to occupy the same single-particle state at the cost of the large Coulomb energy. Correlation keeps electrons away from each other, creating a screening hole around each electron, which reduces the interaction with the other electrons and decreases the Coulomb energy. Thus correlation or screening reduces the gap from its Hartree-Fock value.

## 2.3 Density Functional Theory

An alternative approach that includes both, exchange and correlation effects in the Hamiltonian is density functional theory (DFT). DFT was originally introduced by Hohenberg and Kohn 1964 [16] and Kohn and Sham 1965 [17]. Since then, it has become the standard method for the calculation of ground-state properties of both molecules and solids



in modern solid state physics. Some recent reviews on DFT can be found in [18] and [19]. DFT is based upon two theorems:

1. The electron density  $n(\mathbf{r})$  in the ground state is a functional of the external potential  $V(\mathbf{r})$
2. The potential  $V(\mathbf{r})$  is a unique functional (to within a constant) of the density  $n(\mathbf{r})$ .

Both theorems were proved in [16], and together they are equivalent to the assertion that the ground state energy,  $E_G$  is a minimum with respect to variations in the electron density  $n(\mathbf{r})$ . Using the variational property of the energy functional,

$$\frac{\delta E}{\delta n} = \mu \quad (2.8)$$

and introducing a set of Kohn-Sham orbitals,  $\phi_\lambda$ , one arrives at a set of single-particle equations, the Kohn-Sham equations [17] :

$$\left[-\frac{\hbar^2}{2m}\nabla^2 + V_H(\mathbf{r}) + V_{xc}(\mathbf{r})\right]\phi_\lambda = \varepsilon_\lambda \phi_\lambda \quad (2.9)$$

where the non-interacting Hartree and kinetic energy parts of the potential have been separated out to leave an effective exchange-correlation potential  $V_{xc}(\mathbf{r})$ .  $\mu$  in (2.8) is the Lagrange multiplier associated with the requirement of constant particle number and is actually the chemical potential.

In practice, the potential containing exchange and correlation effects is not known exactly. As an approximation to the full exchange-correlation potential, Kohn and Sham in [17] applied a simple local density approximation (LDA) to the limiting case of a slowly varying density. In LDA, the exchange-correlation energy is given by:

$$E_{xc}^{LDA}[n] = \int d\mathbf{r} n(\mathbf{r}) \varepsilon_{xc}[n] \quad (2.10)$$

$$V_{xc} = \frac{\delta E_{xc}^{LDA}[n]}{\delta n(\mathbf{r})} \quad (2.11)$$

where  $\varepsilon_{xc}[n]$  is the exchange and correlation energy per particle of a homogeneous electron gas with density  $n$ . Although Kohn and Sham did not attempt to use this approximation in atoms, molecules or solids, as they did not expect it to work accurately in

electron interacting systems, a decade later it was shown that the LDA could reproduce many measurable quantities satisfactorily in such systems. The connection between this limiting non-interacting system and a real physical system is rigorously given by the condition that the Kohn-Sham density of the ground state matches the actual density of the system exactly:

$$n^{KS}(\mathbf{r}) = n^{real}(\mathbf{r}) = \sum_i^{occ} |\phi_i(\mathbf{r})|^2 \quad (2.12)$$

It is necessary to satisfy conditions (2.10-2.12), and this is achieved in a self-consistent procedure.

The solution of this system of equations leads then to the energy and density of the ground state, and all quantities derivable from them. Instead of seeking those quantities by determining the wave function of the system of interacting electrons, DFT within the framework of LDA, reduces the problem exactly to the solution of a single-particle equation. Equation (2.9) is an equation of the Hartree-Fock form, where the non-local Hartree-Fock exchange potential,  $V_{ex}$ , is replaced now by a *local*  $V_{xc}$ . Within a local approximation to  $E_{xc}$ , the Kohn-Sham equations present the same numerical simplicities as Hartree's equations (2.3).

The Kohn-Sham equation (2.9) applies only to the ground-state, and KS eigenvalues  $\epsilon_i$  have no clear physical meaning, except for the highest occupied eigenenergy which corresponds to the ionization energy [20]. Although there is no theoretical justification, they are often interpreted as single-particle excitation energies corresponding to the excitation spectra of the system upon a removal or adding of an electron, even if the DFT-LDA energy gap is underestimated by about 50% [18]. Nevertheless, the KS eigenenergies and orbitals are a good starting point for Green's function theory [2], and they are used throughout this thesis in that context.

## 2.4 Green's Function Techniques

The central quantities of many-body perturbation theory are Green's functions, which describe the propagation of electrons and holes in the electronic system. Single-particle,  $G_1$ , and two-particle,  $G_2$ , Green's functions will be of particular interest in the present

work. They are defined as the expectation values of the time-ordered operator products [21]:

$$G_1(1, 2) = -i\langle N, 0|T(\hat{\psi}(1)\hat{\psi}^\dagger(2))|N, 0\rangle, \quad (2.13)$$

$$G_2(12; 1'2') = -i\langle N, 0|T(\hat{\psi}(1)\hat{\psi}(2)\hat{\psi}^\dagger(1')\hat{\psi}^\dagger(2'))|N, 0\rangle. \quad (2.14)$$

The short-hand notation  $(1) \equiv (\mathbf{r}_1, \sigma_1, t_1)$  indicates a set of spatial, spin and temporal coordinates.  $|N, 0\rangle$  denotes the normalised ground-state wavefunction of  $N$ -electron system in the Heisenberg representation,  $T$  is Wick's time-ordering operator that rearranges the subsequent symbols in ascending order from left to right and  $\hat{\psi}^\dagger$  and  $\hat{\psi}$  are the electron creation and annihilation operators in the Heisenberg representation, respectively. The above definitions of Green's functions are valid only for zero temperature.

Single-particle Green's functions describe the propagation of an added electron to the ground state or of the remaining hole when an electron is removed i.e.:

$$|N, 0\rangle \longrightarrow |N \pm 1, m\rangle,$$

where  $|N \pm 1, m\rangle$  denotes an excited states of the  $(N + 1)$  and  $(N - 1)$ -electron system. The type of particle depends on the order of the time variables  $t_1$  and  $t_2$ . Two-particle Green's functions describe the propagation of pairs of particles: pairs of electrons, pairs of holes or an electron-hole pair, depending on the order of the four time variables. In the present work we will restrict ourselves to the simultaneous creation and annihilation of an electron-hole pair. In that case,  $G_2$  describes the transition from the ground state of the  $N$ -electron system to the higher state without changing the total number of electrons,

$$|N, 0\rangle \longrightarrow |N, m\rangle$$

and the four time variables are reduced to two since  $t_1 = t'_1$  and  $t_2 = t'_2$ .

The Green's function ( $G_1$  or  $G_2$ ) can generally be obtained as a solution of a Dyson-type equation schematically written as

$$G = G^{(0)} + G^{(0)}KG \quad (2.15)$$

In the traditional approach,  $G_1^{(0)}$  corresponds to the Green's function of a non-interacting electron and  $K$  is a self-energy operator, describing exchange and correlation effects.

Alternatively (see Section 3.3),  $G_1^{(0)}$  can be computed from a method that already includes some exchange and correlation effects in a simple self-energy  $K^{(0)}$  (such as DFT or HFA). The interaction kernel in (2.15),  $K$  is then replaced by a difference between the total self-energy  $K$  and  $K^{(0)}$ .

For a case of two-particle Green's functions,  $G_2^{(0)}$  is approximated by a product of two single-particle Green's functions which corresponds to a non-interacting pair of particles and  $K$  denotes an effective particle-particle interaction. It should be noted that an exact evaluation of  $K$  is not possible. Instead, appropriate approximations have been introduced for real systems taking all relevant many-body physics into account. The approximations are still very complex and both mathematically and computationally difficult to evaluate. Therefore, treatment of real materials is only possible if powerful computers and efficient algorithms are available. The construction and implementation of such approximations and their application to various materials is the subject of this work.



# Chapter 3

## Theory of Single-Particle Excitations

### 3.1 Hedin's Equations

Single-particle excitations and their spectra can be calculated from the single-particle Green's function  $G_1$  defined by the Equation (2.13).  $G_1$  is rigorously given by the dynamical equation [1]

$$\begin{aligned} & \left\{ i\hbar \frac{\partial}{\partial t} - H(\mathbf{r}) \right\} G_1(\mathbf{x}t, \mathbf{x}'t') + \\ & i \int v(\mathbf{r}, \mathbf{r}'') \langle N, 0 | T(\hat{\psi}^\dagger(\mathbf{x}'', t) \hat{\psi}(\mathbf{x}'', t) \hat{\psi}(\mathbf{x}, t) \hat{\psi}^\dagger(\mathbf{x}', t')) | N, 0 \rangle d\mathbf{x}'' = \\ & = \delta(\mathbf{x}, \mathbf{x}') \delta(t, t'). \end{aligned} \quad (3.1)$$

where  $H(\mathbf{r})$  is a local single particle Hamiltonian, which is, traditionally, given by the Hartree Hamiltonian (2.4),

$$H = -\frac{\hbar^2}{2m} \nabla^2 + V(\mathbf{r}) + V_H(\mathbf{r}). \quad (3.2)$$

The notation  $\mathbf{x}$  in Equation (3.1) stands for space and spin coordinates,  $(\mathbf{r}, \sigma)$  and  $v(\mathbf{r}, \mathbf{r}'')$  is the Coulomb potential. The matrix element with a four field operator product in the second term of the equation is a special case of the two-particle Green's function,  $G_2$ , originally defined by Equation (2.14). Equation (3.1) thus forms the starting point of an infinite series of dynamical equations, each of which involves the Green's function of a higher order. Clearly, a truncation has to be introduced at some point.

The product of the four field operators in (3.1) can, however, be generated by a functional derivative of  $G_1$ , [1]. In addition, Hedin defined the electron self-energy operator

$\Sigma$  in terms of the functional derivative in [1], which finally leads to the equation

$$\left\{ i\hbar \frac{\partial}{\partial t} - H(\mathbf{r}) \right\} G_1(1, 2) - \int \Sigma(1, 3) G_1(3, 2) d(3) = \delta(1, 2) \quad (3.3)$$

Unlike the  $G_2$  appearing in (3.1), the self-energy operator  $\Sigma(1, 3)$  depends on two sets of coordinates only and it does not contain all information contained in  $G_2$  but yet contains all many-particle information which is relevant for the single-particle Green's function. Thus Equation (3.3) is still an exact equation of motion for  $G_1$ .

The self-energy operator  $\Sigma(1, 3)$  is related to  $G_1$  by a set of equations, [1]:

$$\Sigma(1, 2) = i \int G_1(1, 3) W(1^+, 4) \Gamma(3, 2; 4) d(3) d(4) \quad (3.4)$$

$$W(1, 2) = \int v(1, 3) \varepsilon^{-1}(3, 2) d(3) \quad (3.5)$$

$$\varepsilon(1, 2) = \delta(1, 2) - \int v(1, 3) P(3, 2) d(3) \quad (3.6)$$

$$P(1, 2) = -i \int G_1(2, 3) G_1(4, 2) \Gamma(3, 4; 1) d(3) d(4) \quad (3.7)$$

$$\Gamma(1, 2; 3) = \delta(1, 2) \delta(1, 3) + \int \frac{\delta \Sigma(1, 2)}{\delta G_1(4, 5)} G_1(4, 6) G_1(7, 5) \Gamma(6, 7; 3) d(4) d(5) d(6) d(7). \quad (3.8)$$

The short-hand notation  $1^+$  indicates that the time variable  $t_1$  is been augmented by a positive infinitesimal. It is important to use  $W(1^+, 4)$  in Equation (3.4) rather than  $W(1, 4)$  in order to correctly reproduce the four point operators in Equation (3.1), [1].  $W(1, 2)$  is the screened Coulomb interaction, which essentially gives the potential at point 1 due to the presence of a test charge at point 2, including the effect of the polarization of the electrons. It is appropriate to use the screened potential rather than the bare Coulomb potential, since particles in an interacting system respond to the total potential.  $P$  is the polarisability of the system,  $\varepsilon$  is the dielectric function which describes the dielectric screening, and  $\Gamma$  is a vertex function.

If  $G_0$  is the single-particle Green's function corresponding to the Hartree system, then the Green's function of an interacting system is calculated through Dyson's equation,

$$G_1(1, 2) = G_0(1, 2) + \int G_0(1, 3) \Sigma(3, 4) G_1(4, 2) d(3, 4) \quad (3.9)$$

The set of Equations (3.4-3.8) are called *Hedin's equations* and in principle, can be

solved self-consistently along with Equation (3.9). All many-particle effects i.e. correlation and exchange are included in the self-energy operator  $\Sigma$ .

Once  $G_1$  is known, it gives us not only information on single-particle excitation energies of the system, but also allows us to calculate the expectation value of any single-particle operator as well as the total energy operator [1]. However, in the present context we are only interested in the excitation spectra, and the other quantities will not be considered for the remainder of this work.

## 3.2 Quasiparticles

The complicated structure of the resulting space and time dependence of  $G_1$  makes a numerical treatment of Equation (3.9) very difficult. In the absence of a time-dependent external potential,  $G_1(1, 2)$  only depends on the time difference  $t_1 - t_2$  and can be mapped to frequency space through a Fourier transform. In that representation, one can focus on long-lived particle-like excitations of the system, electron or hole *quasiparticles*, that appear as well-defined sharp peaks in the spectrum of the frequency-dependent  $G_1(\omega)$ . Due to the non-Hermitian character of the self-energy operator, such quasiparticle states are characterised by a complex energy:  $\epsilon_m = E_m + i\gamma_m$ , where  $E_m$  is the energy position of the quasiparticle and  $\gamma_m$  is its inverse lifetime. Thus,  $G_1(\omega)$  will be dominated by a structure like

$$G_1(\omega) \sim \sum_m \frac{|m\rangle\langle m|}{\omega - \epsilon_m \pm i0^+}, \quad (3.10)$$

where  $0^+$  is a small positive constant which ensures that a function is analytic in the upper-half-plane. The spectral function or density of states  $A$  is given by a Lorentzian,

$$\begin{aligned} A(\omega) &= \frac{1}{\pi} \sum_m |\Im(G_{1m}(\omega))| \\ &= \frac{1}{\pi} \sum_m \frac{\gamma_m}{(\omega - E_m)^2 + \gamma_m^2} \end{aligned} \quad (3.11)$$

which is usually peaked at  $E_m$  with a spectral width of  $\gamma_m$ .  $G_{1m}(\omega)$  is the matrix element of  $G_1$  in an eigenstate  $\psi_m$  of the non-interacting system.  $A(\omega)$  could also show peaks or satellite structures at some other energies  $\omega_p$  which can be due to plasmon excitations



or other collective phenomena<sup>1</sup>. The residual structure  $|m\rangle\langle m|$  of the frequency poles can be understood as an amplitude (wave function) of the quasiparticle,  $\psi_m^{QP}(\mathbf{x})$ . The quasiparticle's inverse lifetime  $\gamma_m$  is given by the imaginary part of the self-energy  $\Sigma(\omega)$ . From Equations (3.3) and (3.10), an equation of motion of the quasiparticles can be derived:

$$H(\mathbf{r})\psi_m^{QP}(\mathbf{x}) + \int \Sigma(\mathbf{x}, \mathbf{x}', E)\psi_m^{QP}(\mathbf{x}')d\mathbf{x}' = \epsilon_m\psi_m^{QP}(\mathbf{x}) \quad (3.12)$$

### 3.3 The *GW* Approximation

The self-energy operator  $\Sigma$  and  $G_1$  can be computed from Equations (3.4 - 3.9) in a self-consistent procedure. However, in most calculations for real materials, that procedure is numerically difficult due to the high complexity of the problem. Particularly, the high dimensionality of the vertex function  $\Gamma(1, 2; 3)$ , the functional derivative,  $\delta\Sigma(1, 2)/\delta G_1(4, 5)$  and the sixteen-dimensional integration of Equation (3.8) are difficult. An approximation is required to simplify the procedure.

Firstly, the approach could be significantly simplified with a good choice of starting point for  $G_1$  which can be so close to the real  $G_1$  that a self-consistent treatment of the equations is not necessary. Secondly, a simplified expression for the vertex function  $\Gamma$  can be made. The most common and efficient approximation, introduced by Hedin [22] is the so-called *GW* approximation (GWA). This approximation neglects the second term in  $\Gamma$  i.e.  $\Gamma(1, 2; 3) \approx \delta(1, 2)\delta(1, 3)$  so that the polarisability can be schematically written as  $P(1, 2) = -iG_1(1, 2)G_1(2, 1)$ , and finally, the self-energy is given by

$$\Sigma(1, 2) = iG_1(1, 2)W(1^+, 2).$$

In the GWA, as a starting point,  $G_1$  and  $W$  are constructed from either the DFT or HFA eigenenergies and orbitals, which are commonly labeled as *SP* (for single particle) and

---

<sup>1</sup>If the interaction is switched on the peaks become broadened since the single-particle states can now decay to other excitations and lose some weight which might appear as collective excitations or satellite structures; it can be called the plasmon satellite due to the plasmon excitations.

$G_1$  is approximated by a non-interacting single-particle Green's function <sup>2</sup>

$$G_0(\mathbf{x}, \mathbf{x}', \omega) = \sum_n \frac{\psi_n^{SP}(\mathbf{x})\psi_n^{*SP}(\mathbf{x}')}{\omega - E_n^{SP} + i0 + \text{sign}(E_n^{SP} - E_F)}. \quad (3.13)$$

Then all of the quantities (3.5-3.7) are calculated only once and finally the  $G_0W_0$  self-energy,

$$\Sigma = iG_0W_0 \quad (3.14)$$

is used in Equation (3.9) to calculate  $G_1$  and its spectral function (3.11).

### 3.3.1 GW-DFT

In practical applications within the GWA, the non-interacting single-particle Green's function,  $G_0$  corresponds to a Hamiltonian which already contains some exchange or correlation effects. These have to be taken from  $\Sigma$ . The most common one is a DFT Hamiltonian, [see Equation (2.9)], which in addition to the Hartree term contains some local energy-independent exchange correlation potential,  $V_{xc}$ . Dyson's equation for  $G_1$  is then given by

$$G_1(1, 2) = G_0(1, 2) + \int G_0(1, 3)[\Sigma(3, 4) - V_{xc}(3)]G_1(4, 2)d(34). \quad (3.15)$$

Thus, the equation of motion for quasiparticles yields

$$H^{DFT}(\mathbf{r})\psi_m^{QP}(\mathbf{x}) + \int [\Sigma(\mathbf{x}, \mathbf{x}', E) - V_{xc}(\mathbf{x}')] \psi_m^{QP}(\mathbf{x}') d\mathbf{x}' = \epsilon_m \psi_m^{QP}(\mathbf{x}) \quad (3.16)$$

It is assumed that the quasiparticle amplitudes are well described by DFT wave functions, thus, quasiparticle energies are given by the simple equation

$$E_m^{QP} = E_m^{DFT} + \langle \psi_m^{DFT} | \Sigma(E_m^{QP}) - V_{xc} | \psi_m^{DFT} \rangle. \quad (3.17)$$

This implies that only diagonal elements of the operator  $\Sigma - V_{xc}$  have to be calculated. However in many materials DFT wave functions do not describe the true quasiparticle states well. In such cases quasiparticle wave functions can be expanded in a basis given by DFT wave functions,

$$|\psi_m^{QP}\rangle = \sum_n a_n^m |\psi_n^{DFT}\rangle$$

---

<sup>2</sup>In a crystal, the index  $n$  may be associated with the Bloch wave vector and band index.

In this basis the quasiparticle Hamiltonian operator corresponding to Equation (3.16) becomes

$$H_{nn'}^{QP} = E_n^{DFT} \delta_{nn'} + \langle \psi_n^{DFT} | \Sigma(E_m^{QP}) - V_{xc} | \psi_{n'}^{DFT} \rangle. \quad (3.18)$$

Now calculation of the full  $\Sigma - V_{xc}$  operator is required and the quasiparticle Hamiltonian (3.18) has to be diagonalised.

Equations (3.17) and (3.18) can be interpreted as a perturbative approach on top of the DFT calculation with a perturbation operator given by the difference between the GW self-energy (non-local exchange-correlation) operator and a local DFT exchange-correlation operator.

Although the difference operator  $\Sigma - V_{xc}$  is often called "the quasiparticle correction to the DFT band structure", there is no explicit expression for the difference to date. Instead, the matrix elements of both operators,  $\Sigma$  and  $V_{xc}$ , have to be calculated separately and then the difference is taken. It should be noted that both of them are quite large (-10 to -50 eV), and they cancel each other to a large degree, yielding final corrections of the order of a few tenths of an eV up to several eV. This poses the problem that both of them have to be calculated with a high accuracy to give a reliable value for the difference. Calculation of the self-energy operator  $\Sigma$  is described in the next section, while the  $V_{xc}$  is been extracted from CRYSTAL98 [23] within the DFT calculation.

### 3.3.2 GW-HFA

Alternatively, the non-interacting single particle Green's function,  $G_0$  can be obtained from the Hartree-Fock Hamiltonian, (2.6). The HFA takes the fermionic nature of the electrons into account which results in the exchange process. In that case the Hartree-Fock two-particle Green's function is given by

$$G_2^{HFA}(12, 1'2') = G_1(1, 2)G_1(1', 2') - G_1(1, 2')G_1(1', 2). \quad (3.19)$$

The first term corresponds to the non-interacting two-particle propagator while the second term corresponds to the quasi-particle added at point  $1'$  exchanging with the particle added at point  $2'$ , the minus sign results from the Fermi-statistics. This additional ex-

change term yields an equation of motion for  $G_1^{HFA}$  within the Hartree-Fock approximation. Thus in the HFA limit Equation (3.1) becomes

$$\left\{ i\hbar \frac{\partial}{\partial t} - H^{Hartree}(\mathbf{r}) \right\} G_1^{HFA}(1, 2) - \int G_1^{HFA}(1, 3) v(1, 3) G_1^{HFA}(3, 2) d(3) = \delta(1, 2). \quad (3.20)$$

The Hartree-Fock approximation includes the exchange self-energy correction

$$\Sigma_{ex}(\mathbf{x}, \mathbf{x}', E) = i G_1^{HFA}(\mathbf{x}, \mathbf{x}', E) v(\mathbf{r} - \mathbf{r}'), \quad (3.21)$$

which is understood as the lowest-order approximation for  $\Sigma$ .

Starting from the  $G_0 = G_1^{HFA}$  in the GWA, the exchange contribution accounted for in  $G_0$ , has to be taken out from the more general  $GW$  self-energy,  $\Sigma$ . Thus, the Dyson equation for  $G_1$  is given by

$$G_1(1, 2) = G_0(1, 2) + \int G_0(1, 3) \Delta\Sigma(3, 4) G_1(4, 2) d(3, 4). \quad (3.22)$$

with a self-energy given by

$$\Delta\Sigma(\mathbf{x}, \mathbf{x}', E) = \Sigma(\mathbf{x}, \mathbf{x}', E) - G_0(\mathbf{x}, \mathbf{x}', E) v(\mathbf{r}, \mathbf{r}'). \quad (3.23)$$

The quasiparticle equation thus obeys

$$H^{HFA}(\mathbf{r}) \psi_m^{QP}(\mathbf{x}) + \int \Delta\Sigma(\mathbf{x}, \mathbf{x}', E) \psi_m^{QP}(\mathbf{x}') d\mathbf{x}' = \epsilon_m \psi_m^{QP}(\mathbf{x}), \quad (3.24)$$

Again, we can assume that the quasiparticle amplitudes are well described by the single particle wave functions so the quasiparticle energies become

$$E_m^{QP} = E_m^{HFA} + \langle \psi_m^{HFA} | \Delta\Sigma(E_m^{QP}) | \psi_m^{HFA} \rangle. \quad (3.25)$$

### 3.4 Basis Sets

The numerical evaluation of the single-particle wave functions  $\psi_{n\mathbf{k}}(\mathbf{x})$  and of two-point functions  $\varepsilon(\mathbf{r}, \mathbf{r}')$ ,  $W(\mathbf{r}, \mathbf{r}')$ ,  $\Sigma(\mathbf{r}, \mathbf{r}')$ , etc. requires the expansion of all position dependent quantities in a suitable basis. The basis for the wave functions and for the two-point functions can be chosen independently. The most common representation is a plane-wave

(PW) representation of all functions [2, 11, 24]. Several different approaches have been proposed as well, such as a localised Gaussian orbital (GO) basis [7] for all functions, a combination of GO basis for the DFT and plane-wave representation for the GWA [6], a combination of linear-muffin-tin-orbitals (LMTO) basis for the DFT and product basis for the GWA [25], and real-space representation [5, 24].

In the present work we use combined GO-PW basis sets. The Linear Combination of Atomic Orbitals (LCAO) is used as a basis for single-particle wave functions. This approach is adopted in the CRYSTAL [23, 26] package, which is used to generate single-particle states. In this approach, the atomic orbitals are given as a linear combination of individually normalised, atom centred Gaussian type functions. More details about this type of basis are given in Appendix C.

Unlike, single-particle wave functions, all two-point functions are expanded in a plane-wave basis in this thesis. The choice of the plane-wave basis was motivated primarily by its simplicity. Other advantages are: (1) good control over convergence, and (2) the Coulomb interaction is diagonal with matrix elements given by  $\sim 4\pi/|\mathbf{q} + \mathbf{G}|^2$ . However, in this mixed-basis approach the efficacy of the matrix elements calculation has been lost from a programmer's point of view. Namely, the matrix elements can be calculated easily when the crystalline Bloch functions are also expanded in plane waves. There are also other disadvantages related to the plane-wave representation: (1) the convergence could be very slow for some systems, and large number of plane waves might be required, (2) there is no direct physical interpretation, (3) it cannot be easily used for atoms and molecules. Nevertheless, we adopt a plane waves approach as it is a good starting point in GWA and exciton effects code development and it is preferable to calculate certain elements of the GWA Gaussian orbital scheme in a plane-wave representation (e.g. the "head" and the "wings" of the dielectric matrix for case  $q \rightarrow 0$ , see Appendix B) and transform this into the Gaussian orbital basis in future work.

### 3.5 The Self-Energy Matrix Element

This section gives numerical details of the self-energy matrix calculation, and the final expression used in the thesis.

Within the GWA, the self-energy operator is given by a frequency convolution of the single-particle Green's function,  $G_1$  with the screened Coulomb interaction  $W$  (3.14). That can be written formally in a real-space and energy basis as

$$\Sigma(\mathbf{r}, \mathbf{r}', E) = \frac{i}{2\pi} \int e^{-i\omega 0^+} G_1(\mathbf{r}, \mathbf{r}', E - \omega) W(\mathbf{r}, \mathbf{r}', \omega) d\omega. \quad (3.26)$$

While  $G_1(\mathbf{r}, \mathbf{r}', E - \omega)$  is given by (3.13) within either the DFT or HFA framework,  $W$  involves a convolution of the inverted time-ordered dielectric function and the Coulomb potential,

$$W(\mathbf{r}, \mathbf{r}', \omega) = \int d\mathbf{r}'' \varepsilon^{-1}(\mathbf{r}, \mathbf{r}'', \omega) v(\mathbf{r}', \mathbf{r}''). \quad (3.27)$$

For the crystalline case it is appropriate at this point to exploit the lattice translation symmetry to transform this expression to a reciprocal-space basis. In the plane-wave basis this is done by the following decomposition:

$$W(\mathbf{r}, \mathbf{r}', \omega) = \sum_{\mathbf{q}, \mathbf{G}, \mathbf{G}'} e^{i(\mathbf{q} + \mathbf{G}) \cdot \mathbf{r}} W_{\mathbf{G}\mathbf{G}'}(\mathbf{q}, \omega) e^{-i(\mathbf{q} + \mathbf{G}') \cdot \mathbf{r}'} \quad (3.28)$$

where  $\mathbf{G}$  is a reciprocal lattice vector, and  $\mathbf{q}$  is a wavevector in the first Brillouin zone (1BZ). The Fourier coefficients in Equation (3.28) are given by

$$\begin{aligned} W_{\mathbf{G}\mathbf{G}'}(\mathbf{q}, \omega) &= \varepsilon_{\mathbf{G}\mathbf{G}'}^{-1}(\mathbf{q}, \omega) v_{\mathbf{G}\mathbf{G}'}(\mathbf{q}) \\ &= \frac{4\pi e^2}{\Omega} \frac{1}{|\mathbf{q} + \mathbf{G}| |\mathbf{q} + \mathbf{G}'|} \varepsilon_{\mathbf{G}\mathbf{G}'}^{-1}(\mathbf{q}, \omega), \end{aligned} \quad (3.29)$$

where  $\Omega$  denotes the crystal volume. The time-ordered symmetric dielectric matrix  $\varepsilon_{\mathbf{G}\mathbf{G}'}^{-1}(\mathbf{q}, \omega)$  is calculated using the random phase approximation (RPA) [27]:

$$\begin{aligned} \varepsilon_{\mathbf{G}\mathbf{G}'}(\mathbf{q}, \omega) &= \delta_{\mathbf{G}\mathbf{G}'} + 2 \frac{4\pi e^2}{\Omega} \frac{1}{|\mathbf{q} + \mathbf{G}| |\mathbf{q} + \mathbf{G}'|} \\ &\times \sum_{v,c} \sum_{\mathbf{k}} \langle c\mathbf{k} + \mathbf{q} | e^{i(\mathbf{q} + \mathbf{G}) \cdot \mathbf{r}} | v\mathbf{k} \rangle \langle v\mathbf{k} | e^{-i(\mathbf{q} + \mathbf{G}') \cdot \mathbf{r}'} | c\mathbf{k} + \mathbf{q} \rangle \\ &\times \left[ \frac{1}{E_{c, \mathbf{k} + \mathbf{q}} - E_{v, \mathbf{k}} - \omega + i0^+} + \frac{1}{E_{c, \mathbf{k} + \mathbf{q}} - E_{v, \mathbf{k}} + \omega + i0^+} \right] \end{aligned} \quad (3.30)$$

For detailed reading about the RPA dielectric matrix see Appendix B or [27, 28, 29, 30, 31, 32, 33, 34].

On combining the Fourier transformed expression for  $W$  with the non-interacting single-particle Green's function  $G_0$  (3.13), the diagonal matrix elements of the self-energy operator yield [35]:

$$\begin{aligned}
\langle m\mathbf{k} | \Sigma(E) | m\mathbf{k} \rangle &= \int \int d\mathbf{r} d\mathbf{r}' \psi_{m\mathbf{k}}^*(\mathbf{r}) \Sigma(\mathbf{r}, \mathbf{r}', E) \psi_{m\mathbf{k}}(\mathbf{r}') \\
&= \frac{4\pi e^2}{\Omega} \sum_{\mathbf{q}, \mathbf{G}, \mathbf{G}'} \sum_n \frac{\langle m\mathbf{k} | e^{-i(\mathbf{q}+\mathbf{G})\cdot\mathbf{r}} | n\mathbf{k} + \mathbf{q} \rangle \langle n\mathbf{k} + \mathbf{q} | e^{i(\mathbf{q}+\mathbf{G}')\cdot\mathbf{r}} | m\mathbf{k} \rangle}{|\mathbf{q} + \mathbf{G}| |\mathbf{q} + \mathbf{G}'|} \\
&\times \int_{\omega \in \mathbf{R}} d\omega e^{-i\omega 0^+} \frac{\varepsilon_{-\mathbf{G}, -\mathbf{G}'}^{-1}(-\mathbf{q}, \omega)}{E - \omega - E_{n, \mathbf{k}+\mathbf{q}} + i0^+ \text{sign}(E_{n, \mathbf{k}+\mathbf{q}} - E_F)} \quad (3.31)
\end{aligned}$$

The  $SP$  label has been left out from the eigenfunctions and eigenvalues for clarity throughout.

The time/frequency dependence can either be treated by grid representation [5, 24] or by a plasmon-pole approximation [2, 6]. In this work we adopt a plasmon-pole model which is presented in following section.

### 3.5.1 Plasmon-pole model

It is clear from a brief inspection of Equation (3.31) that a direct numerical evaluation involves the calculation of and inversion of the dielectric matrix,  $\varepsilon_{\mathbf{G}\mathbf{G}'}^{-1}(\mathbf{q}, \omega)$ , at many values of  $\omega$ . Although such schemes have been carried out by some authors [36], it is both time consuming and unnecessary in the present mixed GO+PW framework, (see Section 3.4). The physical features of  $W$  allow us to approximate the frequency dependence of the dielectric matrix and to solve the integral in (3.31) analytically. Namely, the imaginary part of  $W$  is characterised by a strong peak corresponding to a plasmon excitation at the plasmon frequency. This is particularly evident for the electron gas and for simple systems with only  $s$ - and  $p$ -type orbitals occupied. Based on these facts a so-called plasmon-pole model has been introduced. The plasmon-pole model assumes that all the weight in  $\Im(W)$  resides in the plasmon excitation [3, 37]. This is strictly true for the electron gas case in the long wavelength limit  $\mathbf{q} \rightarrow 0$  [3, 37]. For finite  $\mathbf{q}$ , however,

the spectrum contains also electron-hole excitations at lower energy. The electron-hole spectrum eventually merges with the plasmon excitations as  $\mathbf{q}$  gets larger.

Several different plasmon-pole models have been proposed in the literature [3, 22, 37, 38, 39], and all of these models use the static dielectric matrix to fit the dynamic  $\varepsilon(\omega)$ . The model adopted in this thesis is one based on the model of von der Linden and Horsch [38], which uses the concept of dielectric band structure (DBS) [40]. The inverse of the symmetric dielectric matrix can be generated from its eigenvalues,  $\varepsilon_{\mathbf{q}l}^{-1}(\omega)$  and orthonormal eigenvectors,  $V_{l\mathbf{G}}(\mathbf{q})$ . The model assumes that all frequency dependence is projected onto eigenvalues, so the inverse of the dielectric matrix can be approximated by

$$\varepsilon_{\mathbf{G}\mathbf{G}'}^{-1}(\mathbf{q}, \omega) = \sum_l V_{l\mathbf{G}}(\mathbf{q}) \varepsilon_{\mathbf{q}l}^{-1}(\omega) V_{l\mathbf{G}'}^*(\mathbf{q}). \quad (3.32)$$

The sum over  $l$  runs over all of the eigenvalues and corresponding eigenvectors. The model form of the eigenvalues,  $\varepsilon_{\mathbf{q}l}^{-1}(\omega)$ , is given by

$$\varepsilon_{\mathbf{q}l}^{-1}(\omega) = 1 + \frac{z_{\mathbf{q}l}\omega_{\mathbf{q}l}}{2} \left( \frac{1}{\omega - \omega_{\mathbf{q}l} + i0^+} - \frac{1}{\omega + \omega_{\mathbf{q}l} - i0^+} \right) \quad (3.33)$$

where  $z_{\mathbf{q}l}$  are weighting parameters, and  $\omega_{\mathbf{q}l}$  are the plasmon frequencies. Originally [38],  $z_{\mathbf{q}l}$  and  $\omega_{\mathbf{q}l}$  are generated by adjusting (3.32) and (3.33) to the static dielectric matrix and taking Johnson's  $f$ -sum rule [41],

$$\int_0^\infty d\omega \omega \Im(\varepsilon_{\mathbf{G}\mathbf{G}'}^{-1}(\mathbf{q}, \omega)) = -\frac{\pi}{2} \omega_{\mathbf{q}l}^2 \frac{\rho(\mathbf{G} - \mathbf{G}')}{\rho(0)} \frac{(\mathbf{q} + \mathbf{G}) \cdot (\mathbf{q} + \mathbf{G}')}{|\mathbf{q} + \mathbf{G}'|^2},$$

into account.  $\rho(\mathbf{G})$  is the Fourier components of the crystalline charge density. The same approach could be applied to the DFT based calculations in this thesis. However, the idea was to make the model work not only for the calculations within a DFT framework, but also for the Hartree-Fock RPA dielectric function. It has been shown [42] that the dielectric function obtained from a Hartree-Fock band structure violates the sum rule. This was expected in the presence of a non-local potential in the single-particle Hamiltonian, which is the case in the Hartree-Fock Hamiltonian. Motivated by this fact, a simple fitting procedure has been adapted in [42] to determine the weights  $z_{\mathbf{q}l}$  and the plasmon frequencies  $\omega_{\mathbf{q}l}$ . The dielectric matrix is calculated at two frequencies: at zero frequency



and at some finite imaginary frequency  $i\omega_f$ . It can be shown easily that

$$\omega_{\mathbf{ql}}^2 = \frac{-\omega_f^2[1 - \varepsilon_{\mathbf{ql}}^{-1}(i\omega_f)]}{\varepsilon_{\mathbf{ql}}^{-1}(i0) - \varepsilon_{\mathbf{ql}}^{-1}(i\omega_f)} \quad (3.34)$$

$$z_{\mathbf{ql}} = 1 - \varepsilon_{\mathbf{ql}}^{-1}(i0) \quad (3.35)$$

The imaginary axis was chosen because the dielectric matrix obeys a Lorentzian frequency behaviour on the imaginary axis, while it is very sensitive to the choice of  $\omega_f$  on the real axis as rapid fluctuations occur in  $\varepsilon_{\mathbf{ql}}$  for energies around and above the gap.

Figures (3.1 - 3.4) demonstrate how eigenvalues of the dielectric matrix for bulk Silicon and solid Argon compare with the eigenvalues generated by the plasmon-pole model. The agreement is quite good over the full frequency range along the imaginary frequency axis ( $i\omega$ ), at both finite  $\mathbf{q}$  and in the  $\mathbf{q} \rightarrow 0$  limit, so the choice of fitting frequency,  $i\omega_f$  is not vital, any value chosen around the fundamental gap will give satisfactory results. However, when fitted values are projected onto the real frequency axis the agreement is good only at low  $\omega$  values. Similar results were obtained for Silicon by Hybertsen and Louie [43]. It is important to mention that the frequency integration in Equation (3.31) is still performed along the real  $\omega$  axis. This means that the plasmon-pole model is not suitable for determining self-energy matrix elements accurately for the higher energy bands. However, this will not be a major concern; since we are interested only in optical properties, it is important to accurately determine states at the top of the valence band and the bottom of the conduction band usually. A few more conduction bands could be required for optical properties of some materials.

Finally, the plasmon-pole form of the inverted dielectric matrix allows us to perform the analytical integration over frequency in (3.31). This yields the following expression for the expectation value of  $\Sigma$ :

$$\begin{aligned} \langle m\mathbf{k}|\Sigma(E)|m\mathbf{k}\rangle &= \frac{4\pi^2 e^2}{\Omega} \sum_{\mathbf{q}, \mathbf{G}, \mathbf{G}'} \sum_n \frac{\langle m\mathbf{k}|e^{-i(\mathbf{q}+\mathbf{G})\cdot\mathbf{r}}|n\mathbf{k}+\mathbf{q}\rangle \langle n\mathbf{k}+\mathbf{q}|e^{i(\mathbf{q}+\mathbf{G}')\cdot\mathbf{r}'}|m\mathbf{k}\rangle}{|\mathbf{q}+\mathbf{G}||\mathbf{q}+\mathbf{G}'|} \\ &\times \begin{cases} \sum_l V_{l,-\mathbf{G}}(-\mathbf{q})V_{l,-\mathbf{G}'}^*(-\mathbf{q}) \left[ -1 + \frac{z_{-\mathbf{ql}}\omega_{-\mathbf{ql}}}{2} \frac{1}{E-E_{n\mathbf{k}+\mathbf{q}+\omega_{-\mathbf{ql}}}} \right] & \text{for } n \in \text{occupied} \\ \sum_l V_{l,-\mathbf{G}}(-\mathbf{q})V_{l,-\mathbf{G}'}^*(-\mathbf{q}) \left[ \frac{z_{-\mathbf{ql}}\omega_{-\mathbf{ql}}}{2} \frac{1}{E-E_{n\mathbf{k}+\mathbf{q}-\omega_{-\mathbf{ql}}}} \right] & \text{for } n \in \text{empty} \end{cases} \end{aligned} \quad (3.36)$$

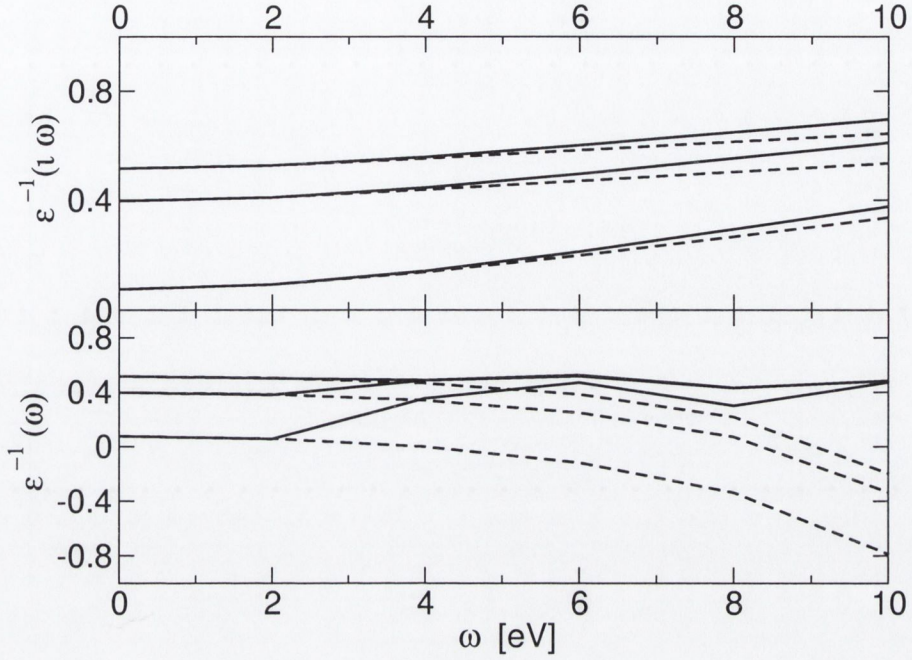


**Figure 3.1:** Comparison between plasmon-pole model (dashed lines) and fully calculated eigenvalues of the inverted dielectric matrix (solid lines) for bulk Si, for the smallest eigenvalues in the  $\mathbf{q} \rightarrow 0$  limit, plotted along the real frequency,  $\omega$ , axis (bottom panel) and imaginary,  $\omega$ , (top panel)

From a brief inspection of this equation we can see that self-energy splits into a bare exchange part (from the “ $-1$  for  $n$  occupied”) which arises from the Hartree-Fock exchange potential and a part containing the contributions from correlation:

$$\langle m\mathbf{k} | \Sigma(E) | m\mathbf{k} \rangle = \langle m\mathbf{k} | \Sigma_{ex} | m\mathbf{k} \rangle + \langle m\mathbf{k} | \Sigma_c(E) | m\mathbf{k} \rangle. \quad (3.37)$$

All energy dependence of the self-energy is contained in the correlation part (dynamic part),  $\langle m\mathbf{k} | \Sigma_c(E) | m\mathbf{k} \rangle$ . If the *GW*-HFA is used the exchange  $\langle m\mathbf{k} | \Sigma_{ex} | m\mathbf{k} \rangle$  term is explicitly contained in the initial self-consistent Hartree-Fock calculation.

It is clear from Equation (3.36) how computationally intensive the calculation of the self-energy matrix elements is, even with a plasmon-pole model. Some illustrative examples as well as numerical details of the calculations are discussed in Chapter 4.

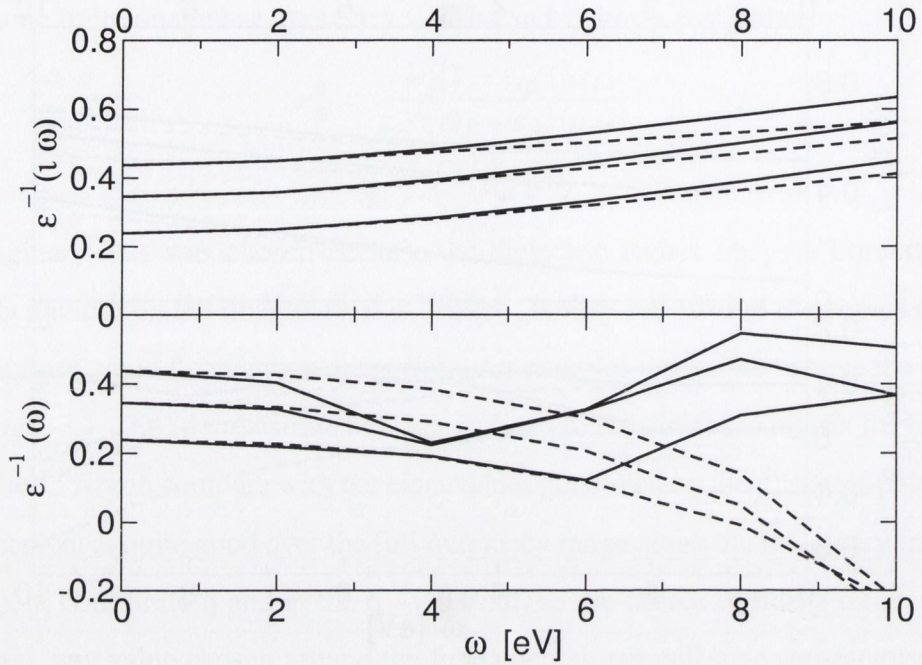


**Figure 3.2:** Same as Figure 3.1, in the  $\mathbf{q} = [1, 1, 0] 2\pi/a$

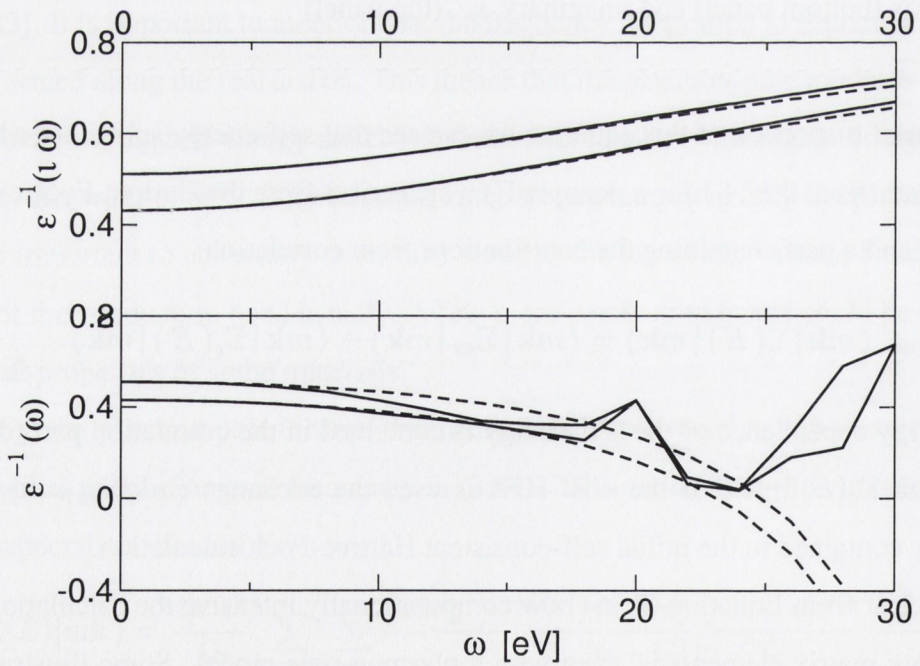


**Figure 3.3:** Comparison between plasmon-pole model (dashed lines) and fully calculated eigenvalues of the inverted dielectric matrix (solid lines) for solid Ar, for the smallest eigenvalues in the  $\mathbf{q} \rightarrow 0$  limit, plotted along the real,  $\omega$ , axis (bottom panel) and imaginary,  $\omega$ , (top panel)

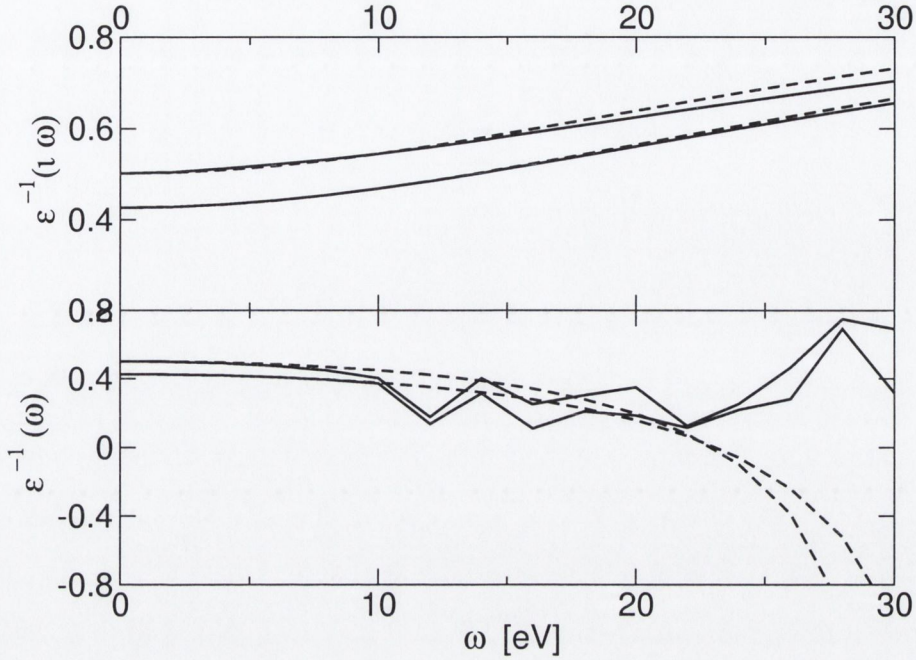


**Figure 3.4:** Same as Figure 3.3, in the  $\mathbf{q} = [1, 1, 0] 2\pi/a$

### 3.6 Determination of Quasiparticle Energies

Once the self-energy matrix elements  $\langle m\mathbf{k} | \Sigma(E) | m\mathbf{k} \rangle$  are evaluated, the quasiparticle Equation (3.17) or (3.25) must be solved. This involves calculation of the self-energy matrix element at the actual quasiparticle energy,  $E_{m\mathbf{k}}^{QP}$ . Sometimes, just inserting the single particle energy value  $E_{m\mathbf{k}}^{SP}$  into the self-energy operator on the right-hand side of Equation (3.17) gives reliable quasiparticle energies. This approach avoids further iterations of (3.17) with respect to the quasiparticle energy. However, it neglects the possibility that the self-energy operator may depend on energy  $E$ .

A somewhat better scheme is given by Hybertsen and Louie in [3] by the equation

$$E_{m\mathbf{k}}^{QP} \approx E_{m\mathbf{k}}^{SP} + Z_{m\mathbf{k}} \Re(\langle m\mathbf{k} | \Delta\Sigma(E_{m\mathbf{k}}^{SP}) | m\mathbf{k} \rangle) \quad (3.38)$$

where  $Z_{m\mathbf{k}}$  are renormalisation factors. They are defined by

$$Z_{m\mathbf{k}} = \left( 1 - \frac{\partial \Re(\langle m\mathbf{k} | \Sigma_c(E) | m\mathbf{k} \rangle)}{\partial E} \Big|_{E=E_{m\mathbf{k}}^{SP}} \right)^{-1} \quad (3.39)$$

The operator  $\Delta\Sigma$  is either given by

$$\Delta\Sigma(\mathbf{x}, \mathbf{x}', E) = \Sigma(\mathbf{x}, \mathbf{x}', E) - V_{xc}(\mathbf{x}) \quad (3.40)$$

for the case of DFT initial calculation or by

$$\Delta\Sigma(\mathbf{x}, \mathbf{x}', E) = \Sigma(\mathbf{x}, \mathbf{x}', E) - G_1(\mathbf{x}, \mathbf{x}', E)v(\mathbf{r} - \mathbf{r}') \quad (3.41)$$

for the HFA. The derivative  $\partial\langle m\mathbf{k} | \Sigma_c(E_{m\mathbf{k}}^{SP}) | m\mathbf{k} \rangle / \partial E$  is evaluated as a difference quotient, calculating the correlation part of self-energy matrix element at two energy points around the  $E^{SP}$  energy value,  $E^{SP} - \Delta$  and  $E^{SP} + \Delta$ . The size of  $\Delta$  was varied to check its effect on quasiparticle energies. It was observed that there are no changes in the energies at the  $\Gamma$  point if  $\Delta$  was varied from 0.2 eV to 1 eV for all materials studied in this work. This scheme is used throughout this work.

### 3.7 Beyond $G_0W_0$

For many materials  $G_0W_0$  already gives highly reliable single-particle spectra, so a self-consistent procedure defined by Equations (3.4-3.8) is not necessary. However, the interacting single-particle Green's function  $G_1$  obtained from the Dyson Equation (3.9) is not necessarily the same as  $G_0$ . Self-consistency is evidently an important issue. Firstly, it guarantees that the final results are independent of the starting Green's function. Secondly, without self-consistency the GWA fails to conserve the particle number, energy and momentum under a time-dependent external perturbation according to the Baym-Kadanoff theory [44].

A number of authors have gone beyond the simple  $G_0W_0$  expression and extended the approach towards self-consistency [45, 46]. It turns out that self-consistency within GWA has a disadvantageous effect on the accuracy of calculated spectral properties. The results of these studies are: (1) the band gap is increased from its non-self-consistent value, worsening the agreement with experimental value; (2) the plasmon satellite is broadened and shifted towards the Fermi energy; and (3) the quasiparticles are narrowed, increasing their lifetime. This can be explained as follows. Unlike  $G_0$ , which refers to

**Figure 3.5:** Diagrammatic expansion for the self-energy operator. The arrows represent the non-interacting Green's function, the wiggly line is a screened interaction. The first diagram is a first-order diagram and corresponds to the GWA, the latter two are self-consistency term and the vertex correction, respectively.

a non-interacting system with single-particle excitations only, some spectral weight in the interacting Green's function  $G_1$  is transferred to a plasmon satellite, which describes collective excitations. The quasiparticle peaks are reduced accordingly. This implies a significant reduction in the dynamic self-energy part that describes correlation,  $\Sigma_c$ . The correlation part of the self-energy is positive, and tends to reduce the band gap, while the exchange part is always negative and increases the gap [4]. In the self-consistent calculation, the exchange part is only marginally reduced, so it dominates over the correlation and tends to increase the band gap. As a result, the gap usually becomes overestimated. Reduction of the correlation part of the self-energy also explains the increase in the quasiparticle lifetime, which is inversely proportional to the  $\Im(\Sigma_c)$ .

In conclusion, a self-consistent GWA approach does not give reliable quasiparticle energies. One way of solving Equations (3.4-3.8) self-consistently is by the simultaneous introduction of the vertex function, which has been approximated by the delta function in the GWA. The self-energy can be expressed in terms of Feynman diagrams, some of which are shown on Figure 3.5. Arrows represent noninteracting Green's functions and the screened interaction is indicated by a wiggly line. The first diagram is the GWA. The second is a self-consistency term, and the third represents vertex corrections. Vertex corrections introduce additional interaction channels not accounted for in the GWA self-energy and RPA polarisability. Vertex corrections in the polarisability, in general, reduce the screening and strengthen the interaction. In the self-energy, vertex corrections describe exchange and correlation effects between the central photoemission hole and the surrounding particles, thereby reducing the probability of finding other holes near

the central photoemission hole. These two effects compete and cancel partially. Indeed, many authors have reported cancellation between vertex and self-consistency diagrams [47, 48]. Schindlmayr and Godby [49] proposed a systematic approach based on a continued iterative solution of Hedin's equations. Numerical results for a finite Hubbard cluster [49] were promising and suggest that an iterative solution of Hedin's equations can improve the spectrum. Generally, a systematic way of improving quasiparticle energies is still outstanding.

## Chapter 4

# Quasiparticle Band Structure of Bulk Materials

The  $GW$  method has turned out to be a highly successful approach for calculation of single-particle excitations for wide range of materials. The main focus of this chapter is to discuss the approach and illustrate the self-energy calculation for various of materials. Quasiparticle energies are the basis for further investigation of the optical properties and coupled electron-hole excitations. The aim of this chapter is to show the reliability and accuracy of the  $GW$  approach. Quasiparticle band structures are presented along symmetry lines and discussed. Energy dependent self-energy matrix elements for selected bands and materials have been discussed as well.

The chapter has been divided into two main sections. The first section gives  $GW$  calculations based on DFT-LDA eigenstates while the second section presents results for  $GW$ -HFA band structure. Numerical details involved in the different steps in the calculations are given within the sections.

### 4.1 $GW$ -DFT Calculations

We calculate the quasiparticle band structure for silicon and compare it with published data in order to investigate its accuracy. Then, we apply the approach to the condensed rare gas solids (RGS): Ne, Ar, Kr and Xe in the FCC structure. Numerical details involved in LDA and  $GW$  calculations and convergence criteria are presented in Section 4.1.1 and 4.1.2, respectively for all materials. Then the results for self-energy and



quasiparticle band structures are presented in Section 4.1.3 for Si and 4.1.4 for the rare gases.

All energy values presented further, refer to the valence-band maximum, that is set to 0 eV in each case.

#### 4.1.1 Details of the DFT-LDA calculation

The results of the LDA calculation enter into the  $GW$  scheme at several points. Firstly, they enter into single particle Green's functions and the RPA dielectric matrix to generate the self-energy operator, see Equations (3.26-3.29). Secondly, the LDA states are used as a basis for the calculation of the self-energy matrix element, Equations (3.31, 3.36) and finally, LDA eigenenergies are used to obtain the quasiparticle energies (3.17). Therefore, the LDA calculation must be carried out very carefully. We use the *ab initio* package CRYSTALxx<sup>1</sup> [23, 26] to generate DFT-LDA eigenvectors, eigenvalues and exchange correlation potential.

Unlike many other calculations, the CRYSTAL package uses the Linear Combination of Atomic Orbitals (LCAO) approach in which the Bloch functions,  $\phi_\mu(\mathbf{r}, \mathbf{k})$  are expanded over the crystal lattice vectors  $\mathbf{R}$  in terms of atomic orbitals,  $\varphi_\mu$ :

$$\phi_\mu(\mathbf{r}, \mathbf{k}) = \sum_{\mathbf{R}} \varphi_\mu(\mathbf{r} - \mathbf{A}_\mu - \mathbf{R}) e^{i\mathbf{k}\cdot\mathbf{R}}. \quad (4.1)$$

Single exponent Gaussian type functions can be used for each  $\varphi_\mu$ , but it is more efficient to use linear combinations of individually normalised Gaussian type functions,  $G[a_j; \mathbf{r}]$  which are called contractions:

$$\varphi_\mu(\mathbf{r} - \mathbf{A}_\mu - \mathbf{R}) = \sum_j^{n_G} d_j G[a_j; \mathbf{r} - \mathbf{A}_\mu - \mathbf{R}] \quad (4.2)$$

The contractions are grouped into 'shells' of the same type, i.e.  $s$ ,  $p$  and  $d$  to improve the computational efficiency. This leads to shorter computational times than the traditional plane wave basis approach, however it involves additional difficulties regarding the construction of the complete and appropriate basis set. A large number of unoccupied states

---

<sup>1</sup>Currently code SMEXCITON runs in conjunction with CRYSTAL95 and CRYSTAL98, (see Appendix A).

**Table 4.1:** Experimental lattice constants in Å.

	$a_0$
Si	5.429 <sup>a</sup>
Ne	4.429 <sup>b</sup>
Ar	5.256 <sup>b</sup>
Kr	5.706 <sup>c</sup>
Xe	6.2023 <sup>d</sup>

<sup>a</sup>Reference [56].    <sup>c</sup>Reference [57].  
<sup>b</sup>Reference [58].    <sup>d</sup>Reference [59].

is needed to achieve well converged results, for the self-energy matrix element (3.36) and dielectric matrix (3.30). Thus, special care has to be taken while constructing the Gaussian orbital basis set. The criteria used in construction of the Gaussian orbital basis sets, as well as some illustrative applications and convergence tests and tables of the sets used in this work are given in Appendix C. Several basis sets are presented in Appendix C for Si from which the two largest are chosen in further calculations: pseudopotential valence basis set labeled 'PP 64 AO' and all-electron basis set labeled '88 AO'. For each of the RGS a single basis set is presented in Appendix C.

We use LDA exchange [50] and a Perdew and Zunger [51] correlation potential for silicon. LDA exchange and Perdew-Wang correlation [52] are used for RGS: Ar, Kr and Xe. For Ne, only the LDA exchange potential is used. The potential was changed for RGS, because the latter gave more accurate results for the band structure, total energy etc. The Perdew-Wang correlation functional was also presented as a more accurate potential by the authors in [52]. For pseudopotential basis sets, the Hay and Wadt Large Core [53, 54] parametrisation is used for silicon and the Durand and Barthelat Large Core [55] is used for neon. Experimental values have been used for the lattice constant,  $a_0$  and are listed in Table 4.1.

## 4.1.2 Details of the $GW$ calculation

The calculation of the  $GW$  self-energy matrix element involves summation over both occupied and virtual states,  $n$ , a double sum over reciprocal lattice vectors,  $G$  and  $G'$  and a sum over  $\mathbf{q}$ -vectors from the first Brillouin zone. All these sums require careful examination for convergence.

The calculation is more efficient if we separate the static bare exchange part of the self-energy from the energy-dependent (dynamic) part which arises from correlation [see Equations (3.36) and (3.37)]. The static part is equivalent to the Hartree-Fock exchange energy:

$$\langle m\mathbf{k} | \Sigma_{ex} | m\mathbf{k} \rangle = -\frac{4\pi^2 e^2}{\Omega} \sum_{\mathbf{q}, \mathbf{G}} \sum_n^{occ} \frac{|\langle m\mathbf{k} | e^{-i(\mathbf{q}+\mathbf{G})\cdot\mathbf{r}} | n\mathbf{k} + \mathbf{q} \rangle|^2}{|\mathbf{q} + \mathbf{G}|^2} \quad (4.3)$$

In this relation, a sum over bands,  $n$  runs only over occupied states and it is important to include all core states in an all-electron basis set approach, e.g. inclusion of the core states increased the direct gap by 0.3 eV for Si. The effect was similar in the rare gases. The static term is diagonal with respect to the reciprocal lattice vectors  $\mathbf{G}$  due to the orthogonality of the dielectric matrix eigenvectors  $\sum_l V_{l,-\mathbf{G}}(-\mathbf{q}) V_{l,-\mathbf{G}'}^*(-\mathbf{q}) = \delta_{\mathbf{G}\mathbf{G}'}$ . However a large number of  $\mathbf{G}$  vectors is required to achieve well converged results. Generally, up to 400  $\mathbf{G}$  vectors were used for rare gases and 283  $\mathbf{G}$  vectors were used for the all-electron approach calculations for silicon. An increase in the number to the next shell, 375  $\mathbf{G}$  vectors changed the gap by 0.02 eV for Si. When the pseudopotential valence electron basis set was used, only 70  $\mathbf{G}$  vectors gave sufficient convergence for Si and 200  $\mathbf{G}$  vectors for Ne.

When the correlation part of the self-energy was calculated, inclusion of the core states induced changes in the quasiparticle energy states by less than 0.01 eV, for Si and the RGS, which is less than the general accuracy obtained with GWA. This is not surprising, due to the large binding energies of these states, the interaction between them and valence electrons is small. So they are neglected in the calculation of the dynamic part of the self-energy. The total number of conduction bands included in the summation in (3.36) was limited by the size of the basis set. The summation was truncated at the upper free-electron limit as described in Appendix C. In the summation over  $\mathbf{G}$  and  $\mathbf{G}'$ ,

59 vectors gave well converged results for all materials considered. This convergence is directly determined by the size and convergence of the dielectric matrix eigenvalues and eigenvectors. Details of the dielectric matrix calculation, as well as some illustrative examples are given in Appendix B.

The sum over  $\mathbf{q}$  from the first Brillouin zone for self-energy matrix elements in (3.36) is performed using Monkhorst-Pack special points [60]. Two special points in the IBZ and their stars give sufficient accuracy. The use of ten special points results in quasiparticle energy differences less than 0.07 eV for Si. The differences were even smaller for the rare gases.

One important difficulty remains related to the summation over  $\mathbf{q}$  points. Namely, if  $\mathbf{G} = \mathbf{G}' = 0$  and  $m = n$ , the terms to be summed up in (3.36) diverge for small  $\mathbf{q}$  as  $f(\mathbf{q}) = A/q^2$ . The special-point theorem is invalid in the presence of singularities. As noted by several authors [6, 61, 62], this summation has to be treated with care. The auxiliary function technique of Gygi *et al.* [61] has been adopted in this work. To perform the sum by special points, an auxiliary function  $g(\mathbf{q})$  that shows the same behavior for  $\mathbf{q} \rightarrow 0$  as  $f(\mathbf{q})$  has to be introduced as follows:

$$\sum_{\mathbf{q}} f(\mathbf{q}) \equiv \sum_{\mathbf{q}} [f(\mathbf{q}) - Ag(\mathbf{q})] + A \sum_{\mathbf{q}} g(\mathbf{q}), \quad (4.4)$$

with

$$A = \lim_{\mathbf{q} \rightarrow 0} [q^2 f(\mathbf{q})].$$

The term  $f(\mathbf{q}) - Ag(\mathbf{q})$  in (4.4) does not contain any divergence and special points can be used to evaluate the sum over  $\mathbf{q}$  in the (3.36). If the auxiliary function,  $g(\mathbf{q})$  is chosen carefully, then the second term in (4.4) or the corresponding integral over the first Brillouin zone can be done analytically [61]. The auxiliary functions used in this work, as well as the corresponding integrals are presented in Table 4.2. If only one vector ( $\mathbf{G}$  or  $\mathbf{G}'$ ) is zero and  $m = n$  the terms to be summed up in (3.36) diverge for small  $\mathbf{q}$  like  $f(\mathbf{q}) = B/q$ . Since these divergences are less problematic than  $1/q^2$ , they are not considered in this work. Alternatively, the same technique can be applied to this case.

As can be seen from (3.36), calculation of the self-energy matrix elements requires the calculation of the dielectric matrix at each special point  $\mathbf{q}$  and at  $\mathbf{q} \rightarrow 0$ . The latter

**Table 4.2:** Auxiliary functions,  $g(\mathbf{q})$  and their integrals over the Brillouin zone [61] for the simple cubic, face-centred cubic and body-centred cubic lattices.  $a$  is the lattice constant.

---



---

Simple cubic (SC):

$$g(\mathbf{q}) = \frac{a^2/2}{3 - \cos(aq_x) - \cos(aq_y) - \cos(aq_z)}$$

$$\sum_{\mathbf{q}} g(\mathbf{q}) = \left(\frac{a^2}{2\pi^3}\right) 15.67249523473854$$


---

Face-centred cubic (FCC):

$$g(\mathbf{q}) = \frac{(a/2)^2}{3 - \cos(\frac{aq_x}{2})\cos(\frac{aq_y}{2}) - \cos(\frac{aq_y}{2})\cos(\frac{aq_z}{2}) - \cos(\frac{aq_x}{2})\cos(\frac{aq_z}{2})}$$

$$\sum_{\mathbf{q}} g(\mathbf{q}) = \left(\frac{a^2}{4\pi^3}\right) 13.89764556215925$$


---

Body-centred cubic (BCC):

$$g(\mathbf{q}) = \frac{(a/2)^2}{1 - \cos(\frac{aq_x}{2})\cos(\frac{aq_y}{2})\cos(\frac{aq_z}{2})}$$

$$\sum_{\mathbf{q}} g(\mathbf{q}) = \left(\frac{a^2}{4\pi^3}\right) 43.19806651591508$$


---



---

is used to determine the quantity  $A$  in (4.4). The full RPA dielectric matrix (3.30) is computed at each point. Again to perform the sum over  $\mathbf{k}$  points in (3.30) we use special points. The dielectric constant was calculated using 10 and 27 special points in the IBZ. The results differ by less than 6%. So, ten special points and their stars are considered as sufficient to give well converged results.

The central problem with the realisation of the GWA is the calculation of the spatial integrals  $\langle m\mathbf{k}|e^{-i\mathbf{Q}\cdot\mathbf{r}}|n\mathbf{k} + \mathbf{q}\rangle$  (where  $\mathbf{Q} = \mathbf{q} + \mathbf{G}$ ) that appear in (3.30) and (3.31). We

write the crystalline orbitals as a linear combination of Bloch functions (4.1),

$$\psi_{m\mathbf{k}}(\mathbf{r}) = \sum_{\mu} a_{\mu m}(\mathbf{k}) \sum_{\mathbf{R}} \varphi_{\mu\mathbf{k}}(\mathbf{r} - \mathbf{A}_{\mu} - \mathbf{R}) \cdot e^{i\mathbf{k}\cdot\mathbf{R}} \quad (4.5)$$

where  $\varphi_{\mu\mathbf{k}}$  is, a localised atomic orbital (4.2) centred at  $\mathbf{A}_{\mu}$ , the sum over  $\mathbf{R}$  spans all lattice vectors and  $a_{\mu m}(\mathbf{k})$  are LDA eigenvector coefficients. Thus, the integral over the crystalline orbitals reduces to a sum over integrals over the Gaussian type functions:

$$\langle m\mathbf{k} | e^{-i\mathbf{Q}\cdot\mathbf{r}} | n\mathbf{k} + \mathbf{q} \rangle = \sum_{\mu\mu'} a_{\mu m}^* a_{\mu' n} \sum_{\mathbf{R}} e^{i\mathbf{k}\cdot\mathbf{R}} \int d\mathbf{r} \varphi_{\mu\mathbf{k}}^*(\mathbf{r} - \mathbf{A}_{\mu}) e^{i\mathbf{Q}\cdot\mathbf{r}} \varphi_{\mu'\mathbf{k}+\mathbf{q}}(\mathbf{r} - [\mathbf{A}_{\mu'} + \mathbf{R}]). \quad (4.6)$$

These are analytically evaluated and more detailed reading can be found in [63] and [42].

### 4.1.3 Results for Si

First of all, we applied our approach to Si in order to investigate its accuracy. We have used the pseudopotential ‘PP 64 AO’ and all electron ‘88 AO’ basis sets (see Appendix C) and our results are compared to highly converged plane-wave calculations. The reason for this was to investigate convergence criteria and the effect of core electrons on the GWA calculations within a localised Gaussian orbital all-electron framework.

The *GW* and LDA band-structures calculated along high-symmetry lines are shown in Figure 4.1. The left and right panels present the pseudopotential and all-electron calculations respectively. On first inspection, it can be noticed that *GW* quasiparticle corrections shift all conduction bands uniformly up when using the pseudopotential approach. While this effect was reported by the earlier pseudopotential valence electron basis set calculations [3, 6], it is not present in our all-electron Gaussian orbital framework. There is a strong dependence between quasiparticle corrections and the wave-vector  $\mathbf{q}$  on the right panel of Figure 4.1.

To investigate this further, first, we compare our LDA results to the plane wave calculations in [5]. The results are given in the first and second columns in Table 4.3, for pseudopotential and all-electron respectively, while the plane wave data, taken from [5] are presented in the third column. Both, our PP 64 AO and 88 AO LDA calculations yield similar results to the plane wave LDA calculation. Also the all-electron basis set

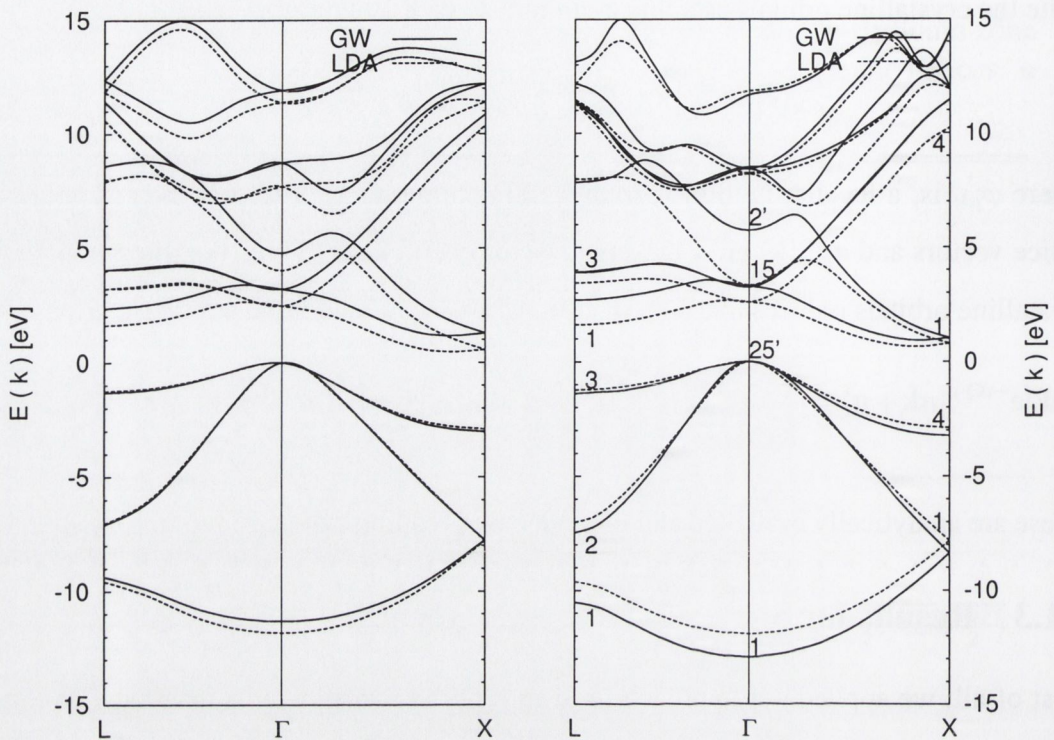


**Figure 4.1:** Band structure for Silicon, *GW* (solid line) and *LDA* (dashed line). Left panel is a pseudopotential valence electron based calculation and the right panel presents all-electron basis set calculation.

calculation data agrees slightly better with the published data [5] than the pseudopotential calculation. Thus, both our basis sets, all-electron and pseudopotential valence electron are suitable to obtain reliable results for *LDA* band structure. Furthermore, they should provide a good basis for *GW* calculations.

Secondly, we compare our *GW* band structure to the plane wave non-self-consistent calculation of Rieger *et al.* [5]. The results are given in Table 4.4. The first and second columns give our pseudopotential and all-electron calculations respectively, the third column shows results taken from [5] and the last column shows experimental data.

The valence band width, 12.92 eV obtained by using the all-electron basis set is in excellent agreement with the experimental value of  $12.5 \pm 0.6$  eV, while our pseudopotential calculation as well as plane-wave data from [5] underestimates the experimental value. The lowest conduction band,  $\Gamma_{15c} = 3.33$  eV is again close to the experimental

**Table 4.3:** Calculated LDA eigenenergies at points of high symmetry for Si (in eV) using the pseudopotential valence electron basis (PP 64 AO) and all-electron basis set (88 AO) in a comparison with plane waves LDA calculation.

Band	PP 64 AO	88 AO	PW <sup>a</sup>
$\Gamma_{1v}$	-11.7	-11.90	-11.99
$\Gamma'_{25v}$	0.0	0.0	0.0
$\Gamma_{15c}$	2.47	2.59	2.58
$\Gamma'_{2c}$	4.01	3.33	3.28
$X_{1v}$	-7.78	-7.76	-7.78
$X_{4v}$	-2.90	-2.88	-2.82
$X_{1c}$	0.56	0.79	0.61
$X_{4c}$	10.38	10.23	10.11
$L'_{2v}$	-9.57	-9.61	-9.57
$L_{1v}$	-7.04	-7.01	-6.96
$L'_{3v}$	-1.25	-1.22	-1.17
$L_{1c}$	1.61	1.61	1.46
$L'_{3c}$	3.21	3.44	3.33

<sup>a</sup>Reference [5].

3.4 eV and plane wave value of 3.2 eV. The same basis set yields a value of 0.97 eV for the fundamental (indirect) gap, which is slightly underestimated when compared to the experimental, 1.17 eV and the plane-wave result, 1.2 eV. However it is still within the *GW* accuracy, which is estimated to be about  $\pm 0.1$  to  $\pm 0.2$  eV and the typical experimental error is about  $\pm 0.2$  eV. It has to be noticed that our *GW* band structure based on the all-electron Gaussian orbital approach is in good agreement with previous all-electron calculations [62, 68, 69]. A recent study [70] suggested that an insufficient number of conduction bands included in calculations [62, 68] resulted in underestimation of the band gap in all-electron approach in the previous calculations. To investigate that possibility we calculated the band gap as a function of number of conduction bands using the all-electron 88 AO basis set. The results are presented in Figure 4.2. It is clear from the plot that sufficient convergence was already achieved for 25 conduction bands. A similar result was obtained in [6].



**Table 4.4:** Calculated  $GW$  quasiparticle energies at points of high symmetry for Si (in eV) using the pseudopotential, PP 64 AO and all electron, 88 AO basis sets in a comparison with plane waves  $GW$  calculation and experimental result.

Band	PP 64 AO	88 AO	PW <sup>a</sup>	Experiment
$\Gamma_{1v}$	-11.30	-12.88	-11.57	$-12.5 \pm 0.6^b$
$\Gamma'_{25v}$	0.0	0.0	0.0	0.0
$\Gamma_{15c}$	3.20	3.33	3.24	$3.4^b$ ; $3.05^c$
$\Gamma'_{2c}$	4.78	5.72	3.94	$4.23^b$ ; $4.1^c$
$X_{1v}$	-7.75	-8.32	-7.67	
$X_{4v}$	-3.02	-3.16	-2.80	$-2.9^d$ ; $-3.3 \pm 0.2^b$
$X_{1c}$	1.28	1.04	1.34	$1.25^b$
$X_{4c}$	10.86	11.53	10.54	
$L'_{2v}$	-9.36	-10.45	-9.39	$-9.3 \pm 0.4^b$
$L_{1v}$	-7.09	-7.42	-6.86	$-6.7 \pm 0.2^b$
$L'_{3v}$	-1.31	-1.35	-1.17	$-1.2 \pm 0.2^b$ ; $-1.5^c$
$L_{1c}$	2.35	2.75	2.14	$2.1^f$ ; $2.4 \pm 0.15^e$
$L'_{3c}$	4.44	3.90	4.05	$4.15 \pm 0.1^e$
$E_g$	1.20	0.97	1.20	1.17

<sup>a</sup>Reference [5].

<sup>c</sup>Reference [64].

<sup>e</sup>Reference [66].

<sup>b</sup>Reference [56].

<sup>d</sup>Reference [65].

<sup>f</sup>Reference [67].

To investigate this further, we calculated the dynamic term of the self-energy as a function of energy and plot its real part together with the data from [5], where the pseudopotential plane wave approach is used. Results at the  $\Gamma$  point, for the valence bands,  $\Gamma_{1v}$  and  $\Gamma'_{25v}$  and lowest conduction bands,  $\Gamma_{15c}$ , are shown in Figure 4.3. The inserts show the data around the actual quasiparticle energies for the band. As we can see, there is remarkably good agreement between our calculation and data from [5] despite the plasmon-pole model used in our case. This suggests that our results are well converged with respect to the number of conduction bands at least for the states around the gap.

In conclusion, we succeeded in obtaining a good description of the quasiparticle states around the energy gap with either basis set. Since, we are mainly interested in low energy

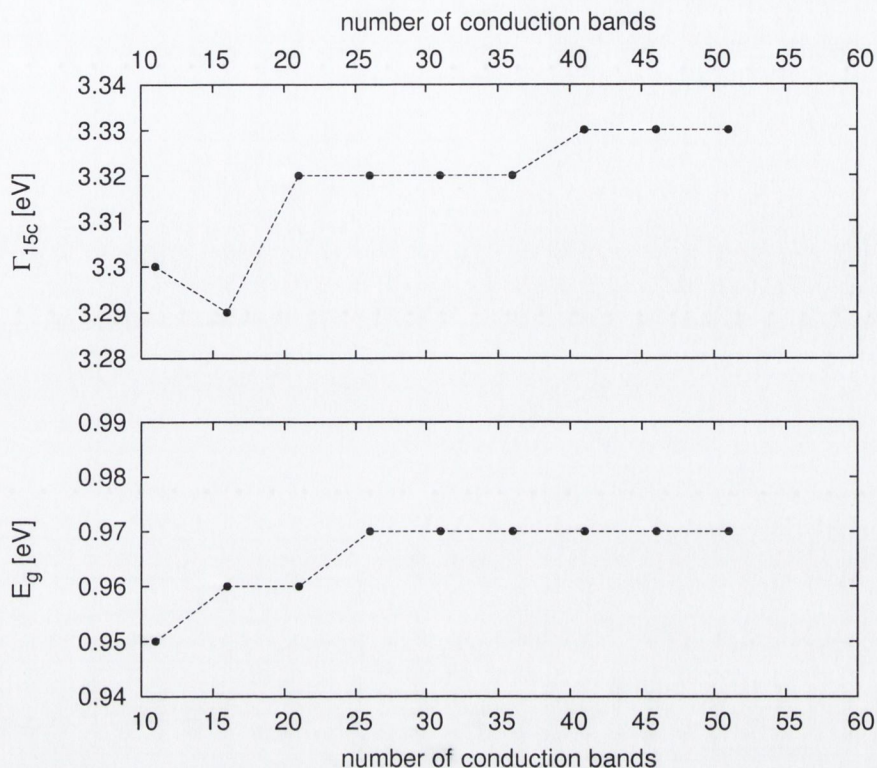


**Figure 4.2:** Direct band gap (upper panel) and fundamental gap (lower panel) for Si as a function of number of the conduction bands included in the calculation using all electron 88 AO basis set. The circles denote the calculated data and the lines are only guides to the eye.

optical spectra, and these states give the main contribution to it, our *GW* calculations should provide a good basis for its computation.

A poor of description of the higher conduction bands could be due to either our simple plasmon-pole model, which as stated in Section 3.5.1 works well only for the states around the gap. Although, there is a possibility that these bands are not well converged with respect to the number of conduction bands and a larger bases set should be developed for equally accurate descripton of the higher conduction bands. However, the number of conduction bands has been limited within the Gaussian orbital framework (see Appendix C) and it would be difficult to increase it without *f*- and *g*-type<sup>2</sup> orbital taken into calculation.

<sup>2</sup>These are not implemented in CRYSTAL95 and CRYSTAL98 codes which are used in a conjunction with our code (see Appendix A).

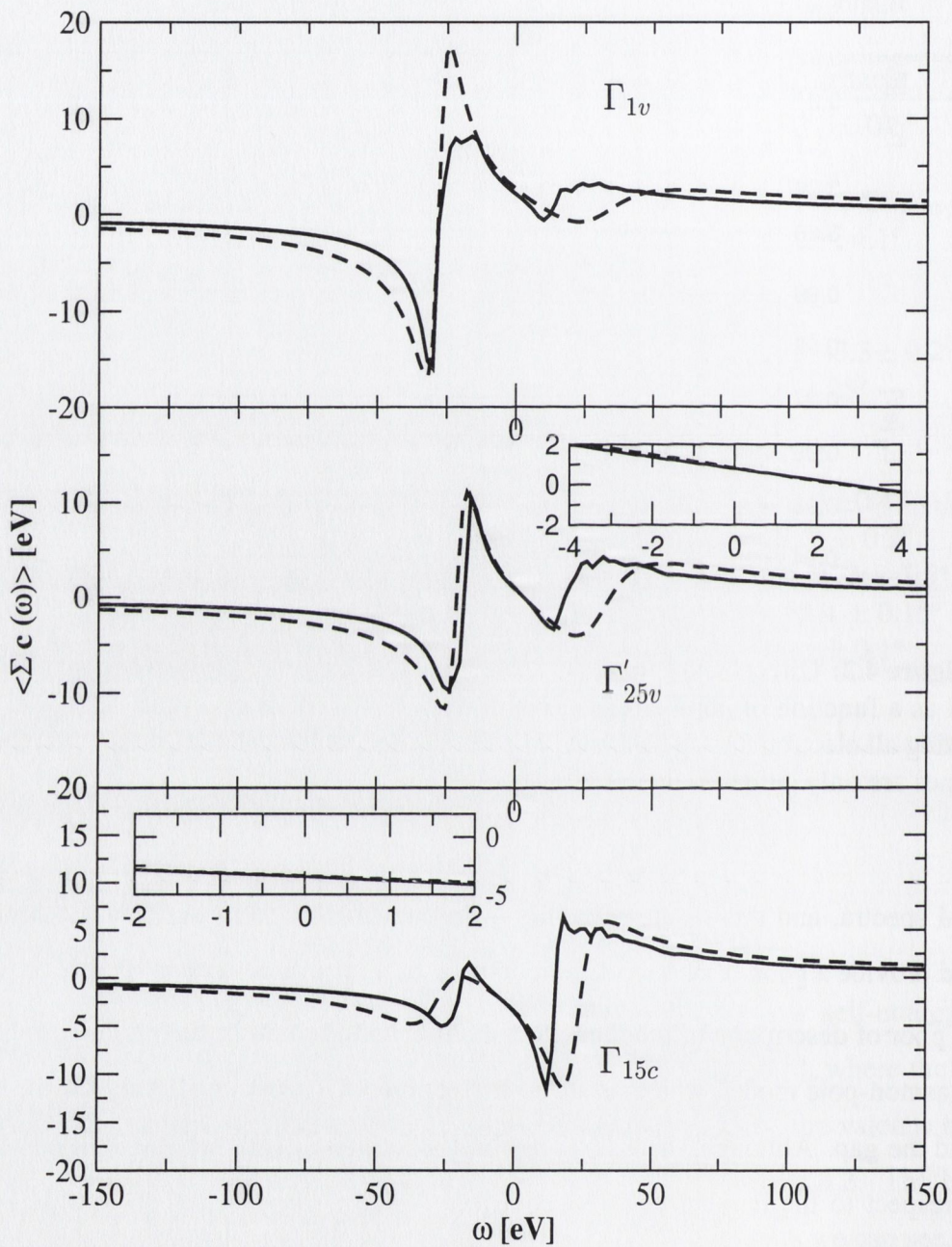


**Figure 4.3:** The correlation part of the self-energy operator at  $\Gamma$  point for Si. The solid line corresponds our calculation and the dashed line is data from [5]. The upper panel corresponds  $\Gamma_{1v}$  band,  $\Gamma'_{25v}$  is in the middle and the lower panel is  $\Gamma_{15c}$  state. Inserts show data around the actual quasiparticle energies

#### 4.1.4 Results for rare gas solids

A number of studies of the electronic structure of rare gas solids (RGS) has been reported in the past. The most recent one of the whole class is given by Bacalis *et al.* [71]. They performed an augmented-plane-wave method using the Hedin-Lundqvist local-density exchange and correlation and a simplified self-energy correction that accounts for dynamical exchange and correlation processes known as COHSEX [1, 72]. Their results are in better agreement with experimental data than those reported earlier by Kunz and Mickish [73] calculated by the HFA. Applying the quasiparticle corrections to the LDA eigenstates they improve agreement with experimental values for the band gap width, valence bands width and conduction band separation.

We calculated the band structures of RGS: Ne, Ar, Kr and Xe, using *GW* self-energy corrections as described in Chapter 3, based on the LDA eigenstates. Numerical details of the LDA and *GW* are given in Sections 4.1.1 and 4.1.2, respectively. Spin-orbit splitting is not taken into account in these calculations. Band structures of the RGS are plotted along symmetry lines in Figure 4.4. *GW* calculations are presented in solid lines while dashed lines present LDA calculations. The figure (all four panels) shows that the conduction bands have been shifted up by the *GW* correction, which improves agreement between the calculated and experimental values for band gap in each solid.

The conduction energy bands of neon (top-left on Figure 4.4) are wide and free-electron-like, which is expected for a light atomic-like neon. Namely, the RGS atoms interact with a weak van der Waals interaction, which results in valence states of the isolated RGS atoms changing only slightly when being built into a solid. Thus, the wave functions of valence electrons in neighbouring atoms overlap only slightly, however excited states overlap with the neighbouring atoms significantly which modifies the van der Waals energy in the crystal (see Ref. [74]). The effect increases in strength from Ne to Xe and it is very weak in helium. The main effect of the crystal field for Ne is to remove the degeneracy of the free-electron bands at high symmetry points e.g the lowest conduction bands at L and X. The  $\Gamma'_{25}$  conduction band is the lowest component of the eightfold degenerate free-electron state.

All  $GW$  conduction bands in Ne are uniformly shifted up by about 9 eV, which is more than 70% of the LDA energy gap. Similarly, conduction states for argon (top-right panel) are uniformly shifted up by about 4 eV which is about 30% of the LDA energy gap. The valence band width is slightly changed for these two solids. This suggests that the LDA band structures of these two solids are qualitatively correct and the so called *scissor operator* (uniform shift of conduction states to adjust to the correct band gap) can be applied for these two elements to obtain quasiparticle energies. However this trend is not present in band structures for krypton (bottom-left panel) and xenon (bottom-right panel). There is a significant dependence of the quasiparticle correction on the wave-vector  $\mathbf{q}$  in the band structure for these two solids.

Tables 4.5-4.8 give a direct comparison at high symmetry points of our LDA and  $GW$  calculations to those from [71] and experimental values where available. Table 4.5 gives data for Ne. Our  $GW$  energy gap is in excellent agreement with the experimental value [75]. The  $L'_{2v}$  band is within 30% of the measured value, while the data from [71] is in slightly better agreement with the experimental value. The difference between our data and that of [71] is significant for the  $L'_{3v}$  band, however there is no measured value for this band. At the  $X$  point the valence band width in our  $GW$  calculation and data from [71] are in good agreement. The conduction band separation,  $\Gamma'_{25c} - \Gamma_{1c}$  known as the  $s - d$  separation and conduction band widths:  $X_{1c} - \Gamma_{1c}$  and  $L_{1c} - \Gamma_{1c}$  differ from 10 to 20% between our data and data in [71] for Ne.

Data for Ar is presented in Table 4.6. Our  $GW$  energy gap is 14.02 eV, which is close to the experimental value of 14.15 eV. The valence band widths are in very good agreement with quasiparticle data from [71]. The band,  $L'_{2v}$  overestimates the experimental value by less than 20%. However, the  $s - d$  separation and conduction bands widths  $X_{1c} - \Gamma_{1c}$  and  $L_{1c} - \Gamma_{1c}$  were all overestimated at the LDA level and they were worsened by the  $GW$  correction.

As was the case for Ar, for both Kr (Table 4.7) and Xe (Table 4.8), the  $GW$  energy gaps,  $\Gamma_{1c}$  are in good agreement with experimental values. Values for the valence band width at band  $L'_{2v}$  are improved by  $GW$  correction and they are in good agreement with

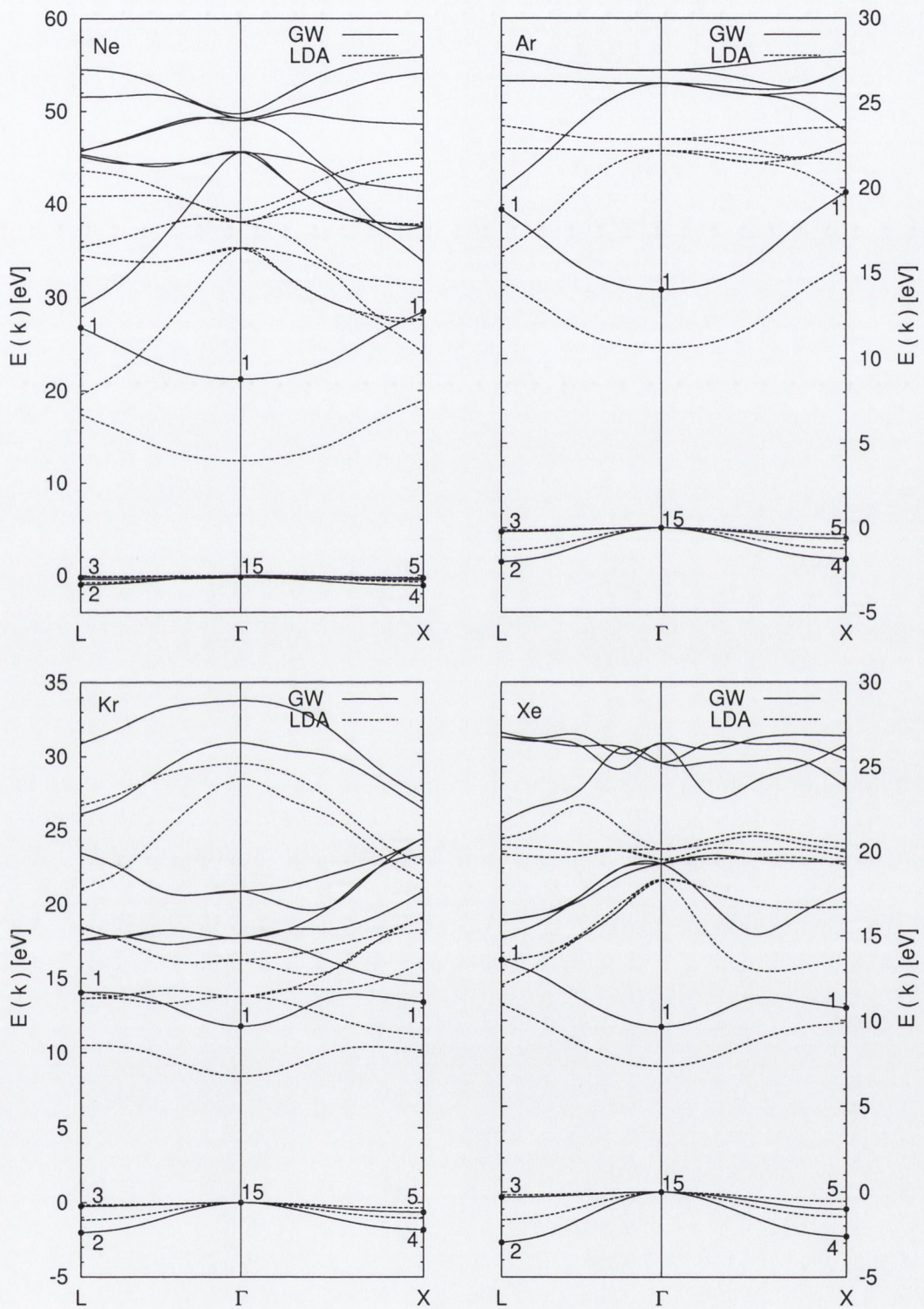


**Figure 4.4:** Band structures for RGS: top-left panel Ne, top-right Ar, bottom-left Kr and bottom-right Xe. GW calculation (solid line) and LDA (dashed line)

**Table 4.5:** Energies (eV) at high-symmetry points for solid neon. The second and third columns correspond to this work (labeled as a LDA and  $GW$ , respectively). The fourth and the last columns are quasiparticle states from [71] and experimental values, respectively.

Bands	LDA	GW	Ref [71]	Experiment
$\Gamma_{15v}$	0.0	0.0	0.0	0.0
$\Gamma_{1c}$	12.44	21.56	16.56	21.42 <sup>a</sup>
$X'_{4v}$	-0.71	-1.09	-0.88	
$X'_{5v}$	-0.23	-0.31	-0.30	
$L'_{2v}$	-0.79	-0.87	-0.99	-1.306 <sup>b</sup>
$L'_{3v}$	-0.078	-0.21	-0.09	
$\Gamma'_{25c} - \Gamma_{1c}$	22.81	24.37	20.51	
$X_{1c} - \Gamma_{1c}$	6.48	7.18	8.12	
$L_{1c} - \Gamma_{1c}$	5.03	5.53	7.21	

<sup>a</sup>Reference [75].                      <sup>b</sup>Reference [76].

**Table 4.6:** Energies (eV) at high-symmetry points for solid Ar. This work is presented in the second (LDA) and third ( $GW$ ) columns, the fourth column corresponds to published data and the last column gives the experimental data.

Bands	LDA	GW	Ref [71]	Experiment
$\Gamma_{15v}$	0.0	0.0	0.0	0.0
$\Gamma_{1c}$	10.63	14.01	11.96	14.15 <sup>a</sup>
$X'_{4v}$	-1.23	-1.85	-1.73	
$X'_{5v}$	-0.40	-0.55	-0.63	
$L'_{2v}$	-1.34	-2.02	-1.92	-1.700 <sup>b</sup>
$L'_{3v}$	-0.14	-0.22	-0.20	
$\Gamma'_{25c} - \Gamma_1$	11.56	12.13	8.44	5.197
$X_{1c} - \Gamma_{1c}$	4.85	5.70	3.10	2.35
$L_{1c} - \Gamma_{1c}$	3.89	4.70	3.50	1.646

<sup>a</sup>Reference [75].                      <sup>b</sup>Reference [76].

**Table 4.7:** Quasiparticle energies (eV) at high-symmetry points for solid Kr. For explanation of the columns see Table 4.5 or 4.6

Bands	LDA	GW	Ref [71]	Experiment
$\Gamma_{15v}$	0.0	0.0	0.0	0.0
$\Gamma_{1c}$	8.43	11.75	9.99	11.61 <sup>a</sup>
$X'_{4v}$	-1.06	-1.87	-1.700	
$X'_{5v}$	-0.36	-0.70	-0.64	
$L'_{2v}$	-1.18	-2.07	-1.88	-2.30 <sup>b</sup>
$L'_{3v}$	-0.15	-0.29	-0.22	
$\Gamma'_{25c} - \Gamma_1$	5.35	5.97	7.36	5.197
$X_{1c} - \Gamma_{1c}$	1.70	1.63	2.57	2.20
$L_{1c} - \Gamma_{1c}$	2.06	2.27	2.88	1.50

<sup>a</sup>Reference [75].                      <sup>b</sup>Reference [76].

**Table 4.8:** Energies (eV) at high-symmetry points for solid Xe. This work is presented in the second (LDA) and third (GW) columns. The last two columns are theoretical and experimental data (see Table 4.5).

Bands	LDA	GW	Ref [71]	Experiment
$\Gamma_{15v}$	0.0	0.0	0.0	0.0
$\Gamma_{1c}$	7.33	9.63	8.23	9.32 <sup>a</sup>
$X'_{4v}$	-1.46	-2.61	-1.52	
$X'_{5v}$	-0.55	-1.01	-0.59	
$L'_{2v}$	-1.64	-2.96	-2.08	-3.01 <sup>b</sup>
$L'_{3v}$	-0.17	-0.30	-0.26	
$\Gamma'_{25c} - \Gamma_1$	10.95	9.64	5.43	3.70
$X_{1c} - \Gamma_{1c}$	2.54	1.11	1.53	2.00
$L_{1c} - \Gamma_{1c}$	3.04	3.95	2.00	1.61

<sup>a</sup>Reference [75].                      <sup>b</sup>Reference [76].



the experimental values for either solid, while the data from [71] is underestimated. Good agreement with the experimental values for  $L'_{2v}$  encourages us to believe that our data is closer to the realistic values at the  $X$  point and at  $L'_{3v}$ , even if it does not agree well with data in [71]. It is important to mention that the magnitudes of spin-orbit interaction for Kr and Xe are  $E_{so} = 0.64$  eV and  $E_{so} = 1.3$  eV [77], respectively, which are quite important and we cannot expect good band structure without inclusion of relativistic effects in the calculation.

The  $s - d$  separation is overestimated at the LDA level for all four solids and it is increased by the  $GW$  correction for Ne, Ar and Kr, so the agreement with experimental values worsens. Similar results were obtained in [71]. Although the  $s - d$  separation for Xe was decreased by the  $GW$  correction in our calculation, it still overestimates the measured value by more than 60%. The conduction band widths,  $X_{1c} - \Gamma_{1c}$  and  $L_{1c} - \Gamma_{1c}$  are not in very good agreement with experimental values for either Ar, Kr, or Xe. As was case in the all-electron Gaussian orbital basis silicon calculation (see discussion in the previous subsection) all of these omissions can be explained by the following: (1) a lack of the convergence with respect to the number of conduction bands in the  $GW$  calculation, particularly the higher conduction bands are more sensitive on that number and (2) the plasmon-pole model used in the calculation, which can describe the energy dependence of the dielectric function only below and around the gap values. In addition, omission of the spin-orbit interaction contributed to the poorer band structures for Kr and Xe.

The  $GW$  correction generally improved the band gap for all four rare gases. Figure 4.5 illustrates the fundamental gap in our  $GW$  and LDA calculations and experimental values for all four rare gases. When going from Ne to Xe, both the LDA and the  $GW$  approximations show a decrease in the fundamental gap. The corrected  $GW$  gap is in good agreement with the experimental value for all four solids. Figure 4.6 illustrates the valence band width for all four gases and compares our LDA and  $GW$  calculations with experimental data. Again, it is shown that the  $GW$  correction improved the valence bands, and our  $GW$  values came close to the experimental values. The valence band

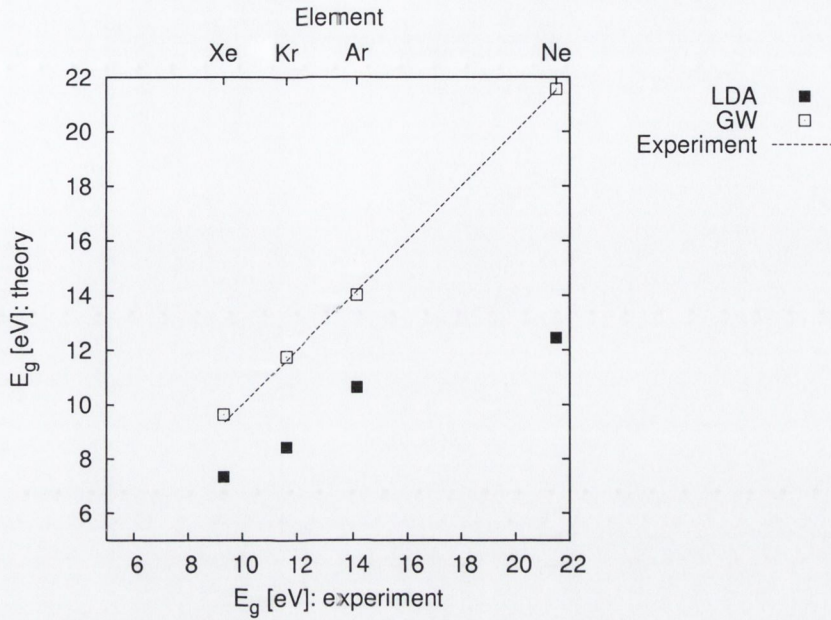


**Figure 4.5:** Calculated band gap energies (in eV) for the RGS (symbols) vs. experimental values, 45° line presents ideal values

width increased when going from lighter Ne to Xe in both LDA and *GW* approximation which is consistent with experimental measurements. From Tables 4.5-4.8 we can see the trend in decrease of the conduction band separation when going from Ne to Xe which is observed experimentally. The LDA and GWA confirm that trend from Ne to Kr, however the higher conduction bands in Xe are in a strong disagreement with experimental values and its *s* – *d* separation does not fit in the mentioned trend.

Finally, the self-energy correction gives reliable band structure for the valence bands and the first conduction band, i.e, energy gap, however the higher conduction bands are not very accurate. Even, if the reasons for this could be explained by the disadvantages of the Gaussian orbital basis set mentioned above, a similar discrepancy was obtained by Bacalis *et al.* [71] when an APW model was used. Our results are applied in the calculation of the low energy optical spectrum, where the transitions between top valence *p* state and bottom conduction *s* state give the main contribution to the spectrum and is not sensitive to the higher conduction bands.

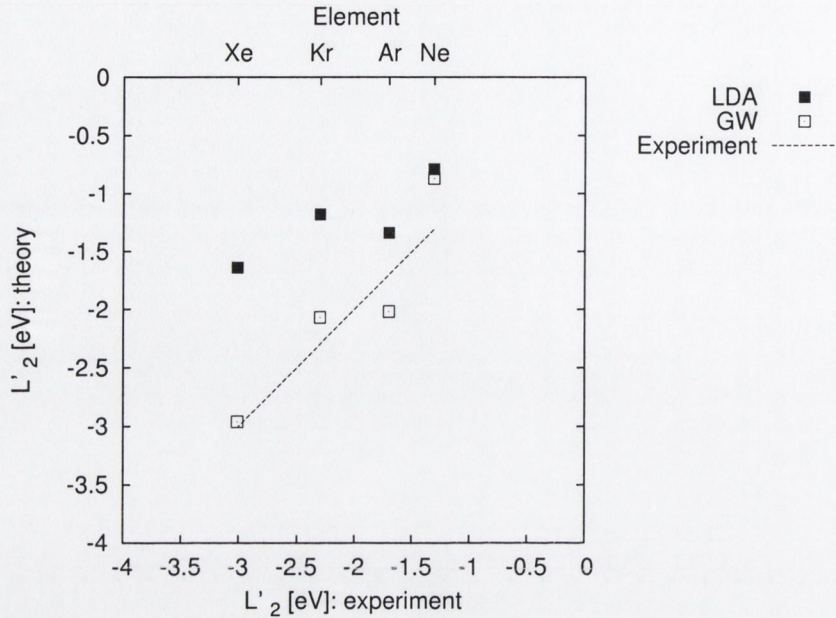


**Figure 4.6:** Theoretical energies (in eV) at  $L'_{2v}$  for the RGS (symbols). As in Figure 4.5, ideal values are presented by 45° line.

## 4.2 Quasiparticle band structure for $\text{Cu}_2\text{O}$

The recent discovery of high-temperature superconductivity [78] in ceramic oxides containing copper has rekindled interest in studying the electronic structure of copper oxides in more detail. Copper oxides exist in two stable forms, cuprous oxide  $\text{Cu}_2\text{O}$  and cupric oxide  $\text{CuO}$ .

Cuprous oxide is of interest in the present work. There are two interesting features of cuprous oxide: Firstly, it crystallizes in the cuprite structure [79] which is unusual and described in 4.2.1. Another interesting feature of  $\text{Cu}_2\text{O}$  is the excitonic spectrum [80, 81] which is not considered in this thesis due to strong spin-orbit coupling.

Many theoretical studies of the electronic structure of  $\text{Cu}_2\text{O}$  have been reported in the past. Some of the earliest studies were performed by Kleinman and Mednick [82] using the Hartree-Fock-Slater method, by Dahl and Switendick [83] using a non-self-consistent augmented plane wave method and by Robertson [84] using a tight-binding approach. More recently, Ching *et. al.* [85] reported a study of the ground state and interband optical properties within the DFT using orthogonalised linear combination of atomic orbitals

and Ruiz *et. al.* [78] reported study of the electronic and structural properties with a self-consistent Hartree-Fock approximation. There is no reported study of the electronic structure of  $\text{Cu}_2\text{O}$  with a  $GW$  approximation based on Hartree-Fock eigenstates that we are aware of. The main aim of this section is to investigate quasiparticle band structure using the  $GW$ -HFA approach described in Section 3.3.2.

### 4.2.1 Crystal structure

A particularly attractive feature of  $\text{Cu}_2\text{O}$  is the cuprite structure, consists of a BCC array of oxygen atoms with Cu ions inserted between consecutive oxygen layers, in such way that each oxygen atom is surrounded by a tetrahedron of copper atoms. Each copper atom is bonded by two oxygen atoms forming a linear unit O-Cu-O, (see Figure 4.7). Alternatively, the structure can be described as two interpenetrating frameworks, each one equivalent to the  $\text{SiO}_2$  cristobalite structure [86] and there is a weak interaction between two frameworks. The cuprite structure has high symmetry with space group  $Pn\bar{3}m$  ( $O_h^4$ ). An unusually short Cu-O bond length of 1.85 Å, indicates the existence of covalent bonding between Cu and O. The Mulliken population analysis in our self-consistent Hartree-Fock calculation gave values of  $+1.05e$  and  $-2.1e$  for the charges of Cu and O, respectively. This confirms a fully ionic picture. Some earlier theoretical works were contradictory about this, Ruiz *et. al.* [78] obtained an ionic structure with some Cu-O covalent character, Ching *et. al.* [85] obtained a quasi-neutral description with a small negative charge on the Cu ions. Restori and Schwarzenbach [87] fitted orbitals of the experimental x-ray electron density showing that  $\text{Cu}_2\text{O}$  is a fully ionic crystal.

The Hartree-Fock calculation was carried out using the CRYSTAL95 [26] code. An all-electron basis set is employed giving a total of 180 atomic orbitals per unit cell. A detailed description of the basis set is given in Appendix C. The experimental value for the lattice constant,  $a_0 = 4.2696$  Å, used in the calculation is taken from [88]. A spin-orbit interaction is not included in the present work.

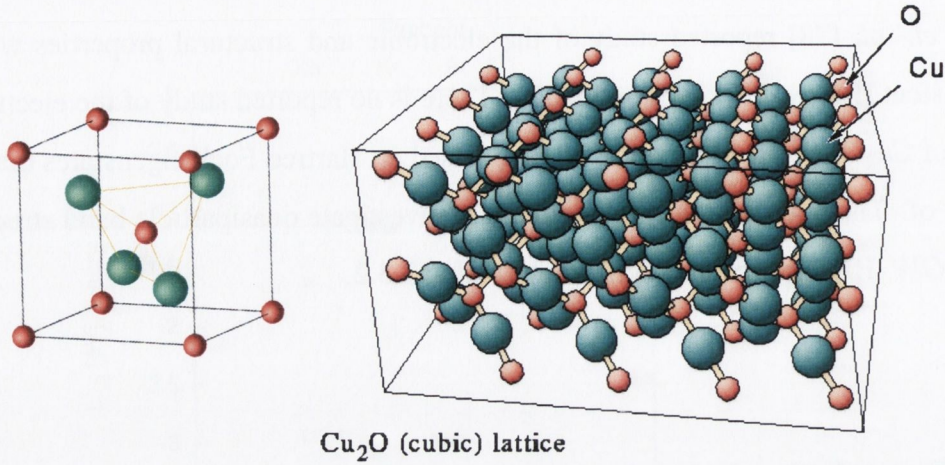


**Figure 4.7:** Crystal structure of Cu<sub>2</sub>O: primitive cell (left) and supercell structure (right). Green balls correspond to Cu atoms and red ones to O atoms. Figure of the supercell was taken from <http://www.fhi-berlin.mpg.de/personal/hermann>.

## 4.2.2 Self-energy calculation

The self-energy matrix element in *GW*-HFA includes only the dynamic part,

$$\begin{aligned}
 \langle m\mathbf{k} | \Sigma(E) | m\mathbf{k} \rangle &= \frac{4\pi^2 e^2}{\Omega} \sum_{\mathbf{q}, \mathbf{G}, \mathbf{G}'} \sum_n \frac{\langle m\mathbf{k} | e^{-i(\mathbf{q}+\mathbf{G})\cdot\mathbf{r}} | n\mathbf{k} + \mathbf{q} \rangle \langle n\mathbf{k} + \mathbf{q} | e^{i(\mathbf{q}+\mathbf{G}')\cdot\mathbf{r}'} | m\mathbf{k} \rangle}{|\mathbf{q} + \mathbf{G}| |\mathbf{q} + \mathbf{G}'|} \\
 &\times \sum_l V_{l,-\mathbf{G}}(-\mathbf{q}) V_{l,-\mathbf{G}'}^*(-\mathbf{q}) \left[ \frac{z_{-\mathbf{q}l} \omega_{-\mathbf{q}l}}{2} \frac{1}{E - E_{n\mathbf{k}+\mathbf{q}} - \omega_{-\mathbf{q}l}} \right] \quad (4.7)
 \end{aligned}$$

since the Hartree-Fock exchange is already included in the self-consistent Hartree-Fock calculation (see Equation 3.21). The sum over  $\mathbf{q}$ -vectors is carried out using a special points by Monkroost and Pack [60] for a simple cubic lattice. Two special points in the IBZ and their stars and 27 reciprocal lattice vectors,  $\mathbf{G}$  and  $\mathbf{G}'$  produced the result converged within 0.01 eV. The sum over bands,  $n$  involves both occupied and conduction states. We found that the core states (Cu 1s,2s,3s,2p,3p and O 1s) do not contribute to the final *GW*-HFA results, significantly. Inclusion of these states decreased the band gap by only 0.03 eV. This is not surprising due to the large binding energies of these states.

The divergence for the case  $\mathbf{q} \rightarrow 0$  and  $\mathbf{G} = \mathbf{G}' = 0$  was treated using the auxiliary function technique given by Equation (4.4) and Table 4.2. The special integrals  $\langle m\mathbf{k} | e^{-i\mathbf{Q}\cdot\mathbf{r}} | n\mathbf{k} + \mathbf{q} \rangle$  in (4.7) are computed as described in Section 4.1.2. The full RPA

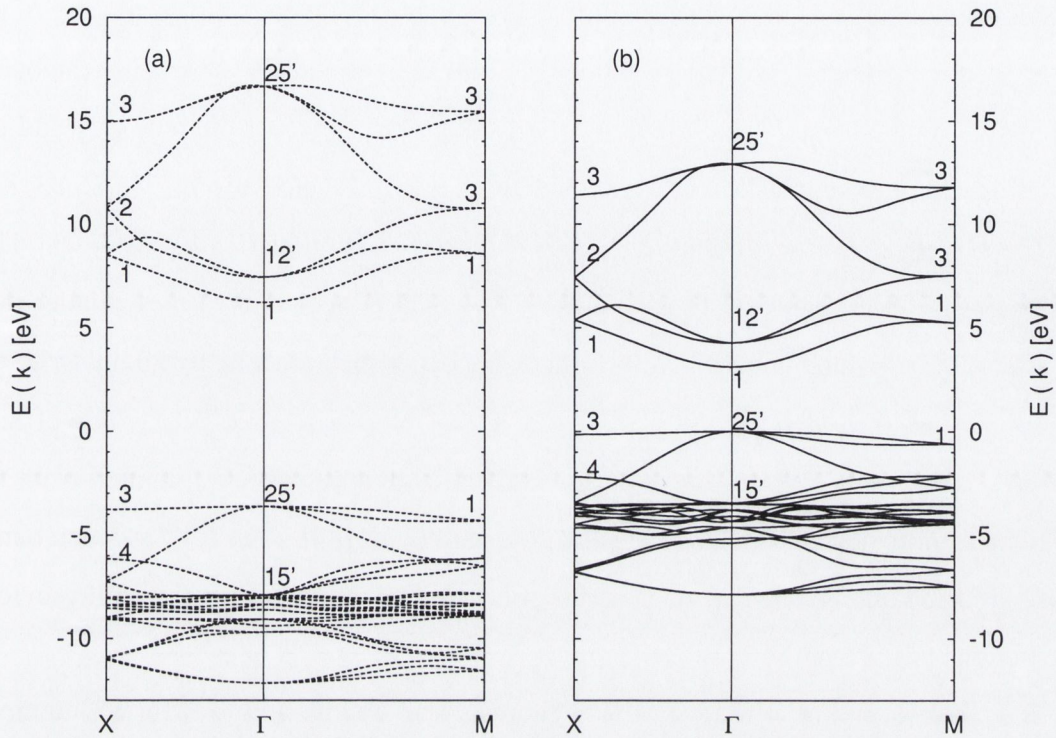


**Figure 4.8:** Electronic band structure for  $\text{Cu}_2\text{O}$ : (a) A self-consistent Hartree-Fock and (b) Quasiparticle  $GW$ -HFA calculation. All bands refer to the top of the quasiparticle valence band set to 0 eV.

dielectric matrix was calculated at each  $\mathbf{q}$  point and at the  $\mathbf{q} \rightarrow 0$  limit. In the dielectric matrix calculation 216  $\mathbf{k}$ -points were used in the simple cubic BZ to perform the integration over the zone.

### 4.2.3 Results

Calculated band structures for  $\text{Cu}_2\text{O}$  are presented in Figure 4.8. The figure compares the self-consistent Hartree-Fock band structure, panel (a) with the  $GW$ -HFA calculation in panel (b). The results of both methods show the existence of the direct gap at the  $\Gamma$  point, which is consistent with experimental observations [80] and earlier calculations [78, 82, 83, 84, 85]. The band gap and valence band width are highlighted in Table 4.9. The Hartree-Fock band gap is 9.84 eV, which is in strong disagreement with the experimental value of 2.17 eV from [80] obtained by optical absorption. This fact reflects the well-

known characteristic of the periodic Hartree-Fock method and does not permit use of the methodology for the interpretation of the excitonic spectrum of  $\text{Cu}_2\text{O}$  because the band-gap energy enters directly into the absorption spectrum. However the topology and the main features of the band structure agree well with previous calculations [78, 82, 83, 84].

The  $GW$  calculation shifted the valence bands up and conduction bands down. This resulted in the band gap of 3.12 eV (3.09 eV)<sup>3</sup>, which is by about 3 times smaller than the Hartree-Fock value but still overestimates the experimental value by about 40%. On the other hand, the valence band width is changed from the Hartree-Fock value of 8.55 to 7.84 eV, which is close to the experimental estimate around 8 eV obtained from the ultraviolet photoelectron spectroscopy by Ghijsen *et. al.* [89]. The  $GW$  valence bands are plotted separately in Figure 4.9 and topology of the structure agrees with previous calculations [78, 82, 85].

The overestimation of the  $GW$ -HFA gap was also obtained in [42] for Si, diamond and MgO where  $GW$ -HFA was used. Reasons for this were attributed to the use of the exaggerated Hartree-Fock eigenvalues in [42], since the gaps in all Si, diamond (see [6] and Section 4.1.3) and MgO [4] were described by  $GW$ -LDA with an accuracy of order 0.1 eV. The overestimation of the  $GW$  band gap of  $\text{Cu}_2\text{O}$  can also be due to use of the Hartree-Fock eigenvalues, and LDA eigenstates could be a better starting point in this case. We performed LDA calculation with CRYSTAL95/98 for  $\text{Cu}_2\text{O}$  which failed to converge. It would be worthwhile to apply a self-consistent  $GW$  calculation for this material. Finally, inclusion of the spin-orbit interaction is also essential for accurate description of the band structure for  $\text{Cu}_2\text{O}$  [80].

---

<sup>3</sup>The result in the brackets indicates the value obtained with all core electrons taken into calculation.

**Table 4.9:** Hartree-Fock (HF) and  $GW$  results for the band gap  $E_g$  and valence band width for  $\text{Cu}_2\text{O}$  from the present calculation compared to the experimental values. All energies are given in eV.

	HF	$GW$	Expt.
$E_g$	9.84	3.1	2.17 <sup>a</sup>
$E_{VB}$	8.55	7.8	about 8 <sup>b</sup>

<sup>a</sup>Reference [80].

<sup>b</sup>Reference [89].

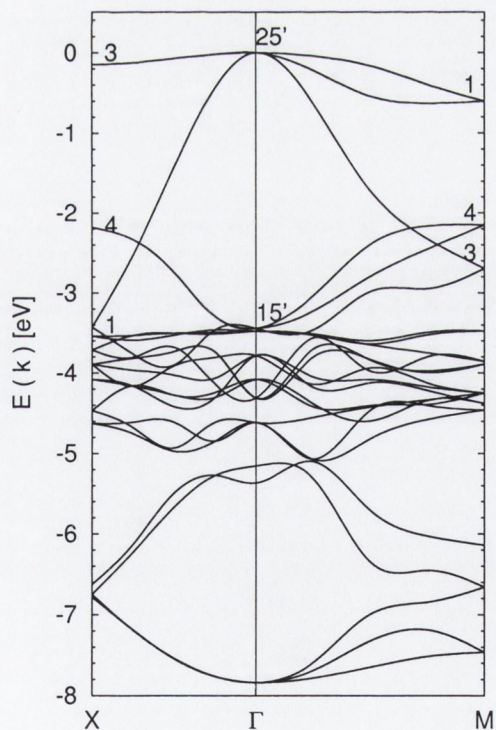


**Figure 4.9:** Electronic valence band structure for  $\text{Cu}_2\text{O}$  computed by the  $GWA$ .



The first part of the paper is devoted to the derivation of the equations of motion for the system. The second part is devoted to the numerical solution of these equations. The third part is devoted to the discussion of the results.

The equations of motion for the system are derived from the Lagrangian formalism. The Lagrangian is given by

$$L = \frac{1}{2} \sum_{i,j} \dot{q}_i \dot{q}_j G_{ij} - V(q_1, q_2, \dots, q_n)$$

where  $G_{ij}$  is the metric tensor and  $V$  is the potential energy. The equations of motion are then derived from the Euler-Lagrange equations.

The numerical solution of these equations is obtained using the Runge-Kutta method. The results are shown in Figure 1.

The results show that the system exhibits chaotic behavior for certain parameter values. This is characterized by a sensitive dependence on initial conditions and a dense set of periodic orbits. The Lyapunov exponent is used to quantify the degree of chaos in the system.

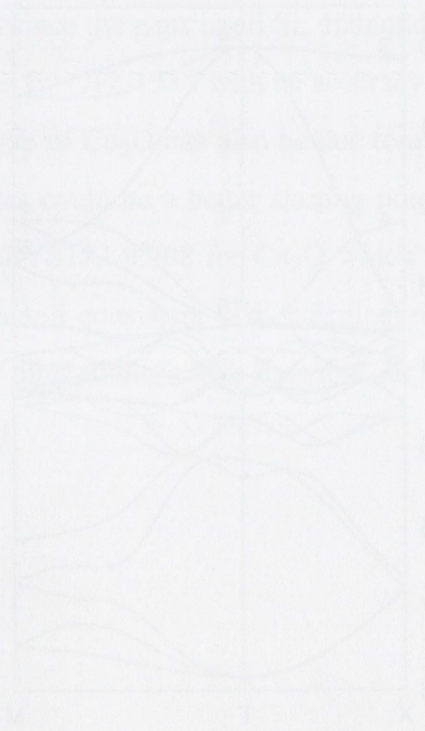


Figure 1: Time evolution of the system's coordinates. The plot shows several curves representing the trajectories of the system over time. The curves exhibit complex, oscillatory behavior, characteristic of a chaotic system. The x-axis represents time, and the y-axis represents the coordinates. The trajectories are highly sensitive to initial conditions, as evidenced by the divergence of nearby paths over time.

## Chapter 5

# Optical Spectra and Electron-Hole Excitations

The optical spectra of solids provide extremely useful information about the character of materials. Optical excitations provide the basis for a vast range of technical applications, including laser technology, light-emitting devices and photovoltaics. In this context, it is important to describe and predict optical properties by a reliable and efficient theory.

Modern *ab initio* techniques have been used to study many properties of solids for many years. DFT has been proven as a very powerful tool for studying ground state properties and the GWA has been very successful for calculation of electron self-energies and quasiparticle band structures. However, neither of these theories leads to an accurate description of the optical spectrum. The cause of it lies in the fact that these theories deal with single-particle states only, and do not describe a key aspect of the optical absorption process: the electron-hole interaction. When a photon is absorbed, an electron in the valence band is excited into the conduction band leaving a hole behind. Single-particle theories regard the excited electron and hole as independent, noninteracting particles. However, the excited electrons and holes do interact and form bound states called excitons. This effect is especially pronounced in a wide gap insulators, where the electron-hole interaction is strong due to insufficient screening. In these systems electron-hole effects can dominate the spectrum and wash out the features found in the one-electron spectrum.

More than two decades ago, Hanke and Sham introduced a scheme in which the electron-hole interaction can be included [9, 10]. The approach relies on calculation of an electron-hole propagator, which describes the dynamics of the electron-hole pair in a quantum many-body system. Due to its computationally complex nature, it had been limited to simple situations or to simplifying model approximations for many years.

Only recently, the Hanke-Sham approach was applied together with single-particle energies and wave functions from LDA and quasiparticle calculations. An efficient algorithm for calculating electron-hole bound states and electron-hole wave functions based on the Hanke-Sham approach has been proposed by Rohlfing *et al.* [13]. This approach is adopted in this work and presented in this chapter.

This chapter is organised as follows: Section 5.1 gives a theoretical overview of the dielectric response and dielectric tensor. The electron-hole propagator and Bethe-Salpeter equation [8] are presented in Section 5.2. Section 5.3 gives details about the electron-hole interaction kernel. The spin structure of the electron-hole states and the optical spectrum are presented in Sections 5.4 and 5.5, respectively. Finally, numerical techniques are given in Section 5.6.

## 5.1 Linear Dielectric Response

The dielectric response of the system placed in an external field,  $\mathbf{E}(\mathbf{r}, \omega)$  can be described by introducing the dielectric constant tensor  $\varepsilon_{ij}$  which gives relation between induced electric displacement  $\mathbf{D}(\mathbf{r}, \omega)$  and external field [90]:

$$\mathbf{D}_i = \varepsilon_{ij} \mathbf{E}_j(\mathbf{r}, \omega) \quad (i, j = 1, 2, 3) \quad (5.1)$$

In the crystalline case, it is appropriate to exploit lattice translation symmetry to transform expression (5.1) to a reciprocal-space basis with the following convention used:

$$\varepsilon_{ij}(\mathbf{r}, \mathbf{r}', \omega) = \frac{1}{\Omega} \sum_{\mathbf{q}, \mathbf{G}, \mathbf{G}'} e^{i(\mathbf{q}+\mathbf{G})\cdot\mathbf{r}} \varepsilon_{ij}(\mathbf{q} + \mathbf{G}, \mathbf{q} + \mathbf{G}', \omega) e^{-i(\mathbf{q}+\mathbf{G}')\cdot\mathbf{r}'} \quad (5.2)$$

Here  $\Omega$  denotes the crystal volume, the wave vector  $\mathbf{q}$  is restricted to lie inside the first Brillouin zone and  $\mathbf{G}$  and  $\mathbf{G}'$  span the (infinite) reciprocal lattice. By this we obtain

the wavevector and frequency dependent dielectric function,  $\varepsilon_{ij}(\mathbf{q} + \mathbf{G}, \mathbf{q} + \mathbf{G}', \omega)$ . As originally introduced by Lindhard [91], one can now define longitudinal and transverse components of the the dielectric function,  $\varepsilon_{\parallel}(\mathbf{q} + \mathbf{G}, \mathbf{q} + \mathbf{G}', \omega)$  and  $\varepsilon_{\perp}(\mathbf{q} + \mathbf{G}, \mathbf{q} + \mathbf{G}', \omega)$ , respectively. However for the case of cubic symmetry, there is only one linearly independent component and can be shown that those two components are equivalent,  $\varepsilon_{\parallel} = \varepsilon_{\perp}$  in long-wavelength limit which is relevant in the current work (see text below). From now, we will consider only the longitudinal component<sup>1</sup> and the index  $\parallel$  will be left out for clarity. Also, it is common to write  $\varepsilon(\mathbf{q} + \mathbf{G}, \mathbf{q} + \mathbf{G}', \omega)$  in a matrix form:  $\varepsilon_{\mathbf{G}\mathbf{G}'}(\mathbf{q}, \omega)$ .

We can now return to relation (5.1). By considering only the longitudinal dielectric function and transforming (5.1) into reciprocal space it can be shown that a small change in external potential  $\delta V^{ext}(\mathbf{q} + \mathbf{G})$  of wave vector  $\mathbf{q} + \mathbf{G}$  will induce microscopic fields in the crystal of a different wave vector  $\mathbf{q} + \mathbf{G}'$  and change in total potential is given by:

$$\delta V^{tot}(\mathbf{q} + \mathbf{G}', \omega) = \sum_{\mathbf{G}} \varepsilon_{\mathbf{G}\mathbf{G}'}^{-1}(\mathbf{q}, \omega) \delta V^{ext}(\mathbf{q} + \mathbf{G}, \omega). \quad (5.3)$$

These microscopic fields arise from the crystal inhomogeneity and they have been termed *local field effects* [9].

Following the Hanke and Sham [9] approach, as a first step of the calculation of the dielectric function, we define the density response function or irreducible polarisability,  $P_{\mathbf{G}\mathbf{G}'}(\mathbf{q}, \omega)$ , which relates induced charge density caused by a change in external potential,

$$\delta \rho(\mathbf{q} + \mathbf{G}, \omega) = \sum_{\mathbf{G}'} P_{\mathbf{G}\mathbf{G}'}(\mathbf{q}, \omega) \delta V^{ext}(\mathbf{q} + \mathbf{G}', \omega). \quad (5.4)$$

From Equations (5.3) and (5.4) one can express the dielectric matrix in terms of the polarisability as

$$\varepsilon_{\mathbf{G}\mathbf{G}'}(\mathbf{q}, \omega) = \delta_{\mathbf{G}\mathbf{G}'} - v(\mathbf{q} + \mathbf{G}) P_{\mathbf{G}\mathbf{G}'}(\mathbf{q}, \omega) \quad (5.5)$$

where  $v(\mathbf{q} + \mathbf{G}) = 4\pi e^2 / \Omega |\mathbf{q} + \mathbf{G}|^2$  is a Fourier component of the Coulomb potential. Within the single-particle picture, in a traditional random phase approximation (RPA)

---

<sup>1</sup>In the more general case one should calculate the transverse dielectric constant for studying the optical properties since, light is a transverse electromagnetic wave.

obtained by Adler [27] and Wiser [92] the polarisability is given by  $P_{\mathbf{G}\mathbf{G}'} = P_{\mathbf{G}\mathbf{G}'}^0$ ,

$$P_{\mathbf{G}\mathbf{G}'}^0(\mathbf{q}, \omega) = \frac{2}{\Omega} \sum_{n, n'} \sum_{\mathbf{k}} \frac{f(E_{n'\mathbf{k}+\mathbf{q}}) - f(E_{n\mathbf{k}})}{E_{n'\mathbf{k}+\mathbf{q}} - E_{n\mathbf{k}} - \omega - i0^+} \\ \times \langle n'\mathbf{k} + \mathbf{q} | e^{i(\mathbf{q}+\mathbf{G})\cdot\mathbf{r}} | n\mathbf{k} \rangle \langle n\mathbf{k} | e^{-i(\mathbf{q}+\mathbf{G}')\cdot\mathbf{r}'} | n'\mathbf{k} + \mathbf{q} \rangle. \quad (5.6)$$

Here,  $f(E)$  denotes the Fermi function,  $n, n'$  are band indices labeling the Bloch eigenstates  $|\mathbf{k}, n\rangle$  of energy  $E_n(\mathbf{k})$  in the solid, and the sum over  $\mathbf{k}$  is performed inside the full Brillouin zone, a spin has been integrated over. If we restrict ourselves to the contribution from  $\mathbf{G} = \mathbf{G}' = 0$ , the dielectric matrix given by Equation (5.5) in a limit of vanishingly small  $\mathbf{q} \rightarrow 0$  is related to the macroscopic dielectric function  $\varepsilon_M$  by

$$\varepsilon_M(\omega) = \lim_{\mathbf{q} \rightarrow 0} \varepsilon_{00}(\mathbf{q}, \omega). \quad (5.7)$$

In that case Equations (5.5-5.6) yields to the standard intraband macroscopic dielectric function, known as Cohen-Enhrenreich [93], without local field effects included. The local fields can be included by calculating the symmetrised entire dielectric matrix,  $\varepsilon_{\mathbf{G}\mathbf{G}'}$  [94],

$$\varepsilon_{\mathbf{G}\mathbf{G}'}(\mathbf{q}, \omega) = \delta_{\mathbf{G}\mathbf{G}'} + \frac{16\pi e^2}{\Omega} \frac{1}{|\mathbf{q} + \mathbf{G}| |\mathbf{q} + \mathbf{G}'|} \\ \times \sum_{v, c} \sum_{\mathbf{k}} \frac{\langle c\mathbf{k} + \mathbf{q} | e^{i(\mathbf{q}+\mathbf{G})\cdot\mathbf{r}} | v\mathbf{k} \rangle \langle v\mathbf{k} | e^{-i(\mathbf{q}+\mathbf{G}')\cdot\mathbf{r}'} | c\mathbf{k} + \mathbf{q} \rangle}{E_{c, \mathbf{k}+\mathbf{q}} - E_{v, \mathbf{k}} - \omega - i0^+} \quad (5.8)$$

then the macroscopic dielectric function is given as the inverse of the head of the numerically inverted dielectric matrix [9],

$$\varepsilon_M^{LF} = \lim_{\mathbf{q} \rightarrow 0} 1/[\varepsilon_{\mathbf{G}\mathbf{G}'}^{-1}(\mathbf{q}, \omega)]_{00}. \quad (5.9)$$

Equation (5.8) applies to semiconductors and insulators where  $v$  and  $c$  correspond to valence and conduction bands, respectively.

On the other side, if  $P$  includes the electron-hole interaction, then it can be defined by the electron-hole correlation function,  $L$  [95]

$$P(\mathbf{r}, \mathbf{r}', \omega) = -iL(\mathbf{r}, \mathbf{r}', \mathbf{r}, \mathbf{r}', \omega) \quad (5.10)$$

then Equations (5.5) and (5.7) give us all necessary information about dielectric properties [9] and  $\varepsilon_M(\omega)$  obeys

$$\varepsilon_M(\omega) = 1 - \lim_{\mathbf{q} \rightarrow 0} \frac{4\pi e^2}{\Omega q^2} P_{00}(\mathbf{q}, \omega). \quad (5.11)$$

The macroscopic dielectric function is addressed again in Section 5.5. In the following few sections, the method for calculation of  $L$  from the Bethe-Salpeter equation is presented.

## 5.2 The Bethe-Salpeter Equation

In this section we investigate electron-hole excitations of type:

$$|N, 0\rangle \longrightarrow |N, S\rangle, \quad (5.12)$$

where  $|N, 0\rangle$  and  $|N, S\rangle$  are the ground and excited states, respectively of the  $N$ -electron system. As Equation (5.12) indicates we restrict ourselves to the excitations which conserve the total number of electrons. The most convenient approach to these excitations is given by a two-particle correlation function,  $L(12; 1'2')$  which is defined by [8]

$$L(12; 1'2') = -G_2(12; 1'2') + G_1(1, 1')G_1(2, 2') \quad (5.13)$$

$L$  describes the correlated propagation of two particles in addition to the individual propagation of each particle, which is contained in the product of two single-particle Green's functions in Equation (5.13).  $L$  obeys the Bethe-Salpeter equation [8]:

$$L(12; 1'2') = L_0(12; 1'2') + \int d(3456) L_0(14; 1'3) \Xi(35; 46) L(62; 52'). \quad (5.14)$$

$\Xi$  denotes the electron-hole interaction kernel (see Section 5.3),  $L_0(12; 1'2')$  corresponds to the non-interacting electron-hole pair propagator which is given by

$$L_0(12; 1'2') = G_1(1, 2')G_1(2, 1').$$

The notation (1) stands for a set of space, spin and time coordinates:  $(1) = (\mathbf{x}_1, t_1) = (\mathbf{r}_1, \sigma_1, t_1)$ .  $L$  depends on four time variables which correspond to two electron-hole creation processes and two electron-hole annihilation processes. In the context of optical

spectra we restrict ourselves to simultaneous creation and annihilation, so only two of four time variables are independent. Finally, only the difference of these two time variables is relevant for Equation (5.14) due to time homogeneity in the absence of external fields. This allows us to carry out a time-energy Fourier transform to  $L(\mathbf{x}_1, \mathbf{x}_2; \mathbf{x}'_1, \mathbf{x}'_2; \omega)$ .

Assuming that the one-electron Green's function  $G_1$  is fully given by the electron and hole long-lived quasiparticle states given by Equation (3.10),

$$G_1(\omega) = \sum_m \frac{|m\rangle\langle m|}{\omega - \epsilon_m \pm i0^+} \quad (5.15)$$

$L_0$  can be written as [8]

$$L_0(\mathbf{x}_1, \mathbf{x}_2; \mathbf{x}'_1, \mathbf{x}'_2; \omega) = i \sum_{\mathbf{k}, v, c} \left[ \frac{\psi_{\mathbf{k}+\mathbf{Q}c}(\mathbf{x}_1) \psi_{\mathbf{k}v}^*(\mathbf{x}'_1) \psi_{\mathbf{k}v}(\mathbf{x}_2) \psi_{\mathbf{k}+\mathbf{Q}c}^*(\mathbf{x}'_2)}{\omega - (E_{\mathbf{k}+\mathbf{Q}c} - E_{\mathbf{k}v}) + i0^+} - \frac{\psi_{\mathbf{k}v}(\mathbf{x}_1) \psi_{\mathbf{k}+\mathbf{Q}c}^*(\mathbf{x}'_1) \psi_{\mathbf{k}+\mathbf{Q}c}(\mathbf{x}_2) \psi_{\mathbf{k}v}^*(\mathbf{x}'_2)}{\omega + (E_{\mathbf{k}+\mathbf{Q}c} - E_{\mathbf{k}v}) + i0^+} \right]. \quad (5.16)$$

The sum over  $v$  includes occupied states and  $c$  runs over conduction states only,  $\mathbf{k}$  is the Bloch wave vector in the Brillouin zone and  $\mathbf{Q}$  is the total momentum of the electron-hole state. In an optical excitation process,  $\mathbf{Q}$  is the momentum of the photon absorbed by the two particle state. Its magnitude is usually small for the case of bulk solids in the visible region of the electro-magnetic spectrum. Thus, it is assumed zero in the present work. Energies,  $E_{\mathbf{k}m}$  and functions,  $\psi_{\mathbf{k}m}(\mathbf{x})$  refer to quasiparticle energies and wave functions respectively. In analogy to the quasiparticle approximation, we assume that the electron-hole excitations (excitons) are given by long-lived transitions thus the correlation function  $L$  can be written in a form similar to Equation (5.16):

$$L(\mathbf{x}_1, \mathbf{x}_2; \mathbf{x}'_1, \mathbf{x}'_2; \omega) = i \sum_S \left[ \frac{\chi_S(\mathbf{x}_1, \mathbf{x}'_1) \chi_S^*(\mathbf{x}'_2, \mathbf{x}_2)}{\omega - \Omega_S + i0^+} - \frac{\chi_S(\mathbf{x}_2, \mathbf{x}'_2) \chi_S^*(\mathbf{x}'_1, \mathbf{x}_1)}{\omega + \Omega_S + i0^+} \right], \quad (5.17)$$

where  $S$  denotes the correlated electron-hole excitation of the system, and  $\Omega_S$  is corresponds to the excitation energy. The electron-hole amplitude is defined by

$$\chi_S(\mathbf{x}, \mathbf{x}') = -\langle N, 0 | \hat{\psi}^\dagger(\mathbf{x}') \hat{\psi}(\mathbf{x}) | N, S \rangle. \quad (5.18)$$

The amplitude can be transformed into a basis of single-particle wave functions of the electron and hole states. In that basis it is expressed in the form:

$$\chi_S(\mathbf{x}, \mathbf{x}') = \sum_{\mathbf{k}} \sum_v^{\text{occ}} \sum_c^{\text{empty}} [A_{\mathbf{k}vc}^S \psi_{\mathbf{k}c}(\mathbf{x}) \psi_{\mathbf{k}v}^*(\mathbf{x}') + B_{\mathbf{k}vc}^S \psi_{\mathbf{k}v}(\mathbf{x}) \psi_{\mathbf{k}c}^*(\mathbf{x}')]. \quad (5.19)$$

The physical picture of an electron-hole pair suggests that only a limited number of electron-hole pairs will contribute to each excitation.

From Equations (5.16, 5.17) and (5.19) an integral Bethe-Salpeter equation (5.14) turns into a generalised eigenvalue problem given by the Hamiltonian [11],

$$\hat{H} = \begin{pmatrix} \hat{H}^{(v,c)(v',c')} & \hat{H}^{(v,c)(c',v')} \\ -\hat{H}^{*(v,c)(c',v')} & -\hat{H}^{*(v,c)(v',c')} \end{pmatrix}. \quad (5.20)$$

The Hamiltonian has a block-matrix structure and each block,  $\hat{H}^{(n_1, n_2)(n_3, n_4)}(\omega)$  is defined by

$$\begin{aligned} \hat{H}^{(n_1, n_2)(n_3, n_4)}(\omega) &= (E_{n_2} - E_{n_1})\delta_{n_1, n_3}\delta_{n_2, n_4} + i \text{sign}(E_{n_2} - E_{n_1}) \\ &\int d(3456)\psi_{n_1}(\mathbf{x}_4)\psi_{n_2}(\mathbf{x}_3)\Xi(\mathbf{x}_4, \mathbf{x}_3; \mathbf{x}_5, \mathbf{x}_6; \omega)\psi_{n_3}^*(\mathbf{x}_5)\psi_{n_4}^*(\mathbf{x}_6). \end{aligned} \quad (5.21)$$

As indicated in (5.20) a pair of bands  $(n_i, n_j)$  presents one occupied and one empty state, and one Bloch vector,  $\mathbf{k}$  from the Brillouin zone which is left out for clarity. The off-diagonal elements of (5.20) do not contain the quasiparticle transition energies, only the interaction elements. It has been shown [13] that these elements are small and they have little effect for the absorption spectrum, however they could influence some other optical properties such as the macroscopic dielectric constant [13]. Nevertheless, we neglect the off-diagonal blocks, and separate the Hamiltonian into two block-diagonal parts: the resonant contributions which correspond to positive frequencies and the anti-resonant ones, active for negative frequencies. In this work, we consider the resonant contribution only and the electron-hole Hamiltonian will refer to that block for the remainder of this work. The matrix of the resonant block is Hermitian and yields the set of equations [13]:

$$(E_{\mathbf{k}c} - E_{\mathbf{k}v})A_{\mathbf{k}vc}^S + \int d\mathbf{k}' \sum_{v'c'} \langle v\mathbf{k}\mathbf{k}' | \Xi | v'c'\mathbf{k}' \rangle A_{v'c'\mathbf{k}'}^S = \Omega_S A_{\mathbf{k}vc}^S. \quad (5.22)$$

This corresponds to expanding the excited states in electron-hole pair configurations as

$$|N, S\rangle = \sum_{\mathbf{k}} \sum_v^{occ} \sum_c^{empty} A_{\mathbf{k}vc}^S \hat{a}^\dagger \hat{b}^\dagger |N, 0\rangle =: \sum_{\mathbf{k}} \sum_v^{occ} \sum_c^{empty} A_{\mathbf{k}vc}^S |vc\rangle \quad (5.23)$$

where  $\hat{a}^\dagger$  and  $\hat{b}^\dagger$  create a quasi-hole or a quasi-electron, respectively, in the many-body ground state  $|N, 0\rangle$ .



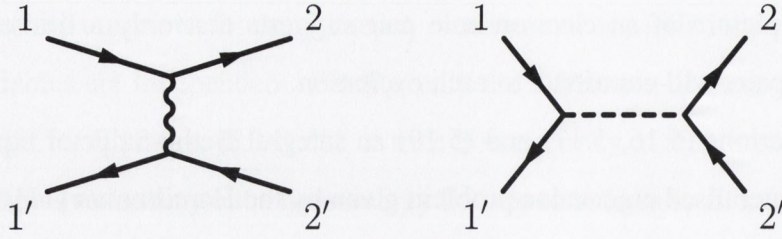


**Figure 5.1:** The irreducible electron-hole interaction  $\Xi$ : electron-hole attraction (left) and Coulomb repulsion (right)

### 5.3 The Electron-Hole Interaction Kernel

The electron-hole interaction kernel  $\Xi$  is given by the functional derivative [8]

$$\Xi(1\ 2; 1'\ 2') = \frac{\delta[V_{Coul}(1, 1')\delta(1, 1') + \Sigma(1, 1')]}{\delta G_1(2', 2)} \quad (5.24)$$

where  $V_{Coul}$  is the Coulomb potential and  $\Sigma$  is the self-energy operator. The self-energy operator is again treated within the  $GW$  approximation given by Equation (3.31). The first term in (5.24) is simple since  $V_{Coul} \hat{=} \rho v = \rho \times 1/|r - r'|$  depends linearly on the charge density  $\rho$ , which is given in terms of  $G_1$  by  $\rho(1) = -iG_1(1, 1^+)$ . The derivative of the self-energy leads to the two contributions:

$$\frac{\delta \Sigma}{\delta G_1} = W + G_1 \left( \frac{\delta W}{\delta G_1} \right) \quad (5.25)$$

The contribution  $\delta W/\delta G_1$  contains information about changes in screening due to the excitation and is assumed to be small [8]. In addition, this term is difficult to evaluate, computationally and mathematically. It was neglected in earlier calculations [8, 11, 13], and in this work as well. Thus, one obtains the following expression for  $\Xi$ :

$$\begin{aligned} \Xi(1\ 2; 1'\ 2') &= -i\delta(1, 1')\delta(2, 2')v(1, 2') + i\delta(1, 2')\delta(1', 2)W(1^+, 1') \\ &=: \Xi^x(1\ 2; 1'\ 2') + \Xi^d(1\ 2; 1'\ 2') \end{aligned} \quad (5.26)$$

Feynman diagrams for the interaction are presented in Figure 5.1. The interaction includes two terms: the screened electron-hole attraction, also called the direct interaction,  $\Xi^d$  (left panel of Figure 5.1) and the exchange interaction,  $\Xi^x$  which results from the un-

screened Coulomb bare repulsion (right panel). Higher order exchange diagrams [96] are allowed, however they will not be considered in this work.

Matrix elements of the interaction kernel are given by

$$\begin{aligned} \langle v\mathbf{c}\mathbf{k}|\Xi^d(\Omega_S)|v'\mathbf{c}'\mathbf{k}'\rangle = & \\ & - \int d\mathbf{x}d\mathbf{x}'\psi_{\mathbf{c}\mathbf{k}}^*(\mathbf{x})\psi_{v'\mathbf{k}'}(\mathbf{x})\psi_{v\mathbf{k}}(\mathbf{x}')\psi_{v'\mathbf{k}'}^*(\mathbf{x}')\frac{i}{2\pi}\int d\omega e^{i\omega 0^+}W(\mathbf{r},\mathbf{r}',\omega) \\ & \times \left[ \frac{1}{\Omega_S - \omega - (E_{\mathbf{c}'\mathbf{k}'} - E_{v'\mathbf{k}'}) + i0^+} - \frac{1}{\Omega_S + \omega - (E_{\mathbf{c}'\mathbf{k}'} - E_{v'\mathbf{k}'}) + i0^+} \right] \end{aligned} \quad (5.27)$$

and

$$\langle v\mathbf{c}\mathbf{k}|\Xi^x|v'\mathbf{c}'\mathbf{k}'\rangle = \int d\mathbf{x}d\mathbf{x}'\psi_{\mathbf{c}\mathbf{k}}^*(\mathbf{x})\psi_{v\mathbf{k}}(\mathbf{x})v(\mathbf{r},\mathbf{r}')\psi_{v'\mathbf{k}'}(\mathbf{x}')\psi_{v'\mathbf{k}'}^*(\mathbf{x}'). \quad (5.28)$$

Their calculation requires evaluation of six-dimensional real-space integrals involving the quasiparticle wave functions. In addition, the direct interaction term  $\Xi^d$  requires a frequency integration. Although, this integration is possible to carry out within a plasmon-pole model, we restrict ourselves to static screening only. The dynamical properties of  $W(\omega)$  are relevant if the excitonic binding energies are of the same order of magnitude as the characteristic oscillation frequencies in  $W(\omega)$ . This effect is pronounced in molecules or atoms [13]. However, dynamical effects in the electron-hole screening and in the one particle Green's function tend to cancel each other [11] for periodic crystals and particularly semiconductors, which suggests that both of them can be neglected. In that case the direct interaction has a simple expression

$$\langle v\mathbf{c}\mathbf{k}|\Xi^d|v'\mathbf{c}'\mathbf{k}'\rangle = - \int d\mathbf{x}d\mathbf{x}'\psi_{\mathbf{c}\mathbf{k}}^*(\mathbf{x})\psi_{v'\mathbf{k}'}(\mathbf{x})W(\mathbf{r},\mathbf{r}',\omega = 0)\psi_{v\mathbf{k}}(\mathbf{x}')\psi_{v'\mathbf{k}'}^*(\mathbf{x}') \quad (5.29)$$

which is used in this work.

## 5.4 The Spin Structure of the Excitons

The spin structure of solutions of the Bethe-Salpeter equation is an important issue. Two different situations can occur depending on the strength of the spin-orbit interaction compared to the electron-hole interaction in the system.

Firstly, if the ground state is a spin-singlet configuration, and if the spin-orbit interaction is negligible, the single-particle states,  $|n\rangle$  are classified as a spin-up,  $|n_+\rangle$  and spin-down,  $|n_-\rangle$  states<sup>2</sup>. Then the Hilbert space of the electron-hole pairs,  $|vc\rangle$  consists of four subspaces:

$$|vc\rangle \longrightarrow (|v_+c_+\rangle, |v_+c_-\rangle, |v_-c_+\rangle, |v_-c_-\rangle)$$

In this representation, the electron-hole Hamiltonian (5.20) obtains the form

$$\hat{H}^{(vc)(v'c')} = \begin{pmatrix} D + \Xi^d + \Xi^x & 0 & 0 & \Xi^x \\ 0 & D + \Xi^d & 0 & 0 \\ 0 & 0 & D + \Xi^d & 0 \\ \Xi^x & 0 & 0 & D + \Xi^d + \Xi^x \end{pmatrix} \begin{pmatrix} (\leftrightarrow |v_+c_+\rangle) \\ (\leftrightarrow |v_+c_-\rangle) \\ (\leftrightarrow |v_-c_+\rangle) \\ (\leftrightarrow |v_-c_-\rangle) \end{pmatrix} \quad (5.30)$$

where  $D = E_{ck} - E_{vk}$ . This Hamiltonian decouples into a spin-singlet,  $j = 1/2$  class of solutions given by

$$\frac{1}{\sqrt{2}}(|v_+c_+\rangle - |v_-c_-\rangle)$$

and spin-triplet,  $j = 3/2$  class<sup>3</sup> consisting of the subspaces

$$|v_+c_-\rangle, |v_-c_+\rangle, \text{ and } \frac{1}{\sqrt{2}}(|v_+c_+\rangle + |v_-c_-\rangle)$$

The Hamiltonian becomes  $D + \Xi^d + 2\Xi^x$  for the spin-singlet class and it is given by  $D + \Xi^d$  for the spin-triplet class. Thus, the Bethe-Salpeter equation can be solved for the spin-singlet and spin-triplet configurations separately and the spin degrees of freedom have been eliminated from the remaining problem.

The second case occurs when the spin-orbit interaction is of the same order of magnitude as (or larger than) the electron-hole interaction. In that case, the single-particle states cannot longer be classified as a spin-up and spin-down states and there is no distinction between singlet and triplet states any more [13]. So, the Bethe-Salpeter Hamiltonian must be discussed including its full spin structure. Since this increases the number of basis states by a factor of 4, the evaluation of the Bethe-Salpeter equation becomes more

<sup>2</sup>Spin of the hole states  $|v\rangle$  corresponds to the electron which originally occupied the state. The spin of the hole would be the negative.

<sup>3</sup>It is convention to call  $j = 1/2$  class and  $j = 3/2$  spin-singlet and spin-triplet exciton states, respectively. In here,  $j$  denotes momentum of the hole. The total momentum of an exciton state is  $J = 0$  for the spin-singlet and  $J = 1$  for spin-triplet states.

difficult. For this reason the spin-orbit interaction is not taken into account in the present work. In addition, the full spin structure should be included in the Hamiltonian for open-shell systems that do not have a spin-singlet ground state.

## 5.5 Optical Spectra

In Section 5.1 we have been presented macroscopic dielectric function in its long-wavelength limit as:

$$\varepsilon_M(\omega) = 1 - \lim_{\mathbf{q} \rightarrow 0} \frac{4\pi}{\Omega q^2} P(\mathbf{q}, \omega). \quad (5.31)$$

In this limit it describes collective excitations, absorption and refraction of the light. Its real part in the static limit,  $\varepsilon_1(\omega = 0)$  is the dielectric constant,  $\varepsilon_0$  and describes the static screening of the Coulomb interaction in the many-body system, while the imaginary part  $\varepsilon_2(\omega)$  is directly related to the measured absorption spectrum. In Sections 5.2-5.4 we presented a way of calculating the two-particle correlation function which defines polarisability beyond the RPA. From Equations (5.17), (5.23) and (5.31) we can write down a final expression for  $\varepsilon_M(\omega)$  [11]

$$\varepsilon_M(\omega) = 1 + \lim_{\mathbf{q} \rightarrow 0} \frac{8\pi e^2}{\Omega q^2} \sum_S \frac{|\sum_{v,c,\mathbf{k}} \langle v\mathbf{k} | e^{-i\mathbf{q}\cdot\mathbf{r}} | c\mathbf{k} \rangle A_{\mathbf{k}vc}^S|^2}{\Omega_S - \omega - i0^+}, \quad (5.32)$$

which, now includes electron-hole excitations.

The main effect of the electron-hole interaction is the coupling of different electron-hole configurations  $|v\mathbf{c}\mathbf{k}\rangle$  in the excitations  $|S\rangle$ . In Equation (5.32), optical transitions are given as a coherent sum of the transition matrix elements of the contributing electron-hole pair configurations, including the coupling coefficients  $A_{\mathbf{k}vc}^S$ . Without the electron-hole interaction, excitations are given by vertical transitions between independent electron and hole states. In that limit Equation (5.32) reduces to the well known RPA dielectric function which we presented in Section 5.1.

$$\varepsilon_M^{RPA}(\omega) = 1 + 2 \lim_{\mathbf{q} \rightarrow 0} \frac{8\pi e^2}{\Omega q^2} \sum_{v,c,\mathbf{k}} \frac{|\langle v\mathbf{k} | e^{-i\mathbf{q}\cdot\mathbf{r}} | c\mathbf{k} \rangle|^2}{E_{c\mathbf{k}} - E_{v\mathbf{k}} - \omega - i0^+}. \quad (5.33)$$

The factor of 2 arises from explicit integration over the spin variable.

The RPA approximation of the dielectric function could be sufficient to describe optical properties for the homogeneous electron gas. In Section 5.1 it has been shown how to introduce local field effects into calculations by means of calculating the entire dielectric matrix  $\varepsilon_{\mathbf{G}\mathbf{G}'}$  and inverting it, see Equations (5.8,5.9). However, in the present interacting-particle approach such a procedure is unnecessary. It has been shown by Del Sole *et al.* [97] that local field effects are already included due to the exchange interaction,  $\Xi^x$  in the electron-hole interacting kernel. So, all information that we need is contained in Equation (5.32).

Relations (5.32) and (5.33) contain a divergent factor  $1/q^2$  which comes from the Fourier transform of the Coulomb potential. This problem can be solved using well known "k · p" theory. It is based on the equation of continuity or on the resulting equality between density and current response. This condition is expressed in the equation [96]

$$\langle v\mathbf{k}|e^{-i\mathbf{q}\cdot\mathbf{r}}|c\mathbf{k} + \mathbf{q}\rangle = \frac{\langle v\mathbf{k}|\mathbf{q} \cdot \hat{\mathbf{j}}(\mathbf{q})|c\mathbf{k} + \mathbf{q}\rangle}{E_{c\mathbf{k}+\mathbf{q}} - E_{v\mathbf{k}}} \quad (5.34)$$

where  $\hat{\mathbf{j}}(\mathbf{q})$  denotes the current operator and it is given by  $\hat{\mathbf{j}}(\mathbf{q}) = i[\hat{H}_0, e^{i\mathbf{q}\cdot\mathbf{r}}]$ , which in the  $\mathbf{q} \rightarrow 0$  limit reduces to  $\hat{\mathbf{j}}(\mathbf{q}) = i[\hat{H}_0, \mathbf{r}]$ . If the crystal potential is a local operator, i.e. if the potential commutes with the position operator  $[V(\mathbf{r}), \mathbf{r}] = 0$ , then the current operator can simply be replaced by the momentum operator  $\hat{\mathbf{p}}$ . However, this no longer holds in the case of the quasiparticle Hamiltonian (3.12) due to self-energy operator nonlocality and the commutator,  $[V(\mathbf{r}), \mathbf{r}]$  has to be accounted for. Even if the quasiparticle shifts are the same for all empty states, the self-energy operator is non-local due to the different spatial properties of the wave functions at the different wave vectors. As discussed by Levine and Allan [98], the quasiparticle shift between the LDA and quasiparticle transition energy of an electron-hole pair  $|v\mathbf{c}\mathbf{k}\rangle$  leads to a renormalisation of the optical transition matrix element:

$$\langle v\mathbf{k}|\hat{\mathbf{j}}|c\mathbf{k}\rangle^{QP} := \frac{E_{c\mathbf{k}}^{QP} - E_{v\mathbf{k}}^{QP}}{E_{c\mathbf{k}}^{LDA} - E_{v\mathbf{k}}^{LDA}} \langle v\mathbf{k}|\hat{\mathbf{p}}|c\mathbf{k}\rangle^{LDA}. \quad (5.35)$$

Alternatively, in the crystalline case, the optical transition matrix element can be calculated from the relation [99]

$$\langle v\mathbf{k}|\hat{\mathbf{j}}|c\mathbf{k}\rangle_{\alpha}^{QP} = \frac{E_{c\mathbf{k}}^{QP} - E_{v\mathbf{k}}^{QP}}{q} \langle v\mathbf{k}|e^{-i\mathbf{q}\cdot\mathbf{r}}|c\mathbf{k} + q\mathbf{e}_{\alpha}\rangle \quad (5.36)$$

with  $q$  being a small but finite shift of  $\mathbf{k}$  in reciprocal space. To this end, the wave functions at the shifted wave vectors  $\mathbf{k} + q\mathbf{e}_\alpha$  ( $\alpha = x, y, z$ ) have to be calculated explicitly. In this relation not only is quasiparticle renormalisation accounted for, but also the non-local part of the pseudopotential or Hartree-Fock exchange, if one is used in the calculation [99].

## 5.6 Numerical Details

The Bethe-Salpeter equation for a periodic system is given as an eigenvalue problem of infinite dimensionality, (5.22)

$$(E_{\mathbf{k}c} - E_{\mathbf{k}v})A_{\mathbf{k}vc}^S + \int_{V_{BZ}} d\mathbf{k}' \sum_{v'c'} \langle vck | \Xi | v'c'\mathbf{k}' \rangle A_{v'c'\mathbf{k}'}^S = \Omega_S A_{\mathbf{k}vc}^S. \quad (5.37)$$

The integration ranges over the full Brillouin zone of volume  $V_{BZ}$ . For the numerical evaluation the continuous integration with respect to  $\mathbf{k}'$  has to be replaced by some discrete scheme of finite dimensionality. The easiest approach is to divide the BZ into an appropriate grid (uniform or nonuniform) of sub-volumes  $V_i$ , represented by one  $\mathbf{k}_i$  point inside it [13]. Then we assume that the coefficients  $A_{\mathbf{k}vc}^S$ , and the quasiparticle energy difference,  $(E_{\mathbf{k}c} - E_{\mathbf{k}v})$  are averaged by values taken at the points  $\mathbf{k}_i$ . In the case of equal sub-volumes  $V_i \equiv V$ , the BSE yields

$$(E_{\mathbf{k}_i c} - E_{\mathbf{k}_i v})A_{\mathbf{k}_i vc}^S + \sum_{\mathbf{k}'_i} \sum_{v'c'} \frac{1}{V} \int_{V_i} d\mathbf{k} \int_{V_i} d\mathbf{k}' \langle vck_i | \Xi | v'c'\mathbf{k}'_i \rangle A_{v'c'\mathbf{k}'_i}^S = \Omega_S A_{\mathbf{k}_i vc}^S. \quad (5.38)$$

In the current work  $\mathbf{k}$  points are chosen from a Monkhorst-Pack mesh [60].

Electron-hole interaction matrix elements have to be evaluated in an appropriate basis. We use a plane-wave basis for all two-point functions, as stated in Section 3.4. In this basis, the screened potential is given by Equation (3.29), thus matrix elements of the direct term of the electron-hole interaction, given by (5.29) yields

$$\begin{aligned} \langle vck | \Xi^d | v'c'\mathbf{k}' \rangle &= -\frac{4\pi e^2}{\Omega} \sum_{\mathbf{G}, \mathbf{G}'} \frac{\varepsilon^{-1}(\mathbf{q}, \omega = 0)}{|\mathbf{q} + \mathbf{G}| |\mathbf{q} + \mathbf{G}'|} \\ &\times \langle v'\mathbf{k}' | e^{i(\mathbf{q} + \mathbf{G}) \cdot \mathbf{r}} | v\mathbf{k} \rangle \langle c\mathbf{k} | e^{-i(\mathbf{q} + \mathbf{G}') \cdot \mathbf{r}} | c'\mathbf{k}' \rangle \delta_{\mathbf{q}, \mathbf{k}' - \mathbf{k}}. \end{aligned} \quad (5.39)$$

Special care has to be taken for the case  $\mathbf{q} \rightarrow 0$  ( $\mathbf{k} = \mathbf{k}'$ ). If  $\mathbf{G} = \mathbf{G}' = 0$  the interaction diverges as  $1/q^2$ . This contribution is separated in 5.38 and integrated over a small sphere

of volume  $V = V_{BZ}/N_k$ , where  $N_k$  is the total number of  $\mathbf{k}$  points. This divergence contributes only notably when  $v = v'$  and  $c = c'$  [100]. In addition the divergence of  $1/q$  type occurs when one of the  $\mathbf{G}$ -vectors is zero ( $\mathbf{G} \neq \mathbf{G}' = 0$  or  $\mathbf{G}' \neq \mathbf{G} = 0$ ). These terms are neglected, because their contribution either averages to zero or vanishes quickly in the limit of a large number of  $\mathbf{k}$  points [100]. For the finite  $\mathbf{q}$  case (i.e.  $\mathbf{k} \neq \mathbf{k}'$ ) the interaction kernel is averaged by the value taken at  $\mathbf{k}_i$  and  $\mathbf{k}'_i$  which leads to

$$\begin{aligned} (E_{\mathbf{k}_i c} - E_{\mathbf{k}_i v})A_{\mathbf{k}_i v c}^S + \frac{1}{V} \sum_{v' c'} \int_V d\mathbf{q} \langle v c \mathbf{k}_i | \Xi | v' c' \mathbf{k}_i \rangle A_{\mathbf{k}_i v c}^S \\ + \sum_{\mathbf{k}'_i \neq \mathbf{k}_i} \sum_{v' c'} \langle v c \mathbf{k}_i | \Xi | v' c' \mathbf{k}'_i \rangle A_{v' c' \mathbf{k}'_i}^S = \Omega_S A_{\mathbf{k}_i v c}^S. \end{aligned} \quad (5.40)$$

The exchange term of the interaction (5.28) in the plane-wave basis obeys

$$\langle v c \mathbf{k} | \Xi^x | v' c' \mathbf{k}' \rangle = 2 \times \frac{4\pi e^2}{\Omega} \sum_{\mathbf{G} \neq 0} \frac{1}{G^2} \langle c \mathbf{k} | e^{i\mathbf{G} \cdot \mathbf{r}} | v \mathbf{k} \rangle \langle v' \mathbf{k}' | e^{-i\mathbf{G} \cdot \mathbf{r}} | c' \mathbf{k}' \rangle. \quad (5.41)$$

The summation over the reciprocal lattice vectors is restricted to non-zero  $\mathbf{G}$  because the Coulomb interaction must be used without the long-range term of vanishing wave vector to obtain the macroscopic dielectric function [9]. Finally, this term does not suffer from any divergence.

In order to calculate the screened interaction (5.39) the inverse static dielectric matrix,  $\varepsilon_{\mathbf{G}\mathbf{G}'}^{-1}(\mathbf{q}, \omega = 0)$  has to be computed at each  $\mathbf{q}$ . We calculate the full RPA symmetric dielectric matrix given by Equation (5.8) at all stars of  $\mathbf{q}$  in the IBZ, numerically invert them and generate the inverted dielectric matrix for the remaining  $\mathbf{q}$  points by symmetry.

## Chapter 6

# Calculation of the Optical Properties in Bulk Materials

The main focus of this chapter, and final goal of this thesis is studying optical properties for different materials, accurately. Initially, the macroscopic dielectric function was calculated using the RPA approach, with and without local field effects. The energy loss function within the RPA approximation is illustrated as well. It is known that the RPA approach cannot result in reliable low-energy optical spectra for semiconductors or insulators, however with local field effects included, it can give some main features of the energy loss function.

Inclusion of excitonic effects can be crucial in an optical spectrum calculation for semiconductors and particularly, insulators. The excitonic effects and electron-hole bound states were studied by calculating the electron-hole interaction (5.39) and (5.41) and solving the Bethe-Salpeter Equation (5.38), then accurate optical spectra and dielectric constant were calculated from Equation (5.32).

Firstly, we applied our approach to bulk silicon. This gave us an opportunity to compare our data with accurate experimental measurements as well as with some earlier calculations. Then the approach was applied to the rare gas solids (RGS): Ne, Ar, Kr and Xe, because of their strong electron-hole interaction and interesting excitonic properties.

This chapter is organised as follows: Section 6.1 gives convergence details for the RPA and exciton calculations. Optical spectra within the RPA approach for Si and RGS are presented in Section 6.2. Sections 6.3 and 6.4 contain calculations of the optical spec-



tra for Si and RGS, respectively, with the electron-hole interaction included. In addition, bound exciton states and electron-hole wave functions for the RGS are discussed in Section 6.4 and 6.5, respectively. The static dielectric constant is presented in Section 6.6 for Si and the RGS. Energy loss functions within the RPA for Ne, Ar and Kr are presented in Section 6.7.

## 6.1 Convergence Parameters

### 6.1.1 RPA calculation

Calculations within the RPA approach were carried out using either  $GW$  quasiparticle energies (in Section 6.2) or DFT-LDA eigenvalues (Section 6.7). DFT-LDA and  $GW$  calculations have been discussed in Sections 4.1.1 and 4.1.2, respectively. Optical spectra were calculated using both interband transitions [Equation (5.33)] and local field effects [Equation (5.9)]. Local field effects were included by numerically inverting the full RPA dielectric matrix,  $\varepsilon_{\mathbf{G}\mathbf{G}'}(\mathbf{q} \rightarrow 0, \omega)$  given by Equation (5.8). The special case for the  $\mathbf{q} \rightarrow 0$  limit when  $\mathbf{G} = \mathbf{G}' = 0$  or  $\mathbf{G} \neq \mathbf{G}' = 0$  is treated analytically using ' $\mathbf{k} \cdot \mathbf{p}$ ' theory, as described in Section 5.5.

We found that a dielectric matrix size of  $59 \times 59$  all materials studied was sufficient to produce well converged results for the inverted dielectric matrix, the relative error of the inverse elements being less than 1% when compared to the spectrum obtained with a matrix size of  $65 \times 65$ . In interband transitions, 4 valence and 45 conduction bands were employed for Si and 3 valence and 30 conduction bands for RGS (see Appendix C). Monkroost-Pack special points were employed when performing summations over the Brillouin zone in Equations (5.33) and (5.8). 2048 special points in the full Brillouin zone were used for all materials studied here. More details and illustrations on RPA dielectric matrix convergence can be found in Appendix B.

### 6.1.2 Exciton calculation

When computing an optical spectrum with electron-hole excitations included [Equation (5.32)], 4 valence and 3 conduction bands and 864 special  $\mathbf{k}$  points in the full Brillouin zone were used.

loun zone were used for Silicon, 3 valence and 1 conduction band and 2049  $\mathbf{k}$  points for RGS. These sets of parameters define a maximum size ( $N_v \times N_c \times N_{\mathbf{k}}$ ) of an electron-hole Hamiltonian that can be diagonalised on a sequential computer with 2 GBytes of RAM. They usually produce converged optical spectra in the low energy region, however special points can result in limited resolution, thus some results may not be fully converged. Advantage could be taken by using off-symmetry shifted points, since the shifted set contains less degeneracy, and thus yields a better resolution, as stated elsewhere [12]. Nevertheless we used the special points as they are directly provided from the CRYSTAL95/98 calculation. The CRYSTAL code has limited size of shrinking factor (see Appendix A) and use of shifted points would require interpolation of the eigenvalues and eigenvectors at points which are not on the standard grid. For the first implementation of the BSE code it is simpler to use the special points.

Calculation of the electron-hole interaction (5.39, 5.41) and solution of the Bethe-Salpeter equation (5.38) requires large numerical effort, since the basis set for the electron-hole wave functions contains a large number of functions ( $N_v \times N_c \times N_{\mathbf{k}}$ ). For the sets of parameters specified above, there are up to  $10^8$  elements to compute. Fortunately, this number can be reduced by half when using hermiticity of the Hamiltonian. The number of calculated matrix elements can be further reduced by employing crystal symmetry. However, it is assumed in the general case, that the  $\mathbf{k}$  ( $\mathbf{k}'$ ) points are not high-symmetry points, but shifted points, thus the use of symmetry would not yield shorter computation times in this case. Instead, we focus on creating the most efficient algorithm for calculation of interaction matrix elements without employing symmetry. This approach provides an equally efficient calculation by using either set of points.

In computing matrix elements of the screened interaction (5.39), the RPA dielectric matrix has to be computed at each  $\mathbf{q} = \mathbf{k}' - \mathbf{k}$ . This is done using the same convergence parameters as in the self-energy calculation (see Section 4.1.2). Even if  $\mathbf{k}$  ( $\mathbf{k}'$ ) points were not high symmetry points, their difference,  $\mathbf{q}$  lies on a symmetric grid and the  $\mathbf{q}$ -point symmetry has been fully exploited in the RPA dielectric matrix calculation and this significantly reduced computational time.

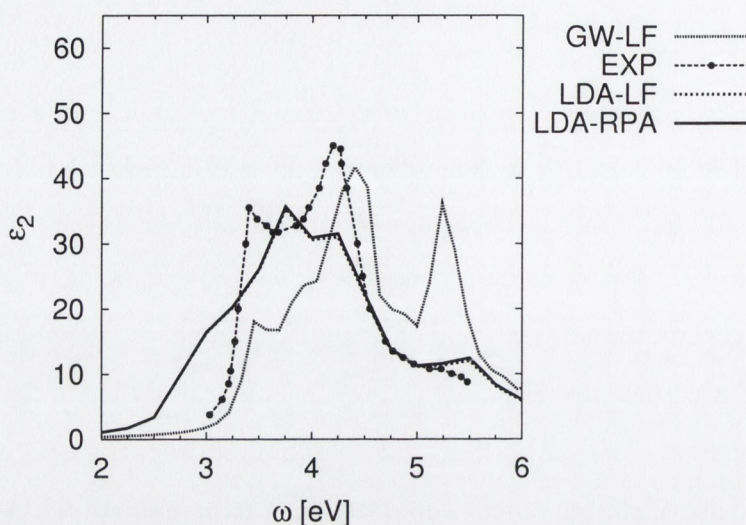


**Figure 6.1:** Imaginary part of the dielectric function,  $\epsilon_2$  for Si. The circles with dashed curve present experimental (EXP) data taken from [101]. The solid and short-dashed curves correspond to the calculated data using the LDA eigenenergies without (LDA-RPA) and with (LDA-LF) local field effects included, respectively. The dotted line corresponds to the calculated spectrum using the *GW* quasiparticle energies. This calculation was obtained by solving the Bethe-Salpeter equation (5.40), when only the exchange interaction (5.41) was included. An artificial broadening of 0.15 eV was used.

Matrix elements of the bare Coulomb interaction (5.41) require a large number of  $\mathbf{G}$  vectors for convergence, so up to 400  $\mathbf{G}$  vectors were used in calculating this term for all materials considered here. However, calculation of this term is not time consuming since the Fourier coefficients of the Coulomb potential are diagonal in reciprocal space in the present plane wave basis.

## 6.2 Calculated Optical Spectra and Local Field Effects

Figure 6.1 shows the imaginary part of the dielectric function as a function of photon energy for Si. Solid and dashed curves present RPA calculation without (5.33) and with (5.9) local field effects, respectively, using DFT-LDA eigenenergies. Experimental data is given by circles and taken from [101]. The first peak called  $E_1$ , which appears at 3.4 eV in the experimental spectrum, is visible only as a small shoulder in the calculated

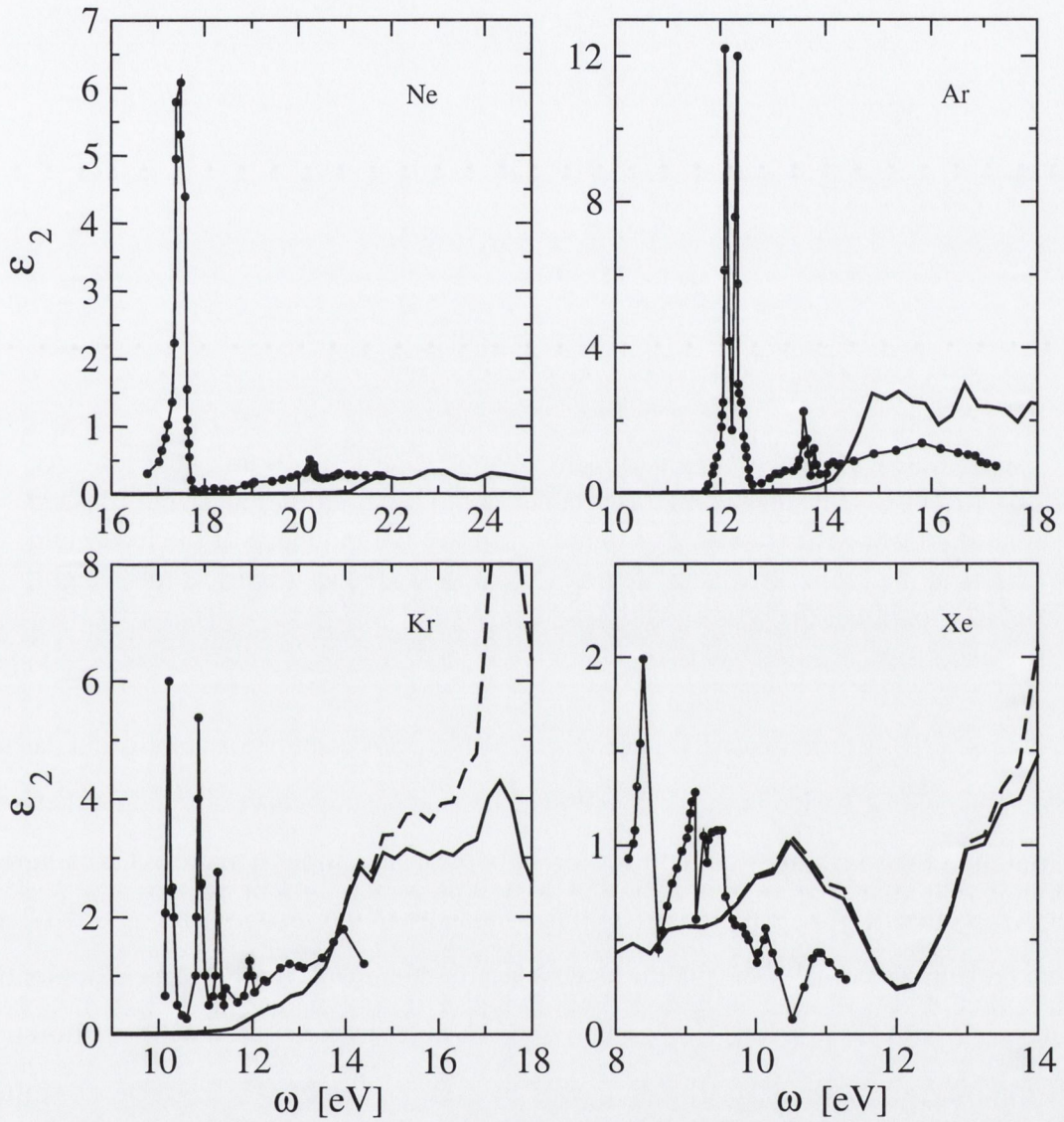


**Figure 6.2:** Imaginary part of the dielectric function as a function of photon energy for the rare gas solids: Ne, Ar, Kr and Xe. The figure shows comparison between experimental data (symbols with solid curve) and calculated spectra within the RPA using  $GW$  quasiparticle energies without (dashed curve) and with (solid curve) local field effects. The experimental data is taken from [77]. An artificial broadening of 0.15 eV was used.

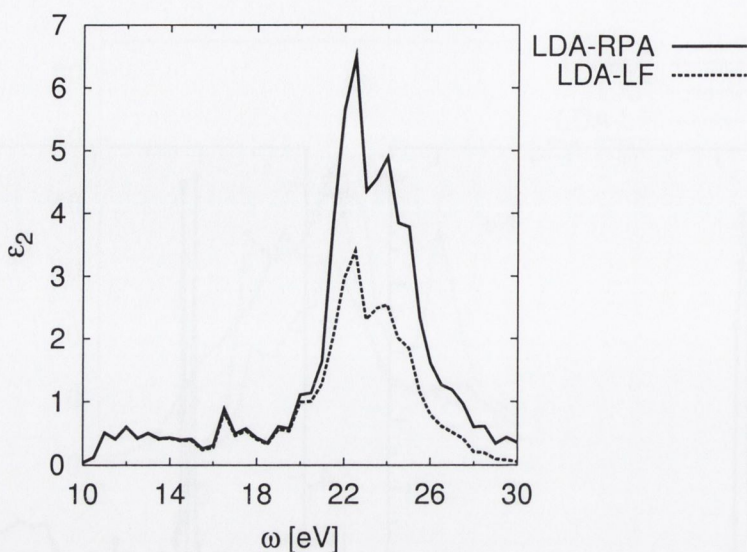


**Figure 6.3:** Calculated imaginary part of the dielectric function,  $\epsilon_2$  for solid Ar, using LDA eigenvalues and eigenvectors, without (solid line) and with (dashed line) the local field effects. The figure illustrates the influence of the local field effects at the higher frequency region. Local fields reduced the spectral weight, but did not affect the peaks positions.

RPA spectra. Its position is at about 3 eV in our LDA-RPA calculations (solid and dashed curves) and about 3.8 eV in the *GW*-RPA calculation (dotted curve). Local field effects did not affect the low energy spectrum for Si in our calculation. This result is in agreement with other RPA calculations [100]. The intensity of the second peak,  $E_2$ , at 4.2 eV is underestimated in RPA calculations, which is in agreement with the pseudopotential plane-wave RPA calculations by Onida *et al.* [11], however not with the all-electron calculation by Arnaud *et al.* [100]. Moreover, the introduction of *GW* corrections shifted peak positions toward higher energies and agreement with measured data was worsened at the region between 4 and 6 eV. It is clear that already in a conventional semiconductor such as silicon calculated peak positions can deviate from the measured values by several tenths of an eV. Also, the magnitude of the spectrum is either underestimated or overestimated when compared with the experimental data.

This discrepancy is even larger for wide gap semiconductors and insulators. Figure 6.2 shows  $\epsilon_2(\omega)$  for the rare gas solids: Ne, Ar, Kr and Xe. The symbols with solid lines present experimental data taken from [77]. The solid and dashed lines correspond

to calculated spectra within the RPA with (5.9) and without the local field effects (5.33), respectively.  $GW$  corrections were taken into account in these calculations. An artificial broadening of 0.15 eV was introduced for all solids. The figure illustrates that local field effects reduced the magnitude of the spectrum in the higher energy region (see Figure 6.2 for Kr and Xe), however peak positions were not changed by local field effects. On the other hand, local field effects did not influence the spectra in the low-energy region, so the structure in that region observed experimentally, is not described within RPA either with or without local field effects. Moreover, the main oscillator strength is shifted toward the higher energies yielding strong disagreement with the measured spectra. Illustration of that effect is given in Figure 6.3 where the RPA  $\epsilon_2$  is presented for solid Ar as a function of photon energy for the energy range up to 30 eV. LDA eigenenergies were employed in these calculations since our  $GW$  approximation does not describe states at the higher energy region (far from the gap) very well, (see Chapter 4). On the other hand, scattering of an electron in higher energy states by atomic potentials is small and the electronic structure of these states can probably be described by an almost free-electron theory. For this reason it is very likely that higher states can be described better by a DFT-LDA Hamiltonian rather than  $GW$  correction. The figure illustrates that local field effects do not change peak positions, but magnitudes of spectra. For the higher energy region this effect can improve agreement with experimental data.

### 6.3 Optical Spectrum for Si

In this section we present the optical spectrum for Si with included the electron-hole interaction (Figure 6.4, solid line). Figure 6.4 compares the calculated spectrum with the experimental (circles with dashed line) one and one with  $GW$  corrections and local field effects included. The spectrum which includes the interaction is in much better agreement with experimental data than the interband transition ( $GW$ -LF) calculation. The most important, difference is that the oscillator strength is shifted toward lower energies. This change originates from the coherent coupling of the optical transition matrix elements in the excited-state electron-hole wave function, which leads to a constructive

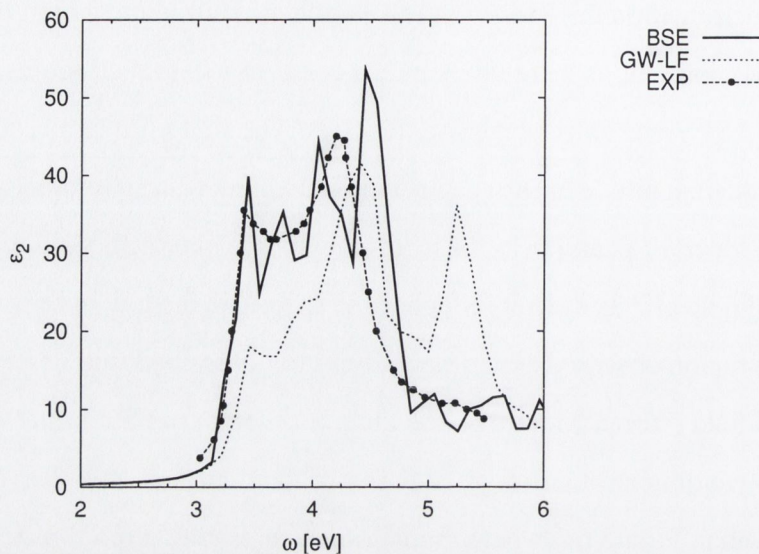


**Figure 6.4:** Imaginary part of the dielectric function,  $\epsilon_2$  for Si. The circles with dashed curve present experimental (EXP) data taken from [101]. The solid line corresponds to the calculation with excitonic effects included and the dotted line corresponds to the RPA calculated spectrum using the  $GW$  quasiparticle energies. An artificial broadening of 0.05 eV was used in the excitonic calculation.

superposition of the oscillator strengths for transitions at lower energies and to a destructive superposition at higher energies [11].

The position and intensity of the first peak,  $E_1$  agree well with experiment. However, the position of the second peak,  $E_2$  occurs at 4.5 eV while the experimental value is at 4.2 eV. This difference is due to the limited number of  $\mathbf{k}$  points; as reported in Section 6.1 we used only 864 special  $\mathbf{k}$  points. Due to the large dispersion of bands and high localisation of excitons at the zone boundary, optical spectra calculations require large number of  $\mathbf{k}$  points in Si. In a converged calculation by Onida *et. al* [11], 2048 special points were used and in Ref. [13, 100] up 500 shifted points were used to obtain a converged calculation in semiconductors. Slight overestimation in the intensities of the peaks and oscillations in the spectrum between 3.2 and 4.5 eV are due to limited number of  $\mathbf{k}$  points. Although, a similar structure was reported in Ref. [11], use of a root sampling technique in BZ integration [Equation (5.32)] gave a rise to the oscillations. Smooth spectra can be obtained by using more accurate integration method such as that

of by Gilat and Raubenheimer [102].

In conclusion, we have shown how inclusion of excitonic effects in the optical spectra calculation improves agreement with experimental data. The calculated Si spectrum is not fully converged, however it agrees qualitatively with experiment and earlier calculations [11]. Using a large number of special points (2048 or more) or shifted points and use of more accurate integration methods such as Gilat-Raubenheimer [102] would be desirable for more accurate description of optical spectra in semiconductors.

## 6.4 Macroscopic Dielectric Function and Exciton Effects of RGS

Electronic and excitonic properties of the RGS have been under investigation both theoretically and experimentally for about four decades. A collection of absorption data (imaginary part of the dielectric function) obtained experimentally has been presented already in Figure 6.2. The same figure shows our interband calculations and huge discrepancies between the calculated and measured data. The reason for that is neglecting the electron-hole interaction in the calculated data.

The sharp absorption lines observed experimentally are assigned to the two spin-orbit split exciton series [77, 75]. The excitons of the RGS consist of a hole in a  $p$ -type valence band and an electron in a  $s$ -type conduction band. The momentum of the hole can be either  $j = 3/2$  – exciton quantum number  $n$  (triplet) or  $j = 1/2$  – exciton quantum number  $n'$  (singlet). Apart from the  $n = 1$  and  $n' = 1$  exciton energies,  $E_n$  of the experimental spectrum can be described successfully by the Wannier-type formula given by

$$E_n = E_{gap} - \frac{B_{ex}}{n^2} \quad n = 2, 3 \dots, \quad (6.1)$$

where  $B_{ex}$  is the binding energy of the exciton states, and  $E_{gap}$  is energy difference between last occupied and first conduction band at  $\Gamma$  point. The energies of the first exciton states ( $n = 1$  and  $n' = 1$ ) deviate significantly from the Wannier values and it was believed that these excitons were more Frenkel-type excitons [103, 104]. This demonstrates that low-lying excitations of the RGS are examples of intermediately bound excitations



where neither the Frenkel nor the Wannier-type<sup>1</sup> of exciton is fully applicable. Several authors [105, 106, 107] tried to evaluate the energy shift of the first exciton state, separately, continuing to describe the higher states within Wannier approach. However, from the theoretical point of view, this is by no means satisfactory [108]. It can be expected that the short-range corrections of the electron-hole potential required to describe the  $n = 1$  and  $n' = 1$  state will affect the states  $n \geq 2$  too.

Our state-of-the-art, *ab initio* approach described in Chapter 5 allows us to describe the entire optical spectrum accurately. Also it presents a unified approach for studying bounded exciton states below the gap as well as unbounded electron-hole states, without using any free parameter. As described earlier, the approach consists of calculation of the electron-hole interaction (5.39, 5.41), solving the Bethe-Salpeter equation (5.38) for coupled electron-hole pair excitations and evaluating the coupled optical transition matrix elements in (5.32).

### 6.4.1 Neon

Neon is a wide-gap insulator and is characterised by weak dielectric screening and concomitantly strong excitonic effects. Its calculated macroscopic dielectric function, with excitonic effects included, is presented in Figure 6.5. The left panel shows the real part,  $\varepsilon_1$  and the imaginary part,  $\varepsilon_2$  is on the right panel. Experimental data is given by circles joined by a dashed line as a guide for the eye. It was obtained by Skibowski cited in [77] by means of the Kramers-Kronig relation from reflection measurements. Numerical details of the calculation are given in Section 6.1. The chosen set of parameters yields a spectral resolution of several meV for the energy range from 20 to 22 eV and about 0.05 eV for energies below 20 eV. An artificial broadening of 0.05 eV was introduced in the calculated spectra.

The spectrum is completely changed at all energies when the electron-hole interaction was included. The most important, the sharp peaks in the low-energy region, observed

---

<sup>1</sup>The Frenkel model assumes that an exciton is highly localised on the atom site or at bond between atoms, and the Wannier model describes excitons delocalised in a real space and highly localised in a reciprocal space usually at the zone boundary.

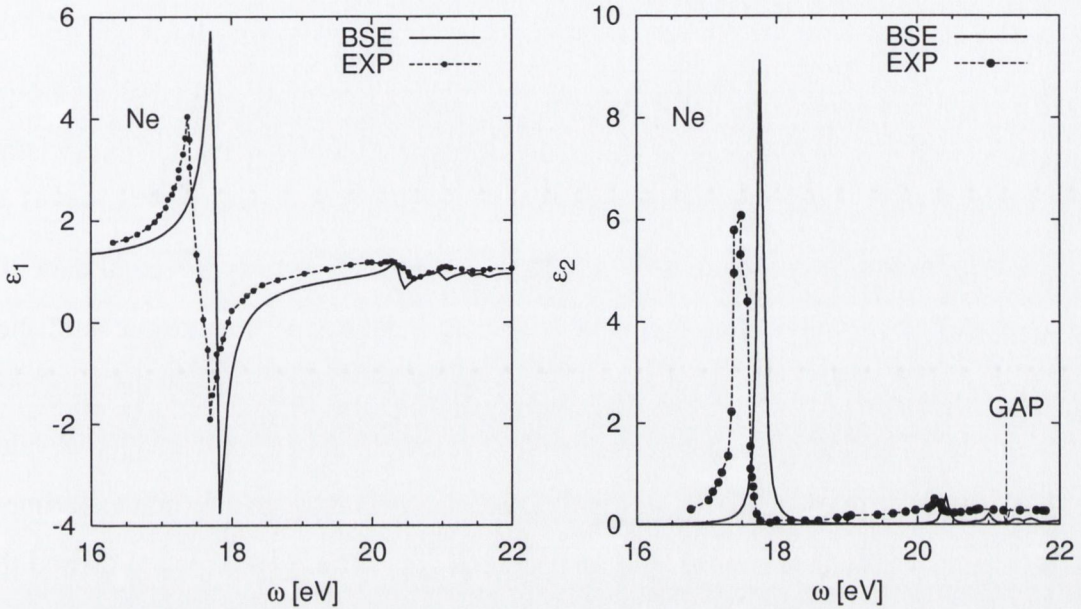


**Figure 6.5:** Real (left panel) and imaginary (right panel) parts of the macroscopic dielectric function for FCC Ne, calculated with excitonic effects included (BSE). Artificial broadening of 0.05 eV was used in the calculated spectra. The experimental data (EXP) is determined by Skibowski from reflection measurements cited in [77].

**Table 6.1:** Energy positions of the maxima detected in  $\varepsilon_2(\omega)$  of solid Ne. Our calculation is presented in column (1). Spin-orbit splitting is smaller than 0.1 eV, thus only spin-singlet,  $\Gamma(1/2)$  series is presented. The gap in the  $GW$  calculation and experiment are compared in the last row. All values are given in units of eV.

n	(1)	(2)	(3)	(4)
1	17.79	17.93	17.37	17.36 <sup>a</sup> ; 17.50 <sup>b</sup>
2	20.42	20.62	20.64	20.25 <sup>a</sup>
3	21.03	21.17	21.19	20.94 <sup>a</sup>
$E_g$	21.56			21.42 <sup>a</sup> ; 21.51 <sup>b</sup>

(2) Reference [109]. (3) Reference [110]  
(4)<sup>a</sup> Reference [111]. (4)<sup>b</sup> Reference [75]

experimentally, are described by the calculation as well. In both  $\varepsilon_1(\omega)$  and  $\varepsilon_2(\omega)$ , the main oscillator strength is in the low energy region (below the gap). As we can see there is remarkable agreement between the experimental and calculated spectra (Figure 6.5).

The positions of the first three peaks are tabulated in Table 6.1. Since, the spin-orbit interaction in Ne is small, only singlet  $j = 1/2$  type excitons were calculated. Our data, column (1) is compared to some earlier non-*ab initio* calculations: columns (2) by Grosso *et al.* [109], (3) by Martelli *et al.* [110] in Table 6.1 and experimental data (4). All our calculated peak positions lie in the range between the experimental and published data. More recent experiments obtained  $n = 1$  triplet peak at 17.36 eV and singlet at 17.50 eV [75]. This indicates that our value of 17.79 eV should be compared to the value of 17.50 eV rather than 17.36. Some small differences between our data and experiment can be due to the band structure. The fundamental gap of our *GW* calculation and the experiment is given in the last row of the table.

Intensities of the first peak for  $\varepsilon_1$  and  $\varepsilon_2$  are higher by about 2 eV than the experimental values. Although, one might address these deviations to the limited number of  $\mathbf{k}$ -points and limited resolution, we have to highlight experimental accuracy before bringing out conclusions about reliability of the calculation. As stated in [77], it was impossible to determine the errors of the absolute values of the reflectivity and there is much more uncertainty in intensities than in peak positions. In other words, experimental dielectric function intensities are not highly reliable in the case of the RGS, generally. A theoretical approach such as a *GW*-BSE calculation with a converged set of parameters can be superior to experimental measurements in this type of material.

## 6.4.2 Argon

One good example of intermediately bound excitons is argon. Figure 6.6 illustrates calculated macroscopic dielectric function for Ar with excitonic effects included (solid line) and experimental data (the dashed line left panel and circles with the dashed line is a guide to the eye, right panel) by Saile cited in [77]. The calculation is carried out using the parameters described in Section 6.1 and an artificial broadening of 0.05 eV, which

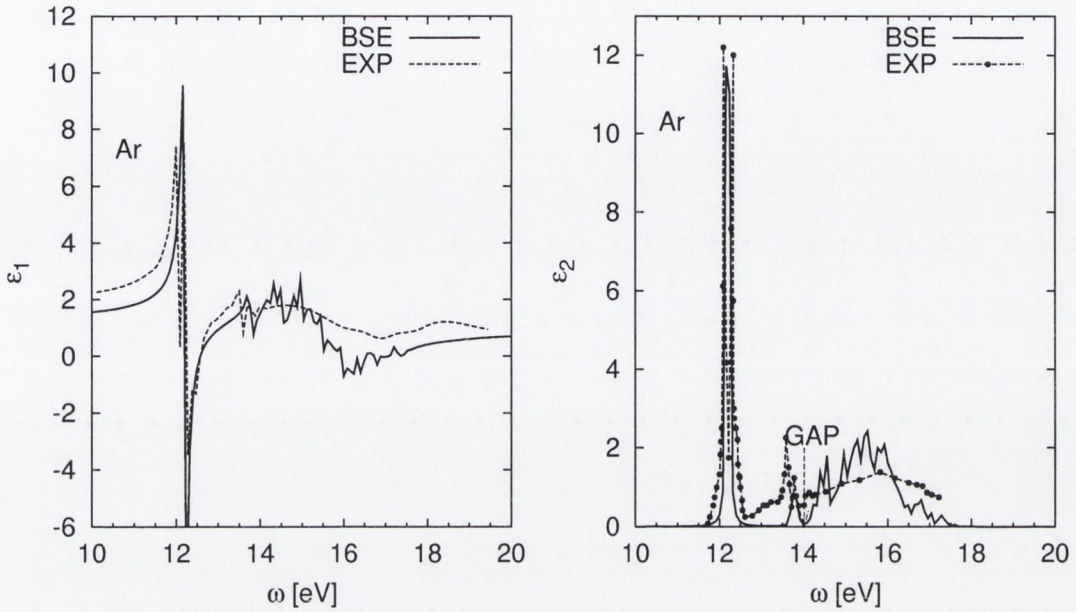


**Figure 6.6:** Real (left panel) and imaginary (right panel) parts of the macroscopic dielectric function for FCC Ar. Experimental data measured by Saile is cited in [77].

corresponds to the average resolution obtained by the given set of parameters. The experimental data is determined from reflectivity measurements by Saile [77].

Again, inclusion of excitonic effects changed the spectrum drastically and made remarkable agreement with experimental data for  $\varepsilon_2(\omega)$ .  $\varepsilon_1(\omega)$  agrees qualitatively with measurements by Saile. The oscillator in our calculation is stronger, while the dielectric constant  $\varepsilon_0$  slightly underestimates the measured value by Saile. However, the optical spectrum  $\varepsilon_2$  obtained by Saile for Ar is up to 40% higher than one determined by Skibowski as reported in [77], while they agree well with the maxima positions. When comparing spectra for RGS, experimental and calculated one should put more weight on actual peak positions rather than values of  $\varepsilon_1(\omega)$  and  $\varepsilon_2(\omega)$ .

The calculated spectrum includes singlet ( $j = 1/2$ ) excitons only, thus the splitting of the first exciton (the two sharpest maxima around 12 eV) is not present in our calculation, but only one maximum at energy 12.16 eV. The third peak in the experimental spectrum belongs to the triplet ( $j = 3/2$ ) series and is not visible in the calculation.

**Table 6.2:** Calculated (1) and experimental energy positions of the maxima detected in  $\varepsilon_2(\omega)$  for triplet and singlet excitons in solid Ar. The fundamental gap of our  $GW$  calculation and experimental gap are listed in the last row. The experimental data is by Skibowski cited in [77]. All values are in units of eV.

n	Type	(1)	Exp.
1	$\Gamma(3/2)$	12.00	12.09
1	$\Gamma(1/2)$	12.16	12.33
2	$\Gamma(3/2)$	13.76	13.58
2	$\Gamma(1/2)$	13.76	13.76
3	$\Gamma(3/2)$		13.91
4	$\Gamma(3/2)$		14.09
3	$\Gamma(1/2)$	14.4	
$E_g$		14.10	14.15

Since a magnitude of the spin-orbit interaction for Ar is only 0.18 eV which is much smaller than the actual exciton energies one can calculate singlet and triplet spectra separately (see Section 5.4). Energy positions of the maxima detected in our  $\varepsilon_2(\omega)$  spectrum for both triplet and singlet excitons are presented along with corresponding experimental peak positions in Table 6.2. Apart from the spin-orbit interaction a major difference between the singlet and triplet exciton energies comes from the exchange interaction,  $\Xi^x$  (5.41), which vanishes for triplet excitons. The exchange term originates from the repulsive bare Coulomb potential and shifts singlet excitons to higher energies than triplet excitons. The differences in the energies between singlet and triplet states in our calculation are direct measures of the exchange contribution. For the first exciton state  $n' = 1$  and  $n = 1$  the difference,  $\Gamma(1/2) - \Gamma(3/2)$  is 0.16 and 0.24 eV in our calculation and experiment, respectively. For higher states,  $n \geq 2$ , there is no splitting in the calculated spectrum and the differences in the experimental exciton energies are 0.17 eV, which is close to the spin-orbit interaction strength. Inclusion of the exchange interaction only affected the first exciton state and contributed to the singlet-triplet energy difference while the splitting of  $n \geq 2$  states is due to the spin-orbit interaction, mainly.

In conclusion, our calculated singlet spectrum agrees very well with experimental

data (related to the singlet excitations) in both intensity and maxima positions. Rapid oscillations in the range between 14 and 16 eV are due to the integration technique and limited number of  $\mathbf{k}$ -points. For determination of the spectra above 16 eV it is necessary to include more conduction bands. Moreover,  $\varepsilon_1$  spectrum underestimates the experiment at energies  $\omega < 12$  eV and convergence of  $\varepsilon_0$  may require more conduction bands as well. The dielectric constant  $\varepsilon_0$  is discussed again in Section 6.6.

### 6.4.3 Krypton

In krypton, the spin-orbit interaction becomes significant ( $\Delta_{so} = 0.6$  eV), but is still smaller than the electron-hole interaction. This fact allows us to apply the same approach, as we did for neon and argon, and study singlet and triplet states separately. The set of parameters used in the calculation has been presented in Section 6.1. The artificial broadening of 0.15 eV was introduced.

The calculated singlet  $\varepsilon_1(\omega)$  and  $\varepsilon_2(\omega)$  spectra are presented in Figure 6.7 (solid line). Experimental data (circles) is determined by Skibowski from reflectivity measurements at 20 K and taken from [77]. Peak positions agree with experiment very well for the first two singlet-type peaks. The spectrum in the from range 12 to 14 eV agrees with experiment. There are considerable discrepancies between reflectance measurements of Kr and Xe reported by different authors [77]. Not only do absolute reflectivities differ by more than a factor of two, but also the relative heights of the maxima vary drastically. It is clear that difficulties are encountered in experiments leading to uncertainty in dielectric functions.

All peak positions obtained in our calculation and in Skibowski experiments, [77] are listed in Table 6.3. The first ( $n' = 1$ ) singlet peak position of 10.92 eV agrees nicely with experimental value of 10.87(10.92) eV. States for  $n' \geq 2$  agree moderately well with Skibowski data. Difference between measured and calculated peak position for triplet  $n = 1$  state is due to omitted spin-orbit interaction. As was the case in Ar, the exchange interaction affected only the  $n' = 1$  state. Splitting of the other peaks originates mainly from the relativistic effects.

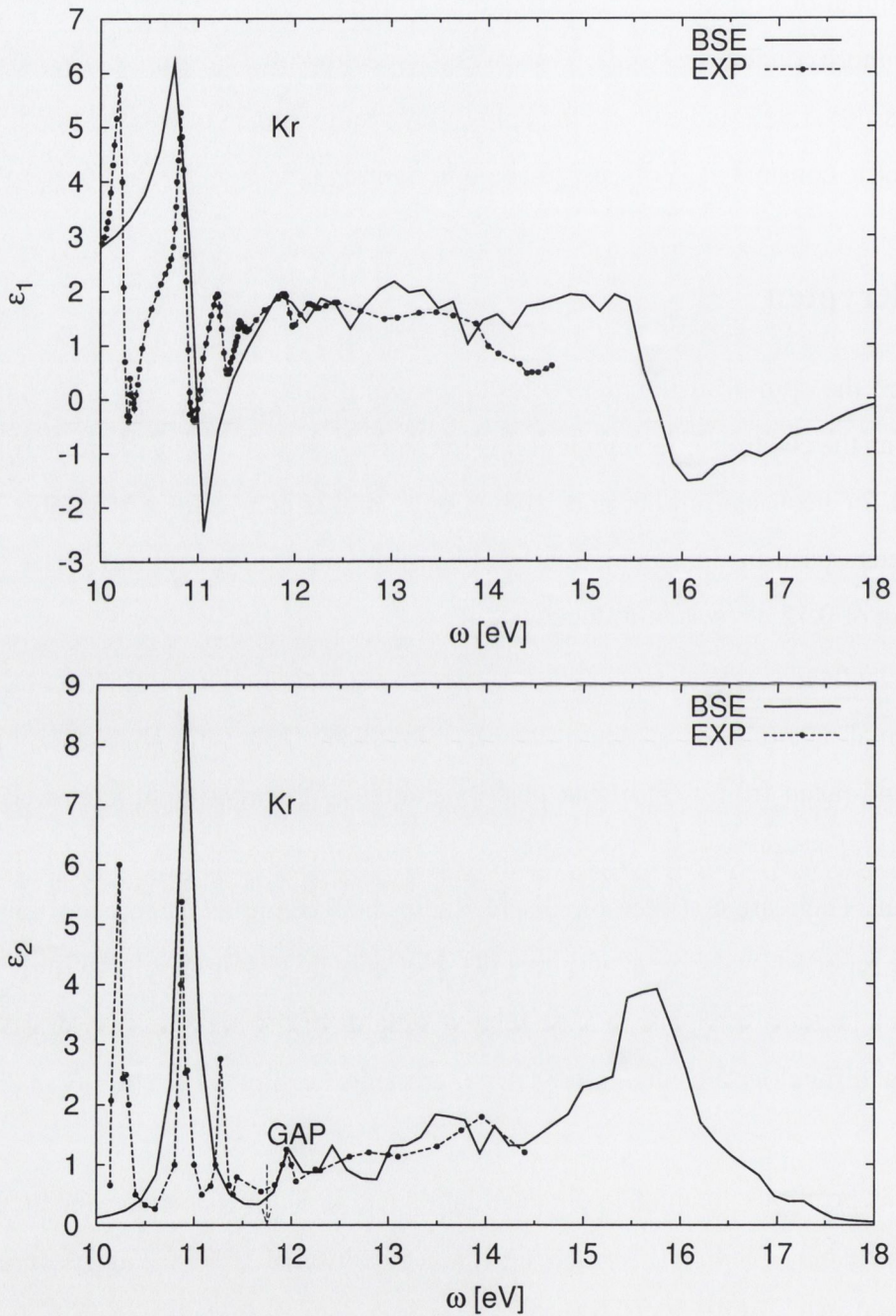


**Figure 6.7:** Real (upper panel) and imaginary (lower panel) parts of the macroscopic dielectric function for FCC Kr. Our calculation with excitonic effects included compared to the experimental data by Skibowski in [77].

**Table 6.3:** Calculated (1) and experimental peak positions detected in  $\varepsilon_2(\omega)$  for triplet and singlet excitons in solid Kr. The fundamental gap of our  $GW$  calculation and experimental gap are listed in the last row. All values are in units of eV. Experimental data is determined by Skibowski reported in [77]

n	Type	(1)	Exp.
1	$\Gamma(3/2)$	10.80	10.23 10.3
1	$\Gamma(1/2)$	10.92	10.87 10.93
2	$\Gamma(3/2)$	12.00	11.27
3	$\Gamma(3/2)$	12.50	11.44
2	$\Gamma(1/2)$	12.01	11.95
3	$\Gamma(1/2)$	12.5	12.22
$E_g$		11.61	11.75

An interesting feature of the experimental spectra is splitting of the first exciton states  $n = 1$  and  $n' = 1$  into two peaks each, at energies 10.23 and 10.3 eV for  $n = 1$  and 10.87 and 10.93 eV for  $n' = 1$ . This splitting disappears at a temperature of 8 K, so it is not expected to be seen in our theoretical approach. The origin of the splitting is not clear [77].

#### 6.4.4 Xenon

So far, it has been illustrated, when going from light Ne toward heavier Kr, relativistic effects are becoming more important. In Xe, the spin-orbit interaction is 1.3 eV, which is about the same order of magnitude as the electron-hole interaction. In such a case it is certain that coupling is close to the  $jj$ -coupling and the full spin structure as well as the spin-orbit interaction should be taken into account.

Nevertheless, we applied the same approach to Xe and results are presented in Figure 6.8. As we can see, there is no longer qualitative agreement between the calculated and experimental data. Peak positions are summarised in Table 6.4 and directly compared to the experiment. It can be seen that our  $n' = 1$  singlet peak coincides with experimental



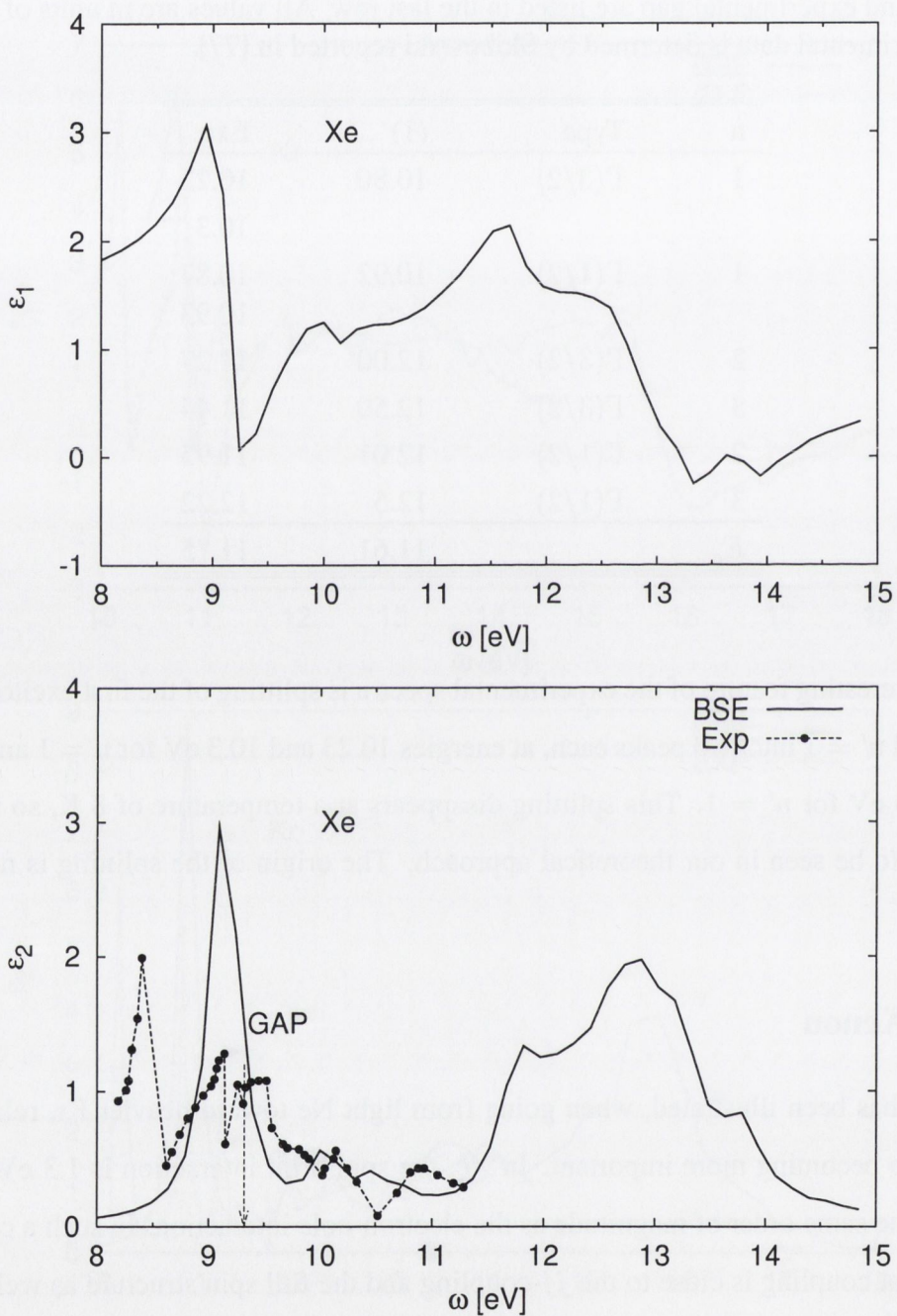


**Figure 6.8:** Macroscopic dielectric constants,  $\epsilon_1$  and  $\epsilon_2$ , with excitonic effects included (solid line) and experimental  $\epsilon_2$  (symbols joined by the line) for condensed Xe. The calculated spectra include only singlet excitations. The experimental data is taken from [77].

**Table 6.4:** Calculated (1) and experimental peak positions detected in  $\varepsilon_2(\omega)$  for triplet and singlet excitons in solid Xe. The fundamental gap of our *GW* calculation and experimental gap are listed in the last row. All values are in units of eV. Experimental data is determined by Skibowski in [77]

n	Type	(1)	Exp.
1	$\Gamma(3/2)$	9.25	8.4
2	$\Gamma(3/2)$	10.5	9.1
3	$\Gamma(3/2)$	10.75	9.2
1	$\Gamma(1/2)$	9.14	9.47
2	$\Gamma(1/2)$	10.03	9.8
$E_g$		9.63	9.32

$n = 2$  triplet state.

Difficulties with these experiments has been mentioned already. Particularly difficult was to observe  $\Gamma(1/2)$  series, because it overlaps with the the  $\Gamma(3/2)$  [75, 77]. However many different authors agree on peak positions if not with absolute or relative values of the reflectivity [77]. It would be worthwhile to include spin-orbit coupling in the Xe calculation before making any judgments.

### 6.4.5 Summary

In this section we presented results for the macroscopic dielectric function,  $\varepsilon_1(\omega)$  and  $\varepsilon_2(\omega)$ , for the RGS. The results for  $\varepsilon_2(\omega)$  are in excellent agreement with experimental data for Ne, Ar and Kr, and inclusion of the electron-hole interaction was crucial for a reliable description of the low energy spectra. Intensities of the spectra differ from measured values, however they are not highly reliable in experiments and experimental errors are unknown. Calculated peak positions deviate from measured ones mainly by spin-orbit coupling. These deviations are more pronounced in  $\Gamma(3/2)$  series then in  $\Gamma(1/2)$ . In Xe the spin-orbit interaction is larger than the electron-hole interaction and the current approach is not suitable. Peak positions in the spectrum of Xe deviate by more than 1 eV for the triplet states and by several tenths of an eV for singlet excitons (see Table 6.4).

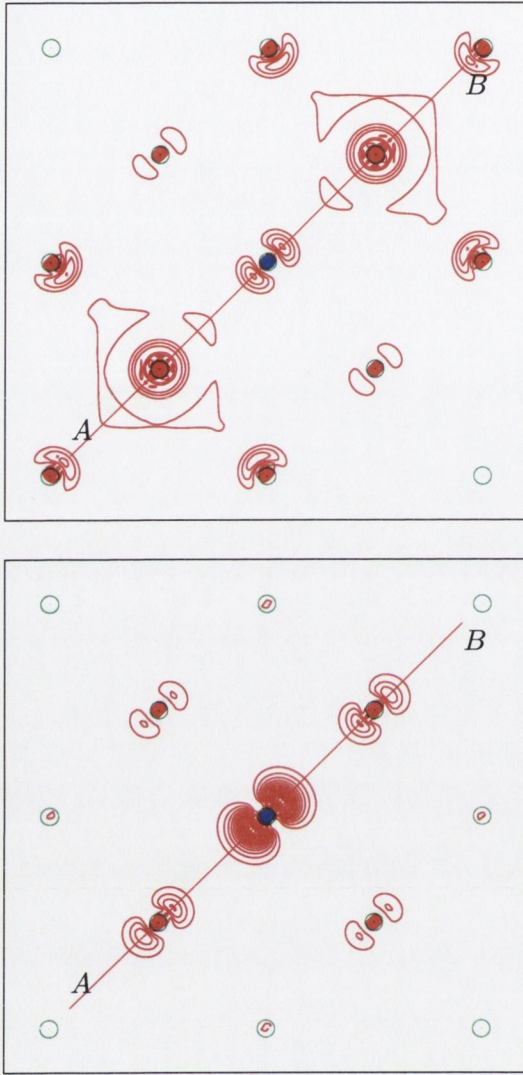


**Figure 6.9:** Contour plots of real space distribution  $|\chi(\mathbf{x}_h, \mathbf{x}_e)|^2$  of an electron ( $\mathbf{x}_e$ ) with respect to a fixed hole ( $\mathbf{x}_h$ ), upper panel and distribution of a hole with respect to a fixed electron, lower panel. The hole (electron) is fixed at the central atom (blue circle). The eigenvector corresponds to lowest energy excitation at 12.16 eV in Ar in the (100) plane. Data along the lines  $AB$  is presented in Figure 6.10. Green empty circles correspond to atom positions.

So far, we have not discussed line shapes for the first exciton peak,  $n = 1$  and  $n' = 1$  in any of RGS. The large value of the oscillator strengths is due to a strong interaction with the radiation field inside the crystal. In fact, the interaction is so strong that excitons cannot be treated separately. Mixed modes of the electromagnetic field and excitons are called exciton-polaritons. The line shapes, exciton transport and exciton decay have to be discussed within an exciton-polariton model and so they are not considered in the present work.

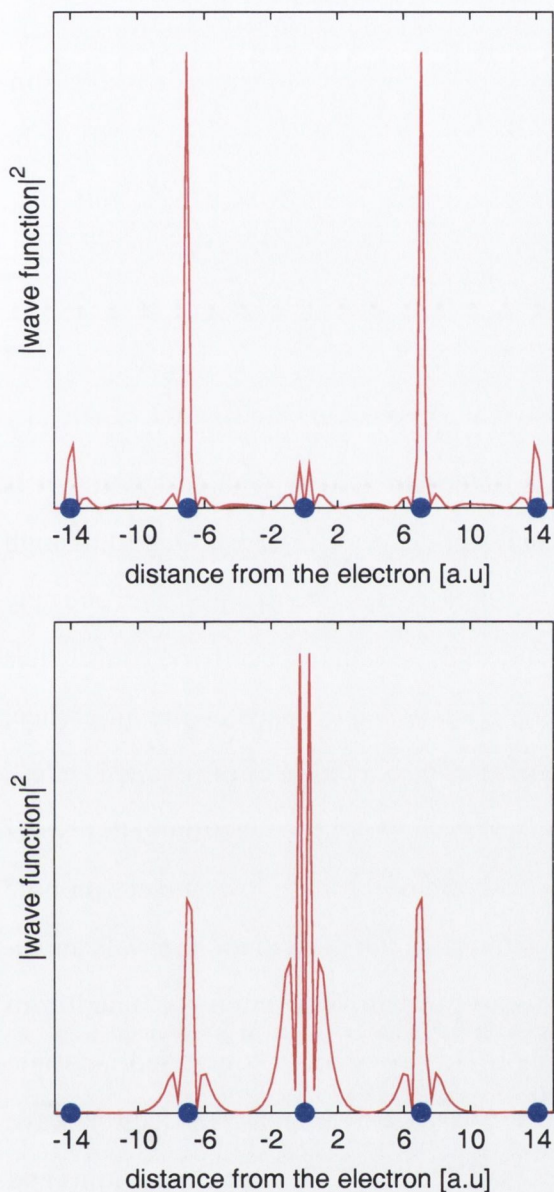


**Figure 6.10:** Same as Figure 6.9 along the line  $AB$ : electron distribution - upper panel, hole distribution - lower panel. Blue circles present atom positions.

## 6.5 Electron-hole wave functions for Argon

In the very early calculations [103, 104] it was observed that the first exciton ( $n = n' = 1$ ) in Ar is highly localised in real space with a radius less than the interatomic distance which violates the basic assumptions of the Wannier model and explains why the Wannier model does not describe the first exciton state in the RGS. However, the doubts emerged from the experimental findings of Laporte *et al.* [112, 113] according to which the excitons are delocalised at least over first nearest-neighbor atoms. The same conclusions

were made from theoretical calculations of Rössles [106] and Grünberg [108].

The current approach allows us to explicitly compute the wave function of an electron-hole excitation  $|n\rangle$ . The electron-hole wave functions are given by Equation (5.19) in the single-particle wave functions basis. For resonant transitions only, the coefficients  $B_{\mathbf{k}vc}^n$  are set to zero, thus the wave function obeys

$$\chi_n(\mathbf{x}_e, \mathbf{x}_h) = \sum_{\mathbf{k}} \sum_v^{\text{occ}} \sum_c^{\text{empty}} A_{\mathbf{k}vc}^n \psi_{\mathbf{k}c}(\mathbf{x}_e) \psi_{\mathbf{k}v}^*(\mathbf{x}_h). \quad (6.2)$$

The coordinates  $\mathbf{x}_e$  and  $\mathbf{x}_h$  refer to the position of the electron and hole, respectively. The wave function is a scalar six-dimensional function. In a crystalline system, it is invariant to the lattice translations simultaneously applied to  $\mathbf{x}_h$  and  $\mathbf{x}_e$ . Due to its high dimensionality, to get the best insight into electron-hole correlation in real space, one may keep either electron or hole at a fixed position and study  $\chi$  with respect to the coordinates of the other particle. This yields a correlation function which depends on the difference,  $(\mathbf{x}_e - \mathbf{x}_h)$ , but also includes all details of the microscopic structure of the excited states.

Figure 6.9 (upper panel) illustrates the probability of finding an electron with respect to a hole fixed at the central atom (blue circle in Figure 6.9) for the lowest electron-hole eigenvector which corresponds to the  $n = 1$  exciton state. Our calculation reveals an *sp*-type envelope function, what is not surprising, as we stated, the exciton is formed from the hole in a *p* state and an electron in an *s* state. However from a simplified isotropic effective-mass model this function would correspond to an hydrogen-like electron wave function. In addition, there is significant delocalisation over the first-neighbor atoms and even further with mean radius about 7 a.u. The delocalisation is extended along the line *AB* which confirms findings in [106, 108, 113]. The maxima of charge distribution in the (100) plane is on the nearest-neighbor atoms along the line *AB*. The lower panel of Figure 6.9 gives the hole distribution in the (100) plane with respect to the fixed electron at the central (blue) atom. Again, the charge is delocalised over the first-neighbor atoms with maximum (in the plane) of probability at the central atom. Figure 6.10 illustrates charge distribution along the line *AB* as a function of distance from the central atom. The charge distribution at the neighboring atoms is polarised toward the central atom. This is due to an attractive screened interaction between quasielectron and quasihole with

effective positive charge. Distributions for the second and third eigenvectors are similar to the first one, they differ only in the orientation of the envelope function.

Our results confirm conclusion from [106, 108, 113], which is that the first exciton is delocalised over the first first-neighbor atoms and give for the first time even more detailed information on the structure and symmetry of correlated electron-hole functions in real space in Ar. Figures 6.9 and 6.10 give clear picture why  $n = n' = 1$  excitons in rare gas solids are not described by either Frenkel- or Wannier-type exciton.

## 6.6 The Static Dielectric Constant

The approach described in Chapter 5 can be directly applied for the calculation of the static dielectric constant,  $\epsilon_0 = \Re[\epsilon(\omega = 0, \mathbf{q} \rightarrow 0)]$ . We calculated  $\epsilon_0$  for Si and RGS using RPA methods with and without local field effects, based on DFT-LDA eigenvalues, the RPA dielectric constant based on the *GW*-LDA quasiparticle energies and finally electron-hole interaction and Bethe-Salpeter equation in order to include the excitonic effects into  $\epsilon_0$ .

The results are presented in Table 6.5 and compared to the published theoretical (where available) and experimental data. The set of parameters given in Section 6.1 for RPA calculation was used for all materials. The LDA-RPA calculation without local field effects, (column  $\epsilon_{00}^{RPA}$ ) overestimates experimental values for Si, Ne, Ar and Kr. This effect is well known and Xe, as an exception, will be left out from further discussion. When local field effects were taken into account,  $\epsilon_0$  decreased and agreement with experiment was improved ( $\epsilon_0^{RPA}$  column). In addition, the calculation for Si, presented in row (b) is carried out using 10  $\mathbf{k}$ -points in the IBZ. Although, this data agrees very well with other plane wave data [29], as well as Gaussian orbital basis approach by Rohlfing [6], it is not fully converged. We presented this calculation because in [6], they also use only 10 points and the same basis set type, while in [29] 60 points were used [row (a) in Table 6.5] in the Brillouin zone summation. This indicates that the values in [6] may not be converged either. Our converged data for Si underestimates the plane wave data and agrees with the experimental value nicely. It is important to mention that we did not

**Table 6.5:** The Static dielectric constant,  $\epsilon_0$  for different materials. The table presents RPA calculations without local field effects (column 2), illustrates influence of the local field effects (column 4), quasiparticle corrections (column 6) and excitonic effects (column 7) and compares with experimental data (last column) and published data, columns indicated as (1), without local field effects and (2), with the local field effects included. Rows indicated as (a) and (b) for Si present converged calculations with 60  $\mathbf{k}$ -points in the IBZ included and using only 10 points, respectively.

	$\epsilon_{00}^{RPA}$	(1)	$\epsilon_0^{RPA}$	(2)	$\epsilon_{00}^{GW}$	$\epsilon_0^{BSE}$	Exp [114]
Si (a)	12.93	13.6 <sup>a</sup>	11.67	12.2 <sup>a</sup>	10.95 <sup>c</sup>		11.7
Si (b)	13.79		12.4	12.8 <sup>b</sup>			
Ne	1.38		1.28			1.26	1.24
Ar	1.98		1.70		1.79	1.63	1.66
Kr	2.13		1.80			1.75	1.86
Xe	1.52		1.40			1.32	2.18

<sup>a</sup>Reference [29].

<sup>b</sup>Reference [6].

<sup>c</sup>The local field effects are included

consider the exchange-correlation contribution [34]. It is expected that inclusion of the exchange-correlation kernel will increase the static dielectric constant and so worsen the agreement with experiment.

Good agreement between experiment and  $\epsilon_0^{RPA}$  is not surprising because a similar trend was observed by other authors [115] for wide-gap insulators. However when quasiparticle energies are used instead of LDA energies and local field effects are included the agreement was worsened by about 6% for Si. It seems that errors caused by LDA eigenvalues and exclusion of other (effects, exciton, exchange-correlation etc.) cancel out in wide-gap insulators. Generally, use of accurate band structures, such as  $GW$  together with local field effects, would lead to underestimation of  $\epsilon_0$ . This suggests that inclusion of excitonic effects along with quasiparticle energies could lead to a unified approach which would result in good experimental agreement for all materials regardless of the gap size.

As shown in Section 6.4, inclusion of excitonic effects is crucial for description of

optical spectra and thus can be of great importance for an accurate description of  $\varepsilon_0$  as well. The real part of the macroscopic dielectric function for the RGS was presented in Figures 6.5-6.8. Excitonic effects induced a positive contribution at lower photon energies leading to better agreement with experiment for spectra,  $\varepsilon_1(\omega)$  and  $\varepsilon_2(\omega)$  overall. This contribution arises from the transfer of oscillator strength toward lower energies.

This calculation is presented in Table 6.5 in  $\varepsilon_0^{BSE}$  column. As we can see, the errors introduced by the quasiparticle energies were canceled by the excitonic effects to a large degree leading to good agreement with experiment, again. Unfortunately, we still have to exclude Xe from our discussion since its  $\varepsilon_0$  is underestimated by nearly 90%. Small differences between calculated and measured values are of the same order of magnitude as differences in experimental data observed by different authors. Difficulties in experiments for these type of materials have been briefly discussed in Section 6.4, more detailed reading can be found in [77].

Despite a good agreement between the calculation and experimental values, we cannot guarantee that our values were fully converged.  $\varepsilon_1(\omega)$  was much more sensitive than  $\varepsilon_2(\omega)$  to choice of parameters, and so was  $\varepsilon_0$ . As suspected by Arnaud [100], a much larger number of  $\mathbf{k}$ -points,  $N_k$  and conduction bands,  $N_c$  may be required to calculate converged  $\varepsilon_0$ . Our findings confirm their belief that the set of parameters reported in Section 6.1 is not sufficient to calculate  $\varepsilon_0$  accurately. Calculations presented in Table 6.5 as  $\varepsilon_0^{RPA}$  were generated using 3 valence, 4 conduction bands and 864  $\mathbf{k}$ -points in full Brillouin zone. Fortunately, when we decreased  $N_k$  from 2048 to 864, the values of  $\varepsilon_0$  were changed by less than 1% (see Table 6.6). By using 864  $\mathbf{k}$ -points we were able to increase the number of conduction bands without increasing the size of the matrix, significantly. Unfortunately,  $N_c$  could not be increased and  $N_k$  kept reasonably large at the same time, so we cannot be certain that inclusion of the higher bands would not affect the value of  $\varepsilon_0$ .



**Table 6.6:** Convergence of  $\varepsilon_0$  for Ar and Kr with respect to  $N_c$  and  $N_k$  including excitonic effects.

$N_v \times N_c$	Argon		Krypton	
	$N_k = 2048$	$N_k = 864$	$N_k = 2048$	$N_k = 864$
$3 \times 1$	1.1798	1.1793	1.656	1.656
$3 \times 4$	–	1.63	–	1.755

## 6.7 Electron Energy Loss Function

In this section we want to address the energy loss function,  $-\Im(\varepsilon_M^{-1}(\omega))$  at higher energy, calculated within the RPA. We did not include excitonic effects in this calculation for the following reasons: firstly, a much larger number of conduction bands is required to obtain higher energy spectra and plasmon energies than we could use in the exciton calculations. Secondly, Olevano and Reining [116] calculated the energy loss function for silicon including *GW* and excitonic effects and they found that the *GW* corrections worsen the results with respect to the RPA calculation while inclusion of the electron-hole interaction improved the results with respect to both *GW* and RPA calculation only by taking into account the coupling between resonant and anti-resonant parts of the Hamiltonian (5.20), which was neglected in our calculations of the optical spectra.

The calculated energy loss function is presented in Figure 6.11 (left column) for the rare gas solids: Ne, Ar and Kr along with experimental data by Schmidt cited in [77] (right column). The DFT-LDA eigenenergies were used in the calculations for the reasons described in Section 6.2 and Ref. [116]. The full dielectric matrix in the  $\mathbf{q} \rightarrow 0$  limit is calculated at the range of frequencies and numerically inverted, so local field effects are included in the calculations. We cannot discuss absolute or relative weights for the spectra, since experimental weights are not known. However the most pronounced peaks and their positions match the actual experimental positions very well. Calculated peak positions are compared with experimental positions from Figure 6.11 in columns (a) for Ne and Ar and column (c) for Kr, Table 6.7. In addition, more recent measurements by Nuttall *et. al* [117] are presented in columns (b).

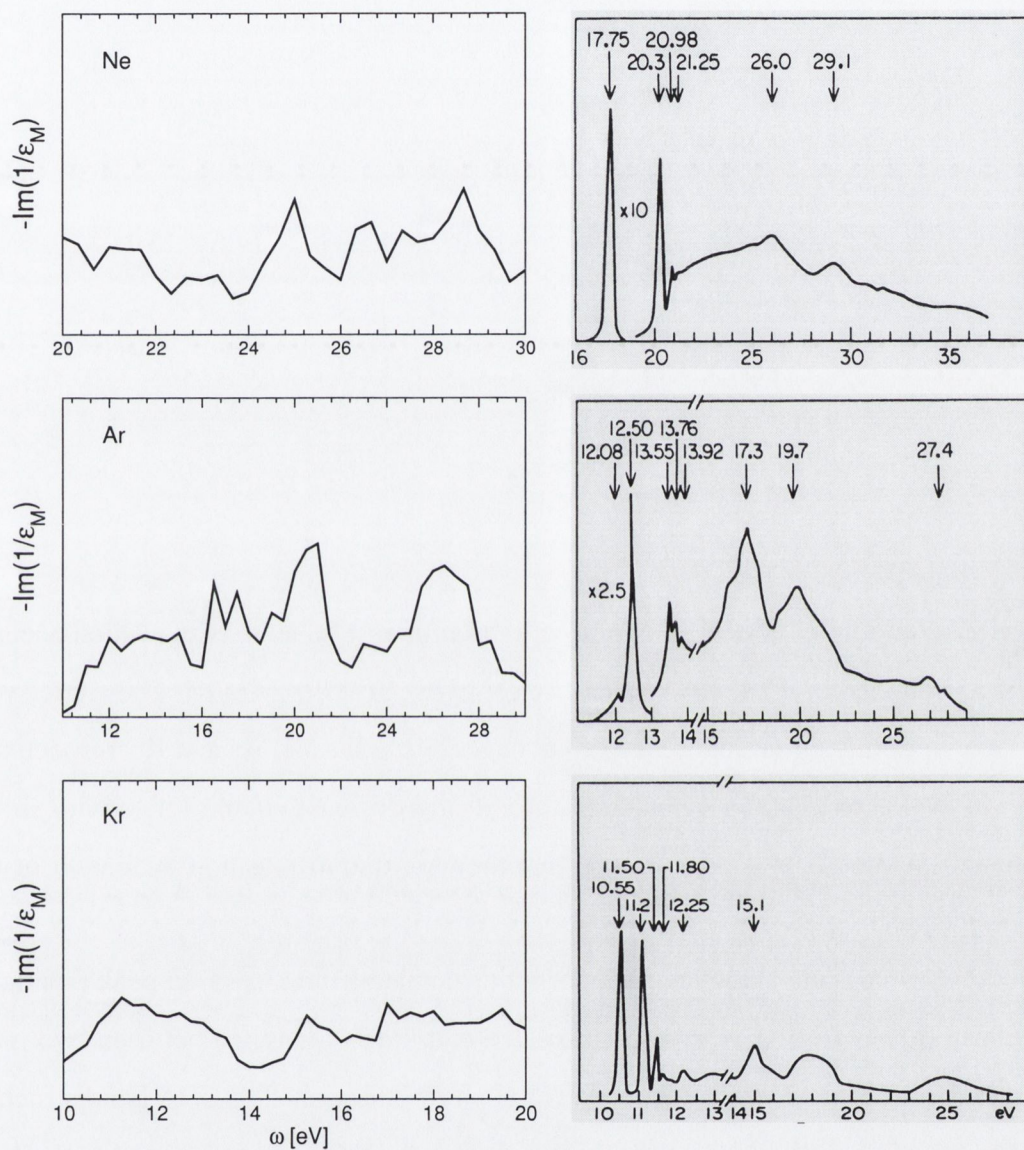


**Figure 6.11:** Energy loss spectra within the RPA (left column) for the rare gas solids: Ne, Ar and Kr. DFT-LDA eigenenergies were employed, and artificial broadening of 0.15 eV was introduced. Local field effects were included in the calculations by numerical inversion of the full dielectric matrix. Right column: experimental data obtained by Schmidt, 1971 for Ne and Ar, 1972 for Kr taken from [77].

**Table 6.7:** Energy loss function - calculated (RPA) and measured peak positions for solid Ne, Ar and Kr. Only peaks which originate from intraband transitions were tabulated here.

Neon		Argon			Krypton		
RPA	Exp.	RPA	Exp.		RPA	Exp.	
	(a)		(b)	(a)		(b)	(c)
25.0	26.0	16.5	16.5	16.5	12.5	12.6	
26.6	29.1	17.2	17.2	17.3	15.25	14.6	15.1
28.6	32.0		19.2	19.7		15.5	
		21.0	20.8		17.0	16.8	17.7
		26.5	26.4		18.0	17.9	18.5
					19.5	21.4	

(a) in [77] Ref. Schmidt 1971. (b) Reference [117].

(c) in [77] Ref. Schmidt 1972.

The most important maxima positions are the strongest broad maxima which occur in calculated loss spectra at 28.6 eV in Ne, 21.0 eV in Ar and 17.0 eV in Kr. They agree very well with experimental peaks at 32.0, 20.8 and 16.8 eV for Ne, Ar and Kr, respectively (Table 6.7). These maxima coincide with a strong decrease of the reflectivity in the reflectance spectra [77]. This indicates that they are due to plasmon excitation of the outer *p*-type electrons [77].

There is remarkable agreement between all calculated and measured peak positions, particularly for Ar and Kr where all calculated data lie in the range between two measurements. Less accurate results obtained for Ne may be ascribed to LDA band structure which underestimates the experimental one by more than 70%, (see Section 4.1.4). From this we can conclude that an RPA calculation, either with or without local field effects, can describe the high-energy spectra and plasmon energies moderately well for insulators as well as semiconductors. This justifies use of the RPA dielectric matrix in *GW* calculations.

# Chapter 7

## Conclusions

This thesis presents a detailed investigation of optical and dielectric properties of solids. In carrying out this study, two types of electronic excitations, single-particle and electron-hole excitations have been calculated within a reliable *ab initio* approach.

### 7.1 Single-particle Excitations

Unlike traditional *ab initio* calculations which use pseudopotential and valence electron plane wave basis sets, we employed all-electron localised Gaussian orbital (GO) basis sets in generating single particle states, while all two-point functions, such as dielectric functions and self-energies were expressed in a plane wave basis. This combined basis set approach, even if not the most efficient from the computational point of view, presents an important step forward in developing an approach for studying complex *d*-type systems and finite systems such as atoms, molecules etc, where conventional plane waves basis sets may not be applied.

In this combined basis we studied single-particle excitations within the *GW* approximation based on DFT-LDA single-particle states. We have shown that an all-electron GO approach yields a good description of the quasiparticle states around the energy gap. Calculated quasiparticle energies for bulk Si were in good agreement with experimental data and an all-electron projector augmented wave method by Arnaud and Alouani [62] and with pseudopotential calculations by Rieger *et al.* [5]. Calculation of the band structures for rare gas solids (RGS): Ne, Ar, Kr and Xe were also shown to be highly reliable within

the  $GW$  approximation. Values for the fundamental gap and valence band width are in good agreement with experimental values. However, higher conduction bands were not described very well, generally. Although, there is a large uncertainty in measured energies in rare gas solids, it would be worthwhile to replace our simplified plasmon-pole approximation by a more accurate plasmon-pole model given by Engel and Farid [39] or to use the space-time method by Rieger *et. al.* [5] for evaluation of the self-energy matrix elements. Nevertheless, accurate calculation of the valence bands and first conduction band in the rare gas solids was sufficient for studying electron-hole excitations and low-energy optical spectra.

Finally, we presented for the first time the  $GW$  quasiparticle band structure of cuprous oxide. This calculation was based on an initial self-consistent Hartree-Fock calculation. The calculated Hartree-Fock band gap overestimated the experimental value by about three times. We have shown that a large shift of the Hartree-Fock states results when  $GW$  corrections are applied leading to moderate agreement with experimental values. The  $GW$  band gap overestimated the experimental value by about 40% and self-consistent  $GW$  calculation may be required for a better description of the band gap when starting from Hartree-Fock eigenstates.

## 7.2 Electron-hole Correlation and Optical Spectra

The most challenging part of the thesis was studying electron-hole excitations and calculation of corresponding optical spectra. It was briefly illustrated that calculation of the dielectric function within the random phase approximation failed to produce reliable optical properties in semiconductors and insulators. Inclusion of local field effects improved the spectra in the high energy region but not at lower energies. It is shown that inclusion of both quasiparticle energies and electron-hole excitations was of crucial importance in an accurate study of optical spectra. Our absorption spectrum for silicon with the electron-hole interaction included improved agreement with experimental data, particularly the position of the first peak,  $E_1$  agrees well with the experimental value. The intensity of the spectrum and position of the second peak,  $E_2$  are slightly overestimated.

These discrepancies were due to an insufficient number of  $\mathbf{k}$  points in the integration. The calculated spectrum agrees moderately with experimental data and with the calculation by Onida *et al.* [11], which confirms its reliability. Taking a large number of special points (2048 or more) or shifted points and use of more accurate integration method such as that of Gilat-Raubenheimer [102] would be desirable for a more accurate description of optical spectra in semiconductors.

The electron-hole interaction is quite significant in the RGS and excitons are highly localised in real space and so delocalised in reciprocal space, which makes the RGS ideal systems to apply our approach to with a special points set. As a result we achieved an excellent agreement of absorption spectra with experiment for Ne and Ar in both peak positions and weights. Three excitonic peaks were detected and matched with experiment in both solids. The calculated spectrum for Kr was in qualitative agreement with experiment: peak positions agreed with experiment but not actual weights. Uncertainties in measured spectra for Kr and Xe were also discussed in Section 6.4. Relativistic effects turned out to be at least as important as excitonic effects for solid Xe. In such case it is certain that angular momentum coupling is  $jj$ -coupling. Agreement between experimental and calculated data was no longer qualitative and inclusion of the full spin structure and spin-orbit interaction is required.

Calculation of the electron-hole correlated wave function in real space for the first exciton state ( $n = 1$ ) of Ar revealed moderate localisation of the hole around a fixed electron position. The probability of finding the hole was slightly delocalised on the first and second neighbor atoms. The radius of the exciton was about the size of the lattice constant. The wave function was an  $sp$ -type function with polarisation toward nearest atoms. This conforms that these excitations belong to an intermediate regime between Frankel- and Wannier-type and confirms experimental findings in [113], and earlier calculations in [108, 106]. As stated in earlier publications, this explains the failure of the Wannier formula for exciton states  $n = n' = 1$  in rare gas solids, since the basic assumption of the Wannier model is violated.

We also achieved accurate calculation of the static dielectric constant for rare gas

solids, Ne, Ar and Kr, and illustrated the importance of including both quasiparticle corrections and electron-hole excitations in its calculation.

### 7.3 Outlook

An original and efficient computer code was developed to address all aspects in this thesis. Although, care has been taken to assure efficiency of the code with respect of the memory requirements, use of storage space and computational time, there are still some limitations. Some of them have already been mentioned in the text. It is possible to make improvements in the code and eliminate some of those limitations and extend the abilities of the code.

First of all, the study of exotic novel materials and highly correlated materials is not possible without spin structure taken into account as many of these materials do not have a spin-singlet for the ground state and cannot be described by a closed-shell model. Inclusion of spin structure and possibly the spin-orbit interaction is desirable and would extend the abilities of the code significantly. Application to open-shell systems would, on the other hand increase the number of basis states by a factor of 4 and evaluation of the Bethe-Salpeter equation would become even more difficult and more time consuming. One solution to this problem would be parallelisation of the code and use of vector computers with distributed memory. This could significantly cut down the computation time of the systems studied in this thesis and allow study of much larger systems. It is strongly recommended that further code development goes toward that direction.

The second source of difficulty arises from limitations in the CRYSTAL code. So far, the CRYSTAL95/98/03 generates eigenvalues and eigenvectors on a symmetric grid only and has limited  $\mathbf{k}$  points sampling to a maximum  $16 \times 16 \times 16$  grid (see Appendix A and Ref. [23, 26, 42]). As was shown in Si, this led to unconverged optical spectra. Advantage should be taken of shifted points and that would involve interpolation of single particle eigenfunctions and quasiparticle energies at arbitrary off-symmetry points, but that is a small price for the achievements gained; the required number of  $\mathbf{k}$ -points for fully converged spectra could be halved by this approach [13, 100]. Additional improvement

in the calculated spectra can be made by using an analytic continuation method [102] instead of the current root sampling method in integration over the Brillouin zone.

As already mentioned above,  $GW$  calculations can be improved by employing space-time [5] integration method instead of the plasmon-pole model. This approach would allow application to not only  $s$  and  $p$ -type materials for which the current plasmon-pole method works, but also  $d$ -type. The approach will yield highly reliable quasiparticle band structure not only for states around the band gap but also for higher energy states.

The code also provides great potential for excitations beyond  $GW$  calculation such as self-consistent, self-energy calculations,  $T$ -matrix [118] and electron-phonon coupling [119]. Implementation of the code with localised Gaussian orbital bases for two-point functions is already ongoing. The use of Gaussian orbital instead of plane-waves will provide applications to the finite systems such as atoms, molecules and clusters.

All suggested improvements in the code will give opportunity to study dielectric properties of different types of materials, transition metal oxides such as manganites and cuprates, high temperature superconductors such as  $MgB_2$ , conjugated polymers and many other novel materials.





# Appendix A

## Computer Code Manual

This appendix gives an overview of the computer code called SMEXCITON, originally developed and used to calculate all different quantities presented in this thesis. The appendix is divided into two main sections. Section A.1 gives detailed information about installing and running the code and documents the input and output files. Section A.2 is a guideline for further developers, it describes the structure of the code, memory requirements and data structure in detail.

### A.1 User Guide

The main part of the program is implemented in C++ programming language, but there are some FORTRAN77 source files used as well, which are mainly imported from external sources [120]. The source files and their purpose are discussed in more details in Section A.2. The program contains the following files and directories:

<code>suscep/README</code>	: short overview of the code
<code>suscep/INSTALL</code>	: installation instructions
<code>suscep/source/ * .cpp</code>	: C++ source files
<code>suscep/source/ * .f</code>	: FORTRAN77 source files
<code>suscep/source/Makefile</code>	: the make file
<code>suscep/include/ * .h</code>	: C++ include files
<code>suscep/source/ * .o</code>	: object files
<code>suscep/bin/smexciton</code>	: main executable
<code>suscep/bin/initdata</code>	: auxiliary executable

## A.1.1 Getting Started

The user is required to set up several parameters prior to the compilation. Firstly, the SMEXCITON code requires the CRYSTAL95/98 [26, 23] properties programs to be installed. The properties programs are called in run-time from the code so two macro variables CRYSTAL95\_CALL and CRYSTAL98\_CALL are defined in the file `suscep/include/param.h`. The file `param.h` has to be edited and their values set to the path of the each of the properties programs:

```
CRYSTAL95_CALL = "crystal95path"  
CRYSTAL98_CALL = "crystal98path".
```

Most memory allocation is done dynamically, however there are several static global arrays, and several user defined data types, e.g. matrices (see also Subsections A.2.2 and A.2.3). Their dimensions are defined by the parameters which are assigned in the file `suscep/include/param.h`. The user is advised to edit this file and check if these parameters comply with a studied crystal and computer's memory capacity and alter them if necessary. Alternatively, the code makes various run-time check ups and warns the user if the values of the parameters do not comply with the input data. The parameters and their meaning are:

MXBF	max. number of basis functions
MXGF	max. number of Gaussian primitives
MXSH	max. number of shells
MXK	max. number of $\mathbf{k}$ -vectors
MXG	max. number of $\mathbf{G}$ -vectors
MXSL	max. number of spherical shells for $\mathbf{R}$ , $\mathbf{G}$ -vectors
MXL	max. number of $\mathbf{R}$ vectors generated
MXBEH	max. number of bands in the electron-hole kernel calculation
MXKDIM	dimension of the electron-hole kernel

The Makefile is provided in the `suscep/source` directory and simply typing `make` in the same directory generates two executables: `smexciton` and `initdata`. The preferable compiler is `g++`, however, the code is portable and it does not use any special libraries so it can be adopted for any C++ compiler.

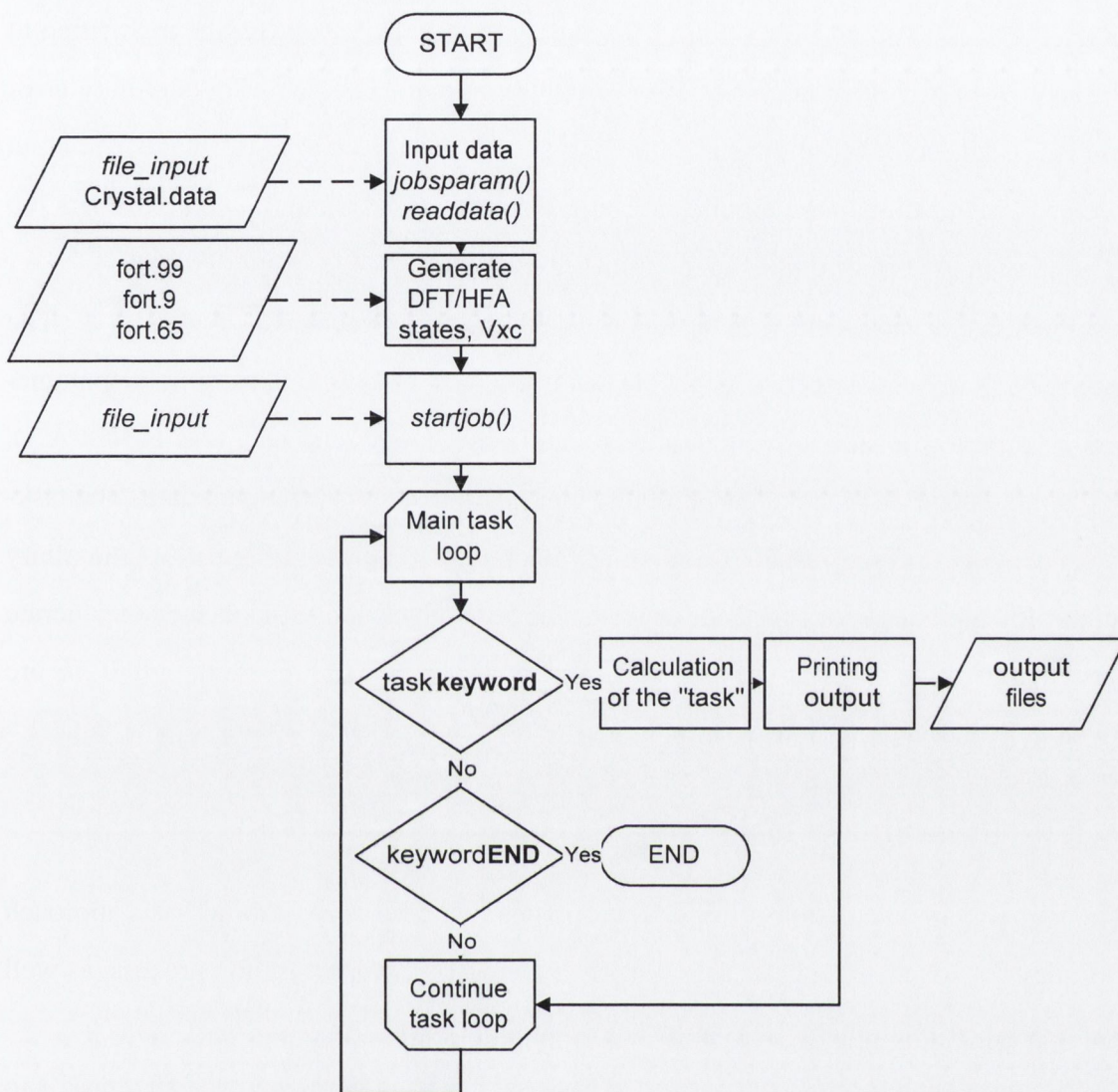


**Figure A.1:** The computational flow of the main calculation carried out with `smexciton` executable.

The main calculations are carried out by the `smexciton` executable, while the latter is used for preliminary calculations and it is discussed in the next subsection. The main executable takes two arguments, *input\_file* and *output\_file*, so the command line takes the form:

```
% smexciton [input_file_name] [out_file_name]
```

The *input\_file* is a user generated ASCII file. The output is written to the *output\_file* and to several task-dependent files. Optionally, some system information related to the

FORTTRAN call<sup>1</sup> might be written to the standard output file. All errors are written to the standard error file and an auxiliary error file, `error_file.log`. The auxiliary error file is introduced because the standard error stream is equivalent to the standard output stream, which prints to the monitor in some systems, so information can be lost if a job is running in the background and the user is logged off.

The computational flow of the main calculations is presented in Figure A.1. The *input\_file* is divided into two main blocks. The first block contains general parameters specific to the studied system and is read in the 'input data' task (see Figure A.1), while the second block contains particular computational task-dependent data. The task-dependent data is read inside the *startjob()* function. As shown in Figure A.1, auxiliary input files are required for the code as well. The next subsection explains how to generate them and gives an overview of their content. Details on how to prepare the *input\_file* are given in Sections A.1.3 and A.1.4.

## A.1.2 Preliminary tasks

The first step in calculations of optical properties in the Gaussian orbital basis approach is to develop an accurate basis set. A brief overview of the optimisation process, as well as basis sets used in this thesis are presented in Appendix C.

Assuming that a sufficiently accurate basis set has been developed, the first task is to generate the auxiliary input files: `Crystal.data`, `fort.99`, `fort.9`, `fort.65`<sup>2</sup> The files `fort.99` and `fort.9` contain the density matrix and they are generated by the CRYSTAL95 and CRYSTAL98, respectively. Thus, they are used by the `properties` programs during the system call. The file `fort.65` contains the exchange-correlation operator and it is used by the CRYSTAL98 `properties` program. The file `Crystal.data` contains all other relevant information gathered from the CRYSTAL95 calculation.

To generate these files, we run the `integrals` and `scf` executables of the CRYSTAL95 [26]. The procedure is schematically presented in Figure A.2. The `integrals` input file has to be named `dat.inp`. Standard output must be directed to a file entitled

---

<sup>1</sup>CRYSTAL95/98 programs `properties` are FORTRAN executables

<sup>2</sup>The default names for FORTRAN units are given by `fort.X` where X indicates the unit number.

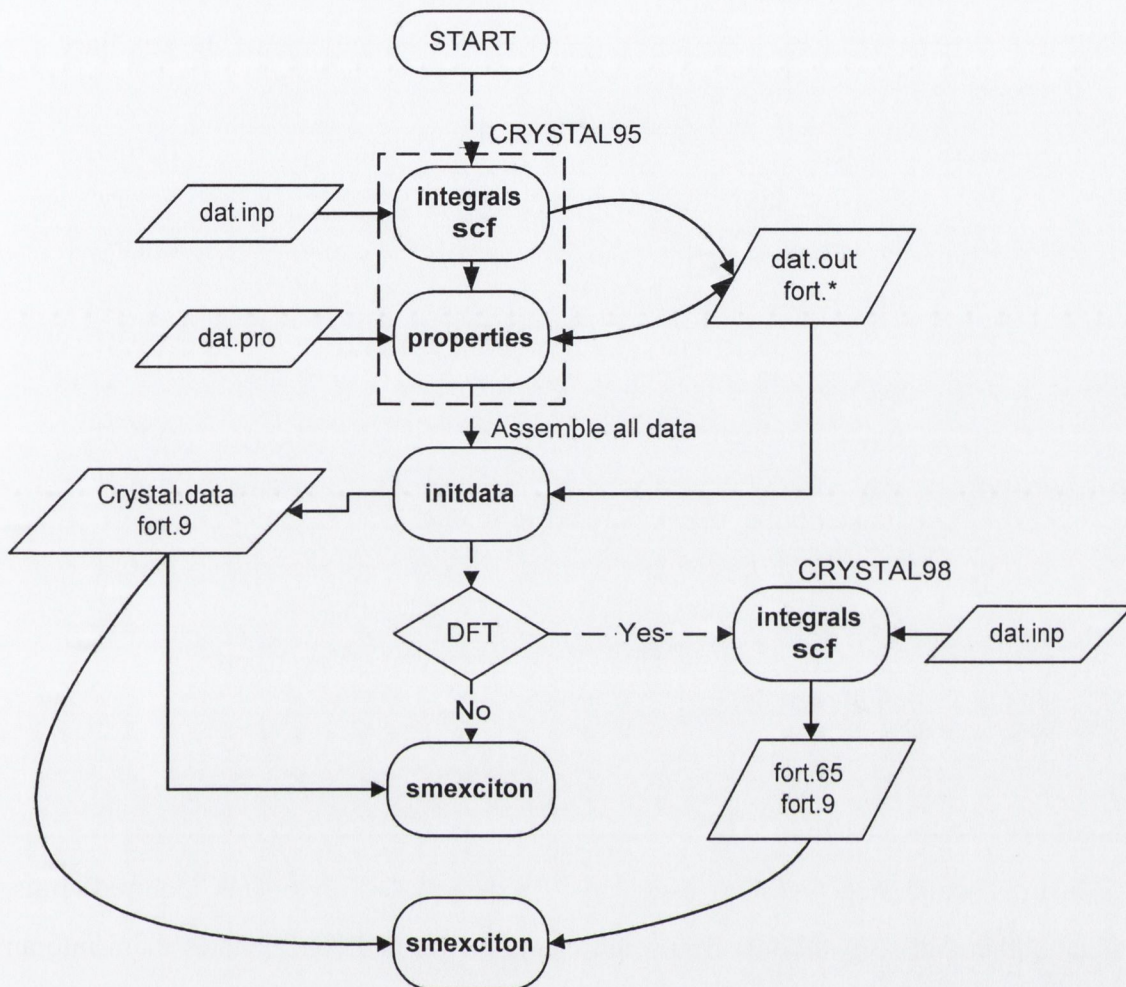


Figure A.2: Computational flow of the preliminary task.

dat.out. Following integrals and scf the CRYSTAL95 executable properties has to run using the following keywords in the input file: **NEWK**, **KNETOUT**, **EXTPRT**, **COORDPRT** [26]. The new **k**-point mesh generated by the **NEWK** option should have the same Monkhorst-Pack shrinking factors [60, 23] as specified in the scf part. The output from properties should be appended to the file dat.out. The command lines for the above have the form:

```

% integrals < dat.in > dat.out
% scf >> dat.out
% properties < dat.pro >> dat.out

```

This process results in the creation of several FORTRAN units, fort.X. The units created

**Table A.1:** Output files written by CRYSTAL95 used to generate the auxiliary input file `Crystal.data`.

Filename	Content	Created by	Format
fort.99	Density matrix, input to properties	NEWK	binary <sup>a</sup>
fort.10	Eigenvectors in the IBZ	SCF	binary
fort.30	Eigenvalues in the IBZ	NEWK	binary
fort.33	Lattice data, symmetry operators, non-primitive translation vector	EXTPRT	ASCII
fort.34	Accurate atomic positions	COORPRT	ASCII
dat.inp	Gaussian orbital basis set, standard integrals/scf input file	User	ASCII
dat.out	CRYSTAL95 standard output	integrals, scf, properties	ASCII

<sup>a</sup>All fort.X binary files are the FORTRAN type binary files, where data is written in records.

should include files listed in Table A.1.

In the second step the short executable `initdata` (no arguments required) runs, which gathers all relevant data from each of these files and concatenates them into an ASCII file, `Crystal.data`. The two files `fort.99` and `Crystal.data` should be kept for subsequent use.

Finally, some tasks of the main optical properties code require the exchange-correlation potential, which is generated by the CRYSTAL98 code. In order to extract this data, `integrals` and `scf` executables of the modified CRYSTAL98 code have to run in the same way and with the same input file as described for CRYSTAL95. This produces, in addition, `fort.9` and `fort.65` units. Both of them are binary units and used by the CRYSTAL98 program `properties` called during the main calculation. So they should be stored along with `fort.99` and `Crystal.data` files.

### A.1.3 General input task

The user generated input file contains an initial common block of general parameters, followed by various task-dependent optional blocks. Each block is arranged in lines of

**Table A.2:** Notation used in the description of the input data.

Symbol	Description
•	New record, keyword
◦	Optional record (switch keyword)
*	Free format
◊	<i>Input record follow some certain conditions</i>
<i>var</i> [#]	Record is an array of dim #.

*records*. The convention used in a description of the input data is presented in Table A.2.

The initial input block is specified with following records:

Record/Variable	Options/Keyword
• * title	
◦ SYMMETRY	<b>NOSYMM</b>
• * point_group	225, 227, 224, 186
• * shr shg itol	
• * iski isqi iskm iskpi	$\leq 16$
• * band_bottom band_top	band.bottom < band_top
◦ metal	<b>METAL</b>
• potential_type	<b>DFT, RHF</b>

**title** User comments, limited to 99 characters.

**SYMMETRY** Optional keyword **NOSYMM** switches all symmetry operations off. By default the symmetry is switched on in each task.

**point\_group** Specifies a type of point group, currently implemented only 186, 224, 225, and 227.

**shr shg itol** Various numerical control cutoff parameters:

**shr** The number of shells summed over in the real space to ensure correct normalisation of the Bloch functions, usually setting **shr** = 1 is sufficient.



**shg** The number of  $\mathbf{G}$ -vectors used in various summations, as well as the number that determine the actual size of the dielectric matrix. This number should be set to a value that defines a complete 'star' of  $\mathbf{G}$  vectors and it may not exceed the value set up by MXG.

**itol** This parameter determine a cutoff for calculation of one-electron integrals. Integrals involving shells of Gaussian orbitals whose largest overlap is less than  $10^{-itol}$  will be neglected. By introducing the cutoff in the integral calculation, the CPU time could be significantly reduced.

**iski isqi iskm iskpi** This record is related to the various 'shrinking factors' of the reciprocal lattice points. The  $\mathbf{k}$ -points mesh is discussed in Ref. [42]. At this stage we want to highlight that only multiples of 4 are permissible as shrinking factors. Various optical properties require different densities of  $\mathbf{k}$  points to achieve sufficient convergence, so four different shrinking factors are introduced in the code to ensure both accuracy and efficiency for all tasks. In addition, a common  $\mathbf{k}$  point mesh is generated by using the common shrinking factor

$$iskq = \max(iski, isqi, iskm, iskpi)$$

and all different  $\mathbf{k}$  and  $\mathbf{q}$  points meshes are scaled into this one. Thus, all four shrinking factors must be multiples of one another<sup>3</sup>.

**iski** Shrinking factor that determines the density of the Monkhorst-Pack  $\mathbf{k}$  point mesh for the integration over the BZ in the RPA dielectric matrix calculation (5.8).

**isqi** determines density of  $\mathbf{q}$  points used for different plotting purposes such as the quasi-particle band structure, dielectric band structure, Hartree-Fock and  $V_{xc}$  exchange operator plotted along lines in BZ, the self-energy spectrum and RPA optical spectrum.

---

<sup>3</sup>A maximal shrinking factor supported by CRYSTAL95/98 is 16.

**iskm** Shrinking factor of the Monkhorst-Pack  $\mathbf{q}$  point mesh for the integration over the BZ for the self-energy matrix element, (3.36) and Hartree-Fock exchange energy calculation.

**iskpi** determines the density of the  $\mathbf{k}$  point mesh used for the integration over the BZ in the optical spectrum with the electron-hole interaction included.

**band\_bottom band\_top** The first (occupied) and final (conduction) band used in the summations of the RPA dielectric function (5.8) and self-energy matrix element (3.36).

**metal** The code at the moment is not capable of automatically distinguishing metals from semiconductors and insulators so the keyword **METAL** is required for application to metals. The default case is non-metal.

**potential\_type** Calculation of the *GW*-DFT quasiparticle band structure requires the exchange-correlation potential generated by CRYSTAL98. Inserting the keyword **DFT** causes the CRYSTAL98 `properties` program to be called in run-time, while the keyword **RHF** switches off that call.

#### A.1.4 Optional Blocks

The initial input section is immediately followed by an input block specifying the requested calculation. The block is identified by the keyword at the beginning of that block, which is followed by the formatted input data. The input file can contain one or more of these blocks. All  $\mathbf{k}$ ,  $\mathbf{q}$  points given in an input file must be in oblique coordinates:

$$\mathbf{k} \equiv (k[0], k[1], k[2]) = \frac{k[0]}{isqi} \mathbf{b}_1 + \frac{k[1]}{isqi} \mathbf{b}_2 + \frac{k[2]}{isqi} \mathbf{b}_3, \quad (\text{A.1})$$

where  $\mathbf{b}_j$  are reciprocal primitive lattice vectors. All keywords are listed in Table A.3. A detailed description of the input data of all supported tasks, as well as a format of the output data is given below.

**SETPRINT** Printing selected output. All data is printed in the output file given by the second argument if not otherwise specified. All lengths are written in Bohr's units.

**Table A.3:** List of the task identification optional keywords.

Keyword	Description
<b>SETPRINT</b>	Various printing options
<b>RPA_DBS</b>	RPA dielectric band structure
<b>RPA_SPECTR</b>	RPA dielectric function
<b>EXCHENG</b>	HF exchange energy
<b>EXCHANGE</b>	HF exchange matrix element
<b>SE_PLOT</b>	<i>GW</i> self-energy vs. energy
<b>QP_BANDS</b>	<i>GW</i> Quasiparticle band structure
<b>PPTEST</b>	Plasmon-pole model test
<b>EXCITON</b>	electron-hole interaction
<b>END</b>	The program ends

The following options are supported:

**EIGENVEC** Prints eigenvectors in real space - see input below.

**EIGENVAL** Prints eigenvalues - see input below.

**GVECS** Prints **G** vectors - no input required.

**KVECS** Prints **k** vectors - no input required.

**ENDTASK** Termination of **SETPRINT** task.

**EIGENVEC** input:

Record/Options	Meaning
• * $n_k$ $1 \leq n_k \leq 10$	Number of <b>k</b> points
<i>Insert each <math>k_i</math> point for <math>i = 1 \dots n_k</math> in the separate record</i>	
◇ $k_i[3]$	The oblique coordinates for $k_i$
• * bands_m[2]	Lower and upper bands for printing
• * grid[3] grid[3] $\geq 0$	Number of points along <i>x</i> , <i>y</i> and <i>z</i> directions
• * origin[3]	Coordinates of origin (in Bohr's units)
• * griddim[3]	Lengths along <i>x</i> , <i>y</i> and <i>z</i> (in Bohr's units)

The real part of the eigenvectors are written in ASCII files, `eeigvec#.dat`, where `#` presents an ordinal number of **k**-points as appear in the input task.

The files have the following format:

eeigvec#.dat content			
<i>x</i>	<i>y</i>	<i>z</i>	$\Re(\psi_{m\mathbf{k}})$ ( $m = \text{bands\_m}[0] \dots \text{bands\_m}[1]$ )

**EIGENVAL** - input:

Record/Options	Meaning
• * $n_{\mathbf{k}}$	Number of <b>k</b> points
<i>Insert each <math>\mathbf{k}_i</math> point for <math>i = 1 \dots n_{\mathbf{k}}</math> in the separate record</i>	
$\diamond k_i[3]$	The oblique coordinates for $\mathbf{k}_i$

The **SETPRINT** task can support any number of subtasks and they can come in any order. The task must be terminated by **ENDTASK** keyword.

**RPA\_DBS** Random phase approximation dielectric band structure

Record/Options	Meaning
• * $n_{\text{eigenv}}$	Number of the dielectric matrix eigenvectors and eigenvalues printed out.
$1 \leq n_{\text{eigenv}} \leq \text{shg}$	
• * $n_{\mathbf{q}}$	Number of <b>q</b> points at which the dielectric matrix is computed.
$n_{\mathbf{q}} \geq 1$	
<i>Insert each <math>\mathbf{q}_i</math> point for <math>i = 1 \dots n_{\mathbf{q}}</math> in the separate record</i>	
$\diamond q_i[3]$	The oblique coordinates for $\mathbf{q}_i$

In this task the static symmetric dielectric matrix,  $\varepsilon_{\mathbf{G}\mathbf{G}'}(\mathbf{q}, \omega = 0)$  is calculated within the random phase approximation, (5.8) and diagonalised. The inverse of the eigenvalues,  $\varepsilon_n^{-1}(\mathbf{q})$  and eigenvectors  $V_{nl}(\mathbf{q})$  are written in the files:

Output filename	Content	Format
<code>rpa_dbs.dat</code>	$i \quad  \mathbf{q}_i  \quad \varepsilon_n^{-1}(\mathbf{q}_i), (n = 0 \dots n_{\text{of\_eigenv}})$	ASCII
<code>dm.eigenvectors</code>	$V_{nl}(\mathbf{q}_i)$	binary

The number of eigenvalues printed out, as well as the number of eigenvectors is determined by the first record, `n_eigenv`. The eigenvalues are printed in an ascending

order. Their matching eigenvectors are printed in a binary file as complex < double > quantities. The total size of the file is given by

$$size = n_q \times n\_eigenv \times MXG \times sizeof(\text{complex} < \text{double} >).$$

### RPA\_SPECTR Macroscopic dielectric function within RPA level.

Record/Options	Meaning
•* energy[2]	Lower and upper frequency bounds (in eV)
•* n_energy n_energy $\geq 1$	Number of frequency points
•* gamma gamma $\geq 0$	Artificial broadening parameter
•* n <sub>q</sub> $1 \leq n_q \leq 4$	Number of <b>q</b> points at which the dielectric matrix is computed
<i>Insert each <b>q</b><sub>i</sub> point for <math>i = 1 \dots n_q</math> in the separate record</i>	
◇ q <sub>i</sub> [3]	The oblique coordinates for <b>q</b> <sub>i</sub>

The symmetric dielectric matrix,  $\epsilon_{\mathbf{G}\mathbf{G}'}(\mathbf{q}, \omega)$  (5.8) is fully computed and numerically inverted at the range of frequencies. This provides for the study of the optical spectrum within the RPA level, with both local fields included and without local fields. Separate elements of the dielectric matrix<sup>4</sup>, macroscopic dielectric function,  $\epsilon_M(\omega) = \epsilon_1(\omega) + i\epsilon_2(\omega)$  and energy loss spectra (with local fields included) are printed in the ASCII files:

Output filename	Content		
RPAeGG#.dat	$\omega$	$\Re(\epsilon_{\mathbf{G}\mathbf{G}'}(\omega))$	$\Im(\epsilon_{\mathbf{G}\mathbf{G}'}(\omega))$
RPAeM#.dat	$\omega$	$\epsilon_1(\omega)$	$\epsilon_2(\omega)$
RPAloss#.dat	$\omega$	$\Re(1/\epsilon_M(\omega))$	$\Im(1/\epsilon_M(\omega))$

Again the symbol # is replaced by the **q**-point index.

<sup>4</sup>Supported elements at the moment are for  $\mathbf{G} = \mathbf{G}' = (0, 0, 0)$ ,  $\mathbf{G} = (0, 0, 0)$ ;  $\mathbf{G}' = (1, 1, 1)$  and  $\mathbf{G} = \mathbf{G}' = (1, 1, 1)$ .

**EXCHENG** Hartree-Fock exchange energy. No additional input required, however the number of  $\mathbf{k}$ ,  $\mathbf{q}$ , and  $\mathbf{G}$  vectors taken into account has to be chosen carefully [42], to ensure well converged calculation. This option allows relatively low-cost testing of convergence of the Hartree-Fock exchange operator, (4.3) computed as a part of the *GW*-DFT quasiparticle corrections. If the Hartree-Fock eigenenergies and wave functions are used in this calculation, then the converged exchange energy should correspond to the value obtained from CRYSTALxx<sup>5</sup> using a **UHF** Hamiltonian and the **EXCHGENE** keyword. The Hartree-Fock exchange energy is written in the output file given in the second argument of the command line, *output.file*. The energy is written in units of Hartree<sup>6</sup>.

**EXCHANGE** Hartree-Fock exchange operator.

Record/Options	Meaning
●* bands_m[2]	Lower and upper bands for plotting
●* n <sub>k</sub> n <sub>k</sub> ≥ 1	Number of $\mathbf{k}$ points
<i>Insert each <math>\mathbf{k}_i</math> point for <math>i = 1 \dots n_k</math> in the separate record</i>	
◇ $k_i$ [3]	The oblique coordinates for $\mathbf{k}_i$

In addition, the diagonal elements of the Hartree-Fock exchange operator,  $\Sigma_{ex}^{km}$  (4.3) are computed and plotted in a form of a band structure. If the **DFT** keyword is selected in the initial input block, matrix element of the DFT exchange-correlation,  $V_{xc}^{km}$  will be plotted as well. Auxiliary output files are both in an ASCII format and are listed below.

File	Content
vxc.dat	$i$ $V_{xc}^{k_i,m}$ , ( $m = \text{bands\_m}[0] \dots \text{bands\_m}[1]$ )
hfexchange.dat	$i$ $ \mathbf{k}_i $ $E_{ex}^{k_i,m}$ , ( $m = \text{bands\_m}[0] \dots \text{bands\_m}[1]$ )

<sup>5</sup>Any CRYSTAL release supports these options.

<sup>6</sup>1 Hartree = 27.211396130 eV.

## SE\_PLOT Self-energy diagonal matrix element as a function of energy

Record/Options	Meaning
•* bands_m[2]	Lower and upper bands for plotting
•* fit_type	Plasmon-pole fitting
<b>IMAG</b>	Imaginary type fitting
<b>REAL</b>	Real type fitting
•* fit_energy	
fit_energy $\neq 0$	Finite energy at which the dielectric matrix is fully calculated for the plasmon-pole model (eV)
fit_energy $< E_g$	If <b>REAL</b> type fitting is selected.
•* energy[2]	Lower and upper energy bound (eV)
•* n_energy	Total number of energy points to be considered
n_energy $\geq 1$	
•* gamma	Artificial broadening parameter for self-energy plot
•* n <sub>k</sub>	Total number of <b>k</b> points to be considered
n <sub>k</sub> $\geq 1$	
	<i>Insert each <b>k</b><sub><i>i</i></sub> point for <math>i = 1 \dots n_k</math> in the separate record</i>
◇ <i>k</i> <sub><i>i</i></sub> [3]	The oblique coordinates for <b>k</b> <sub><i>i</i></sub>

The self-energy matrix element,  $\langle m\mathbf{k}|\Sigma|m\mathbf{k}\rangle$  (3.36) is computed as a function of energy,  $E$  within the  $GW$  approximation (see Chapter 3), at a range of bands, from bands\_m[0] to bands\_m[1] and specified **k** points. The auxiliary output file, selfkk.dat is an ASCII file and has a structure:

selfkk.dat Content				
<i>i</i>	<i>m</i>	$E$ (eV)	$\Re(\Sigma_{\mathbf{k}_i m}(E))$	$\Im(\Sigma_{\mathbf{k}_i m}(E))$

*i* and *m* indicate **k**<sub>*i*</sub>-point and band index respectively. Data for each **k**<sub>*i*</sub> and *m* is stored in separate blocks followed by a blank line.

**QP\_BANDS** Quasiparticle correction to the either Hartree-Fock or DFT-LDA band structure

Record/Options	Meaning
•* bands_m[2]	Lower and upper bands for plotting
• fit_type	Plasmon-pole fitting
<b>IMAG</b>	Imaginary type fitting
<b>REAL</b>	Real type fitting
•* fit_energy	
fit_energy $\neq 0$	Finite energy at which the dielectric matrix is fully calculated for the plasmon-pole model (eV)
fit_energy $< E_g$	If <b>REAL</b> type fitting is selected.
•* gamma	Artificial broadening parameter for self-energy plot
•* delta_shift	Defines size of the interval for calculation of the functional derivative of $\Sigma(E)$ .
delta_shift $\neq 0$	
•* n <sub>k</sub>	Total number of <b>k</b> points to be considered
n <sub>k</sub> $\geq 1$	
	<i>Insert each <b>k</b><sub>i</sub> point for <math>i = 1 \dots n_k</math> in the separate record</i>
◊ k <sub>i</sub> [3]	The oblique coordinates for <b>k</b> <sub>i</sub>

The quasiparticle correction is calculated using the *GW* approximation. If the LDA eigenvalues and eigenvectors are used then the keyword **DFT** is required in the initial input block to ensure calculation of  $V_{xc}$ . Both the quasiparticle eigenvalues and LDA/HFA eigenvalues are printed in separate ASCII files :

File	Content
qpbands.dat $i$   <b>k</b> <sub>i</sub>	$E_{m\mathbf{k}_i}^{QP}$ ( $m = \text{bands\_m}[0] \dots \text{bands\_m}[1]$ )
hfbands.dat $i$   <b>k</b> <sub>i</sub>	$E_{m\mathbf{k}_i}^{SP}$ ( $m = \text{bands\_m}[0] \dots \text{bands\_m}[1]$ )

*SP* indicates either LDA or HF.



**PPTEST** Plasmon-pole model dielectric matrix:

Record/Options	Meaning
●* energy[2]	Lower and upper energy bounds (in eV)
●* n_energy n_energy ≥ 1	Number of energy points
●* gamma	Artificial broadening parameter
●* n_eigenv 1 ≤ n_eigenv ≤ shg	Number of the dielectric matrix eigenvalues printed out.
●* n <sub>q</sub> 1 ≤ n <sub>q</sub> ≤ 4	Total number of <b>q<sub>i</sub></b> points to be considered
	<i>Insert each <b>q<sub>i</sub></b> point for i = 1 . . . n<sub>q</sub> in the separate record</i>
◇ q <sub>i</sub> [3]	The oblique coordinates for <b>q<sub>i</sub></b>
● fit_type <b>IMAG</b> <b>REAL</b>	Plasmon-pole fitting Imaginary type fitting Real type fitting
●* fit_energy fit_energy ≠ 0	Finite energy at which the dielectric matrix is fully calculated for the plasmon-pole model (eV)
fit_energy < E <sub>g</sub>	If <b>REAL</b> type fitting is selected.

This task calculates the plasmon-pole approximation to the frequency dependent dielectric matrix as well as the full dielectric matrix at a range of frequencies. It is primarily meant for checking the reliability of the plasmon-pole model. Output files are all in ASCII format:

File	Content
real_fit#.dat	$\omega \quad \epsilon_n^{-1}(\omega) \quad (n = 1 \dots n\_eigenv)$
imag_fit#.dat	$\omega \quad \epsilon_n^{-1}(i\omega) \quad (n = 1 \dots n\_eigenv)$
real_numeric#.dat	$\omega \quad \epsilon_n^{-1}(\omega) \quad (n = 1 \dots n\_eigenv)$
imag_numeric#.dat	$\omega \quad \epsilon_n^{-1}(i\omega) \quad (n = 1 \dots n\_eigenv)$

The symbol # is replaced by an ordinal number, *i* of **q<sub>i</sub>** point listed in the input task.

**EXCITON** Program for the calculation the electron-hole interaction and properties related to it. This is the most time consuming task and the total calculation consists of several steps. In the first step, *GW* quasiparticle energies are generated for the set of **k** points in the IBZ. In the second step, the electron-hole interaction is calculated and the Bethe-Salpeter Hamiltonian diagonalised. Finally, properties such as the dielectric function or electron-hole eigenfunctions can be computed. In order to minimize the CPU time of the calculation the user is allowed to split the entire calculation into steps and calculate each step separately by choosing appropriate keywords. Thus, one could recalculate, e.g. the dielectric function using a different energy range or a different step without repeating the calculation of the electron-hole kernel or the *GW* energies which are the two most expensive parts of the computation. The input for this task has the following structure:

Record /Options	Meaning
•* bands_m[2]	Lower and upper electron-hole bands
• GW task	
<b>GWCALC</b>	Calculation of the quasiparticle energies - additional input required
<b>GWREAD</b>	Reading quasiparticle energies in IBZ - no input
• electron-hole interaction task	
<b>EHKERNEL</b>	Calculation of the electron-hole interaction - additional input required
◇ properties task	
<b>SPECTRUM</b>	Calculation of the macroscopic dielectric function - additional input required
<b>EHWAVEFUNCTIONS</b>	electron-hole wave functions in real space - additional input required
• <b>ENDTASK</b>	Termination of the <b>EXCITON</b> task

**GWCALC** Computes *GW* corrections for the set of **k** points in IBZ and for bands from bands\_m[0] to bands\_m[1] used in the calculation of the electron-hole excitations.

Record/Options	Meaning
• <code>fit_type</code>	Plasmon-pole fitting
<b>IMAG</b>	Imaginary type fitting
<b>REAL</b>	Real type fitting
•* <code>fit_energy</code>	
<code>fit_energy</code> $\neq 0$	Finite energy at which the dielectric matrix is fully calculated for the plasmon-pole model (eV)
<code>fit_energy</code> $< E_g$	If <b>REAL</b> type fitting is selected.
•* <code>delta_shift</code>	Defines size of the interval for calculation of the functional derivative of $\Sigma(E)$ .

This option writes all quasiparticle energies into binary the file `qpenergies`, which is used in follow-on calculations. The energies are written as a data type `double`.

**GWREAD** Once the *GW* quasiparticle corrections are calculated by the above option, the user can avoid repeating their calculation with this option. It is possible in the first run to calculate only the *GW* quasiparticle energies and in the second run to calculate the electron-hole interaction. This option is useful if the user has limited CPU time per process. The option does not require additional input, however it is required that the option **GWCALC** has been run before so that the file `qpenergies` exists. It is also assumed that the initial parameters, such as **k**, **q** points density or `bands_m[2]` are not changed between two runs. While the existence of the file 'qpenergies' is checked by the code, the latter two parameters are not checked and any change in them could result in unphysical solutions or cause dumping of the process.

**EHKERNEL** Electron-hole interaction calculation and solving the Bethe-Salpeter equation

Record/Options	Meaning
• screening_type	
<b>FULL_DM</b>	Full RPA DM in screening.
<b>DIAGONAL_DM</b>	Diagonal elements of the RPA DM only.
<b>OFF</b>	Screened potential switched off
• exciton_type	
<b>SINGLET</b>	( $j = 1/2$ )-type exciton
<b>TRIPLET</b>	( $j = 3/2$ )-type exciton

The electron-hole interaction kernel (5.39) can be computed by calculating the full RPA dielectric matrix in screening (**FULL\_DM**) (see Chapter 5), taking a diagonal approximation only, (**DIAGONAL\_DM**) or with the screening can be switched off (**OFF**). The last option, together with **SINGLET** exciton type is equivalent to taking only local fields into account. Separate calculation of the spin singlet and triplet exciton is possible, assuming that the magnitude of the spin-orbit interaction is negligible and the ground state is spin-singlet. The excitation energies,  $\Omega_S$  are written in an ascending order. The corresponding wave-function coefficients,  $A_{kvc}^S$  are written in the same order as  $\Omega_S$  in a binary file as the complex < double > data type. The output files are:

File	Content	Format
eh_eigenvalues.dat	$\Omega_S$	ASCII
eh.eigenvectors	$A_{kvc}^S$	binary

**SPECTRUM** Calculate the macroscopic dielectric function from the electron-hole states. The input data for this task is:

Record/Options	Meaning
•* energy[2]	Lower and upper energy bounds (in eV)
•* n_energy	Number of energy points
•* gamma	Artificial broadening parameter

The following ASCII output files are produced within this task:

Output filename	Content
e2.dat	$\omega \quad \varepsilon_1(\omega) \quad \varepsilon_2(\omega)$
loss.dat	$\omega \quad \Re(1/\varepsilon_M(\omega)) \quad \Im(1/\varepsilon_M(\omega))$

**EHWAVEFUNCTIONS** Calculation of the electron-hole wave functions in real space

Record/Options	Meaning
• <code>number_of_wfns</code> $1 \leq \text{number\_of\_wfns} \leq 10$	Number of wave functions
• <code>* grid[3]</code>	Number of points along $x$ , $y$ and $z$ direction
• <code>* origin[3]</code>	Coordinates of origin
• <code>* griddim[3]</code>	Lengths along $x$ , $y$ and $z$

The wave functions are computed for the hole fixed at the central atom. They are printed in the same order as they are written in the file `eh.eigenvalues`. Each function is printed in the separate ASCII file `eheigvec#.dat`

eheigvec#.dat content					
$x$	$y$	$z$	$\Re(\chi_s)$	$\Im(\chi_s)$	$ \chi_s ^2$

where the symbol `#` is replaced by index,  $s$  of the eigenfunction.

Note, if the properties tasks, **SPECTRUM** and **EHWAVEFUNCTIONS** are called without calling programs **GWCALC** or **EHKERNEL** in run-time, the user has to ensure that the files `qpenergies`, `eh.eigenvalues.dat` and `eh.eigenvalues` do exist and the setup which dictates the dimensions of the electron-hole kernel has not been changed between runs. The setup includes `bands_m[2]`,  $\mathbf{k}$  point mesh (shrinking factors) and `MXBEX` (see [42]).

## A.2 Programming Guidelines

### A.2.1 The code structure

The original source is written in C/C++ language. Some features of the C++ language are used, however overall programming style is C for simplicity. The features include the `complex < double >` class and reading and writing on binary files. The `complex` class is defined within GNU C++, and renamed as `Complex` in the code. It is simple to use and compatible with FORTRAN's `complex * 16` data type.

The code is developed mainly for computationally demanding problems with large memory requirements (2 GB or more). To handle such large memory requirements, the local file system is widely used instead of memory whenever possible. The `ofstream` and `ifstream` classes provide efficient writing and reading of large arrays in a file. Particularly efficient random access to stored data is provided by the `ifstream` class. For those reasons, all original source files have a `*.cpp` extension and they are required to be compiled by C++ compiler. However a developer is not required to have knowledge of truly C++ object oriented programming.

**Source files** The source files are:

**main.cpp** The primary source file for the program. It contains the function

```
int main(int argc, char * argv[])
```

which controls the reading of the input files and the designation of the computational tasks. All other functions contained in `main.cpp` or called from it are listed in the header file `main.h`.

**kpoints.cpp** All functions which are related to the **k** and **q** points, the general parallelepiped **k** point mesh, Monkhorst-Pack special points, symmetry information and the shifted points mesh.

**linear\_algebra.cpp** Source code dealing with the matrix algebra: multiplication, inversion, diagonalisation, etc. Actual diagonalisation and inversion routines are imported from an external source which is in FORTRAN77, so the header file `linear_algebra.h` in addition contains all necessary definitions for calling FORTRAN subroutines from a C++ source.

**tools.cpp** Functions for initialisation and printing of different type of arrays.

**integrals.cpp** Contains the main algorithm for the Gaussian orbital integration schemes.

**integrals\_qGzero.cpp** All functions for calculation of the momentum operator of the optical matrix elements.

**epsilon.cpp** All functions for the calculation of the RPA dielectric function, dielectric matrix and RPA polarisability. The two main functions which are directly related to the computational tasks are: `calc_RPA_spectrum()` and `calc_RPA_DBS()`. For more details of the data type passed in, as well as other functions programmed in this file, see the header file `epsilon.h`.

**setprint.cpp** Functions for general printing options.

**wave\_functions.cpp** Functions for the calculation of single-particle and two-particle wave functions in real space.

**self\_energy.cpp** Functions for the calculation of the self-energy matrix element, quasi-particle band structure and plasmon-pole model. Main calculation routines include:

- `QP_bands_plot()` Calculates quasiparticle band structure
- `self_energy_plot()` Calculate self-energy matrix element as a function of energy
- `plasmon_pole()` Plasmon-pole model testing

Details about declaration of the functions, data types and all other functions contained in the file are listed in the header file `self_energy.h`.

**HFexchange.cpp** Functions for calculation of the Hartree-Fock exchange matrix element and Hartree-Fock exchange energy.

**exciton.cpp** The source code dealing with the electron-hole interaction kernel and macroscopic dielectric function with excitonic effects included. The function,

`calc_exciton()`

is the major computational function of the code. Again, all additional functions, as well as some extra global data can be found in the file `exciton.h`.

In addition there are several FORTRAN77 source files which are mainly imported from external sources:

**init\_data.f** Source code for the preliminary data manipulation. The executable `initdata` gathers all relevant information from CRYSTAL95 code into `Crystal.dat` file. The source was originally written by Hogan [42] and it has been slightly changed since then.

The source files, **blas.f**, **dblas.f**, **cheev.f**, **dzasum.f**, **zblas.f**, **zggev.f** and **zgetri.f** are part of the the LAPACK library. We list them here and user/implementer is referred to [120] to find out more about these source files and their use.

**Include files** Each \*.cpp source file listed above has its own include file \*.h which contains all functions relevant to the source file and some global data relevant only for that source file. In addition, there are several more include files which are included in all \*.cpp files, if not specified differently:

**param.h** All dimensions/constants used in the declaration of static arrays and user generated data types (matrices).

**user\_data.h** The user defined data types.

**global\_data.h** All global data declared before `main()`. Included only in `main.cpp`.

**extern\_global\_data.h** same as above but included in all \*.cpp files except `main.cpp`.

**constants.h** contains all different physical/mathematical constants, such as  $\pi$ ,  $m_0$  electron mass, etc.

**conversion\_factors.h** defines conversion factors to CGS units.

**mycomplex.h** sets up proper header file for the complex numbers class, also defines type `Complex`,

```
typedef complex < double > Complex
```

**mylogical.h** defines data types `BOOLEAN` and `BYTE` if they are not defined. Also, it defines logical constants `TRUE = 1` and `FALSE = 0` and binary operators `OR` and `AND` which are more familiar to fortran programmers than the standard C/C++ operators `||` and `&&`.



## A.2.2 User defined data types

Several user defined data types were introduced in the code. This approach is taken mainly to simplify handling of linear algebra objects such as matrices and vectors and to generate so called data base 'cards' for objects which contain many different types of information related to one object i.e.  $\mathbf{k}$  points. All constants needed in these declarations are assigned in the param.h file (see previous subsection and Section A.1.1).

The major data types defined globally are:

```
typedef struct {
    int comp1 ;
    int comp2 ;
    int comp3 ;
} VECTOR_INT ;
```

This structure is used for vectors which have integers for components. It is used for the oblique coordinates of reciprocal lattice vectors. All introduced structures are new data types so it will be an error if one declares

```
struct VECTOR_INT k ;
```

instead, the correct declaration is

```
VECTOR_INT k ; .
```

```
typedef struct {
    double comp1 ;
    double comp2 ;
    double comp3 ;
} VECTOR_DOUBLE ;
```

A vector, with type double (real numbers) for components. The components are the actual coordinates  $x$ ,  $y$  and  $z$ , respectively. The lattice vectors are declared with this data type. One might think that the above two data types could be defined as a simple arrays of three elements, however the idea was to extend VECTOR\_DOUBLE and VECTOR\_INT structure into VECTOR class and defined the operators such as +, -, \* (dot product) and cross product (e.g \*\*) for the vector class.

```
typedef struct {
    VECTOR_INT oblique ;
    VECTOR_DOUBLE cart ;
} VECTOR_KNET ;
```

This structure is used for  $\mathbf{k}/\mathbf{q}$  points. Vectors in oblique coordinates are used for printing, while Cartesian coordinates are needed in an actual calculation.

```
typedef struct {
    int number_of_stars ;
    int symmetry_labels[48] ;
    int kfpointer ;
    double weights ;
} K_PROPERTIES ;
```

This structure is related to the  $\mathbf{k}$  points in the special Monkhorst-Pack set. It contains information related to the symmetry: `number_of_stars` is the number of points in the BZ belonging to the star of  $\mathbf{k}$ , `symmetry_labels[48]` is an array of symmetry labels which correspond to the symmetry operations from the little group of  $\mathbf{k}$ , `kfpointer` is the index of the eigenstate at a particular  $\mathbf{k}$  point and finally, `weight` is the geometrical weight of the  $\mathbf{k}$  point (see [42]).

```
typedef struct {
    Complex akfull[MXBF][MXBF];
} EIGEN_VECTOR ;
```

The matrix used mainly for single-particle eigenvectors. A value of `MXBF` is assigned in the file `param.h` and presents the maximum possible number of atomic orbitals, (see A.1.1).

```
typedef struct {
    double ekfull[MXBF] ;
} EIGEN_VAL ;
```

1D array used for single-particle eigenvalues.

```
typedef struct {
    Complex Matrix[MXG][MXG] ;
} DM_MATRIX ;
```

The matrix used in declaration of the dielectric matrix. MXG is assigned in the param.h file and presents the maximum number of **G** vectors.

```
typedef struct {
    Complex Matrix[MXKDIM][MXKDIM] ;
} K_MATRIX ;
```

The matrix used for electron-hole interaction kernel. The value of MXKDIM is required to be large, generally between 2000 and 11000. The latter number is a maximum value for the dimension of the complex < double > type matrix supported at computers with 2 GB of RAM. Since efficiency of diagonalisation depends of this constant, the user is recommended to alter this constant according to their own needs and keep its value as small as possible.

All the data types listed above can be found in the header file user\_data.h, which is included in all files.

### A.2.3 Global data

The most frequently accessed data has been declared globally prior to main() function. The data is declared in files global\_data.h and extern\_global\_data.h. In this subsection, we give a list of global variables and explain each variable.

Firstly, all data from the common input task (Section A.1.2) is stored as global data. Additionally, the common shrinking factor *iskq*, as well as some BOOLEAN type variables: SYMMETRY, metal and potential\_type, which are generated from the switch keywords (Section A.1.4) are also stored globally. Then the data taken from the file Crystal.data is stored as global data and can be divided into number of groups:

(1) All data mainly used in the Gaussian integration routines such as in integrals.cpp and integrals\_qGzero.cpp:

```
int ndf ;
```

The number of basis (Bloch) functions.

```
int ndf1 ;
```

The number of atomic orbitals, which differs from *ndf* if *d*-orbitals are present. 5 *d*-orbitals are expanded into 6 linearly dependent functions, which are recombined at the inclusion of the Bloch eigenvectors.

```
int nkf ;
```

The number of **k**-points in the irreducible Brillouin zone, as used in the initial CRYSTAL95/98 calculation. This number is not used in the current code, however it may become of use in some further version of the code in which the eigenvectors and eigenvalues would be used from a CRYSTAL special points grid and generated by symmetry and interpolation at the other required points.

```
int nexp ;
```

The number of Gaussian primitives.

```
double sc[MXGF], pc[MXGF], dc[MXGF] ;
```

These are the values of the contraction coefficients for *s*, *p* and *d* type Gaussian primitives.

```
double expo[MXGF] ;
```

Contains the value of the exponent of each Gaussian primitive.

```
VECTOR_DOUBLE xyz[MXGF] ;
```

the coordinates of the centers of Gaussian orbitals, usually situated at atom sites.

```
int ng[MXSH] ;
```

the number of Gaussian primitives in each shell.

```
int gpos[MXSH] ;
```

labels the index of the first primitive in a shell of all related arrays.

```
int shtype[MXSH] ;
```

labels the orbital type of each shell; 0 → *s*, 1 → *sp*, 2 → *p*, 3 → *d*.

```
VECTOR_DOUBLE ai[3], bi[3];
```

Primitive vectors of the real and reciprocal lattice, respectively.

```
double vol;
```

The volume of the primitive cell.

(2) All symmetry related data, also read from the file `Crystal.data`:

```
int number_symmetry_operators_inPointGroup;
```

Number of symmetry operators for the point group.

```
int irr[48 * 9];
```

Symmetry operators.

```
VECTOR_DOUBLE tauR[48];
```

Non-primitive translation vectors,  $\tau_R$  related to non-symmorphic groups.

There are several global arrays generated in run-time:

```
EIGEN_VAL single_part_val[MXK];
```

Single particle eigenvalues in a uniform grid in the parallelepiped. The common shrinking factor, `iskq` is used to generate the grid (see also ref [42]). The eigenvalues and eigenvectors are generated by using the C/C++ function `int system()` with the command line for running the `properties` program as an argument. While the eigenvalues are stored globally, the actual eigenvectors are written in a binary file `DFTstates` as the Complex data type.

```
EIGEN_VAL exchange_correlation;
```

The DFT exchange-correlation functional matrix element generated at the same grid as the single-particle eigenvalues and eigenvectors. At the moment only diagonal elements of the exchange-correlation potential matrix element are stored.

```
VECTOR_INT gvecs[MXG];
```

The reciprocal lattice vectors in oblique coordinates.

```
VECTOR.DOUBLE gvecs_bi[MXG] ;
```

The reciprocal lattice vectors in Cartesian coordinates.

```
VECTOR.DOUBLE Rvec_ai[MXL] ;
```

The real space lattice vectors in Cartesian coordinates.

```
int number_of_R_vectors ;
```

Total number of lattice vectors used the integration.



# Appendix B

## Static RPA Dielectric Matrix

The symmetrised dielectric matrix and the concept of dielectric band structure was mentioned in Section 3.5. Dielectric band structure is used to determine frequency dependent dielectric functions for  $GW$  self-energy matrix elements (3.31) within the plasmon-pole approximation. In this appendix we outline the formalism and illustrate the dielectric band structure concept through applications to silicon and FCC argon. The second aim of this appendix is to illustrate convergence of the inverse dielectric matrix, since it has been used for calculation of the screening in context of the self-energy and screened electron-hole interaction.

### B.1 Dielectric Band Structure

The longitudinal dielectric matrix of Adler [27] and Wiser [92] has been presented in Section 5.1 for semiconductors and insulators,

$$\begin{aligned} \varepsilon_{\mathbf{G}\mathbf{G}'}(\mathbf{q}, \omega) &= \delta_{\mathbf{G}\mathbf{G}'} + \frac{16\pi e^2}{\Omega} \frac{1}{|\mathbf{q} + \mathbf{G}|^2} \\ &\times \sum_{v,c} \sum_{\mathbf{k}} \frac{\langle c\mathbf{k} + \mathbf{q} | e^{i(\mathbf{q} + \mathbf{G}) \cdot \mathbf{r}} | v\mathbf{k} \rangle \langle v\mathbf{k} | e^{-i(\mathbf{q} + \mathbf{G}') \cdot \mathbf{r}'} | c\mathbf{k} + \mathbf{q} \rangle}{E_{c,\mathbf{k} + \mathbf{q}} - E_{v,\mathbf{k}} - \omega} \end{aligned} \quad (\text{B.1})$$

In Section 5.1 we have related the long wavelength  $\mathbf{q} \rightarrow 0$  limit of the dielectric matrix to the macroscopic absorption spectra. Here, we will focus on its static limit within the RPA  $\varepsilon_{\mathbf{G}\mathbf{G}'}(\mathbf{q}, \omega = 0)$ , since this limit determines static screening. In this context, the artificial broadening,  $0^+$  has been set to zero. Its application has been illustrated in determining the static and dynamic screening in computing the screened electron-hole interaction



and self-energy matrix elements, respectively. In these applications, the inverse of the dielectric matrix had to be calculated. Further applications were presented in the dielectric constant,  $\epsilon_0$ , calculation and RPA optical spectra in Sections 6.2 and 6.7.

Calculation of the DM for semiconductors and insulators can be drastically simplified by the concept of the dielectric band structure (DBS) introduced by Baldereschi and Tosatti [40]. The concept is based on dielectric eigenvalues and eigenpotentials which diagonalise the DM in the same way as the energy band structure and set of energy eigenfunctions diagonalise the Hamiltonian matrix. They allow a graphical representation of the DM.

The static DM, defined by (B.1), can be symmetrised by [94]:

$$\tilde{\epsilon}_{\mathbf{G}\mathbf{G}'}(\mathbf{q}) = \frac{|\mathbf{q} + \mathbf{G}|}{|\mathbf{q} + \mathbf{G}'|} \epsilon_{\mathbf{G}\mathbf{G}'}(\mathbf{q}) \quad (\text{B.2})$$

The matrix  $\tilde{\epsilon}_{\mathbf{G}\mathbf{G}'}(\mathbf{q})$  is Hermitian and therefore can be diagonalised as:

$$\sum_{\mathbf{G}'} \tilde{\epsilon}_{\mathbf{G}\mathbf{G}'}(\mathbf{q}) \tilde{V}_{n\mathbf{G}}(\mathbf{q}) = \epsilon_n(\mathbf{q}) \tilde{V}_{n\mathbf{G}}(\mathbf{q}) \quad (\text{B.3})$$

This will give a set of real eigenvalues  $\epsilon_n(\mathbf{q})$  and complex eigenvectors  $\tilde{V}_{n\mathbf{G}}(\mathbf{q})$ , and it can easily be proven that  $V_{n\mathbf{G}}(\mathbf{q}) = |\mathbf{q} + \mathbf{G}'|^{-1} \tilde{V}_{n\mathbf{G}}(\mathbf{q})$  are the eigenvectors of  $\epsilon_{\mathbf{G}\mathbf{G}'}(\mathbf{q})$  with the same eigenvalues  $\epsilon_n(\mathbf{q})$ , as well as eigenvectors of  $\epsilon^{-1}$  with eigenvalues  $\epsilon_n^{-1}(\mathbf{q})$ . We will consider only the symmetric dielectric matrix given by (B.2) and denote it by  $\epsilon_{\mathbf{G}\mathbf{G}'}$  for the remainder of this appendix.

The DM is defined in terms of its inverse (5.3), it is convenient to consider inverse eigenvalues  $\epsilon_n^{-1}(\mathbf{q})$ , which when  $\mathbf{q}$  spans the Brillouin zone, define a *dielectric band structure*. A real space dielectric eigenfunction, called an eigenpotential is given by:

$$V_n(\mathbf{q}, \mathbf{r}) = e^{i\mathbf{q}\cdot\mathbf{r}} \sum_{\mathbf{G}} V_{n\mathbf{G}}(\mathbf{q}) e^{i\mathbf{G}\cdot\mathbf{r}} \quad (\text{B.4})$$

When the crystal is perturbed with a weak external potential,

$$\delta V^{\text{ext}}(\mathbf{q} + \mathbf{G}') = V_{n\mathbf{G}}(\mathbf{q}),$$

it is straightforward to show from equation (5.3), that the screened potential is given by

$$\delta V^{\text{tot}}(\mathbf{q} + \mathbf{G}) = \sum_{\mathbf{G}'} \epsilon_{\mathbf{G}\mathbf{G}'}^{-1}(\mathbf{q}) V_{n\mathbf{G}}(\mathbf{q}) = \epsilon_n^{-1}(\mathbf{q}) V_{n\mathbf{G}}(\mathbf{q}). \quad (\text{B.5})$$

Its Fourier transform has the same  $\mathbf{r}$ -dependence as the perturbation, but is scaled by a constant factor  $\varepsilon_n^{-1}(\mathbf{q})$ . The dielectric band structure with corresponding eigenpotentials give us all essential information contained in the static dielectric matrix, particularly the deviations of the dielectric eigenvalues from diagonal values of the DM and of the dielectric eigenpotentials from plane waves (homogeneous limit) give us the magnitude of local field effects [40, 30].

## B.2 The RPA Response Function and Local Field Effects

The charge density response function,  $P$  or polarisability has been defined as a ratio between induced charge density and an external potential, (5.4). Within the RPA, calculation of the polarisability matrix,  $P_{\mathbf{G}\mathbf{G}'}$  takes only intraband transitions into account and local field effects are not included. However, it can be shown that local field effects (and exchange-correlation if it is considered) can be included in the polarisability via the relation [28]:

$$P_{\mathbf{G}\mathbf{G}'} = \sum_{\mathbf{G}''} \varepsilon_{\mathbf{G}\mathbf{G}''}^{-1} P_{\mathbf{G}''\mathbf{G}'}^0 \quad (\text{B.6})$$

The response matrix is Hermitian and can be diagonalised. Eigenvectors of  $P_{\mathbf{G}\mathbf{G}'}$  transformed into real space can be interpreted as a possible form of induced charge oscillation or plasmons [121].

## B.3 Convergence Parameters

The symmetric RPA dielectric matrix,  $\varepsilon_{\mathbf{G}\mathbf{G}'}(\mathbf{q}, \omega)$  has been calculated for all materials studied in the thesis. In this section we illustrate some convergence criteria of the dielectric matrix.

Equation (B.1) involves summation over occupied and conduction bands. It has been shown elsewhere that only valence electrons contribute to the summation over occupied states. This conclusion was confirmed in our calculations. In the summation over conduction bands we refer to Appendix C where the conduction band 'cut-off' was determined for each basis set considered in the thesis.

**Table B.1:** Some selected elements of DM for Si at  $\mathbf{q} \rightarrow 0$  limit, calculated using different basis sets and 256  $\mathbf{k}$ -points in FBZ, compared with published data.

$\mathbf{G}$	$\mathbf{G}'$	(42AO)	(52AO)	(88AO)	Ref [29]	Ref [33]
(0 0 0)	(0 0 0)	9.9126	13.7453	13.7954	13.610	15.4646
(1 1 1)	(0 0 0)	-0.2018	-0.3669	-0.4150	-0.441	-0.4665
(2 2 2)	(0 0 0)	0.1213	0.1637	0.1627		0.1767
(1 1 1)	(1 1 1)	1.1443	1.6325	1.7261	1.780	1.7976

By using the all electron basis sets for Si presented in Appendix C we calculated some selected elements of the static dielectric matrix at  $\mathbf{q} \rightarrow 0$ . The data is presented in Table B.1 and compared with published data (last two columns). Two main conclusions can be drawn from the table: (1) A large basis set is required to produce a dielectric matrix which is comparable with fully converged plane-wave data. (2) For elements at large  $\mathbf{G}$ -vectors even more conduction bands are needed to achieve good agreement. The table shows that using a relatively large basis set (88AO), the 'head' element is larger by about 1.2% than the result obtained with a plane-wave basis in [29], the 'wing' and 'body' elements differ from the published data by about 2% and 5%. These deviations are mainly due to an insufficient number of conduction bands, and they are even larger for the smaller basis sets. It is shown in Appendix C that only 45 conduction bands contribute to the calculation for the largest 88 AO basis set. However, the exact matrix elements are not known, and measurable quantities such as  $\epsilon_0$  or optical spectra are comparable with published and experimental values (see Section 6.6). For calculation of these quantities only the 88 AO basis set was used for silicon.

After the number of conduction bands, the most important factor in the dielectric matrix calculation is the Brillouin zone integration. The integration is carried out using the Monkhorst-Pack special points scheme [60]. Convergence of different dielectric matrix elements is examined and presented in Table B.2 for Si using the largest basis set, 88 AO. Very good convergence is achieved for the 'wing' and 'body' elements with 256  $\mathbf{k}$  points, however the 'head' element for  $N_{\mathbf{k}} = 256$  deviates by about 7% from the element

**Table B.2:** Some selected DM elements and  $\varepsilon_0^{RPA}$  (last row) for Si calculated using different number of  $\mathbf{k}$ -points in FBZ, using 88 AO basis set. Displayed elements are calculated at  $\mathbf{q} \rightarrow 0$  limit, the matrix size  $59 \times 59$  was inverted in obtaining  $\varepsilon_0^{RPA}$ .

$\mathbf{G}$	$\mathbf{G}'$	$N_{\mathbf{k}} = 256$	$N_{\mathbf{k}} = 864$	$N_{\mathbf{k}} = 2048$
(0 0 0)	(0 0 0)	13.795	13.021	12.939
(1 1 1)	(0 0 0)	-0.415	-0.415	-0.415
(1 1 1)	(1 1 1)	1.726	1.725	1.725
$\varepsilon_0^{RPA}$		12.47	11.73	11.65

obtained with  $N_{\mathbf{k}} = 2048$ , there is the same error in the value for  $\varepsilon_0^{RPA}$ . Nevertheless, we used a mesh of the 256 points in the calculation of the screening [see Equations (3.30 and 5.39)]. This mesh was used by Rohlfing *et al.* [6] and resulted in a good band structure for different materials. Also, Rohlfing *et al.* [6] examined different models for the dielectric matrix and they showed that the choice of the dielectric matrix is not crucial for calculation of the self-energy, since it is rather averaged over the Brillouin zone. According by we limited ourselves to use only 256  $\mathbf{k}$ -points in the FBZ (or 10 points in the IBZ) for the dielectric matrix calculation in the context of  $GW$  self-energy and screened electron-hole interactions for all materials. This was motivated by large savings in the computation time when the DM was computed at a large number of  $\mathbf{q}$ -points, such as in the electron-hole interaction. However for determining an optical spectrum or dielectric constant, a fully converged dielectric function was used (see Section 6.1).

Finally, when the dielectric function was transformed into reciprocal space (5.2), vectors  $\mathbf{G}$  and  $\mathbf{G}'$  span the infinite reciprocal lattice. However, in a realistic calculation some cutoff has to be introduced. Converged inverse dielectric matrices  $\varepsilon_{\mathbf{G}\mathbf{G}'}^{-1}$ , or converged eigenvalues and eigenvectors of the dielectric matrix require a sufficiently large matrix to be calculated. Table B.3 shows the convergence of the dielectric constant,  $\varepsilon_0$  with local fields included for Si, Ne, Ar and Kr. Well converged results were achieved after 59  $\mathbf{G}$ -vectors for Si and the RGS, including Xe (not shown). The choice of 59  $\mathbf{G}$  vectors for converged dielectric constant was also supported in literature [62, 42]. In our case  $\varepsilon_0$

**Table B.3:** Convergence properties of the dielectric constant for different materials with respect to the size of the dielectric matrix when the local field effects were included. The size used in the calculations in Chapters 4, 5 and in following section is indicated in bold.

$N_G$	Si	Ne	Ar	Kr
1	13.79	1.38	1.98	2.13
15	13.05	1.287	1.704	1.802
27	12.833	1.287	1.701	1.801
<b>59</b>	<b>12.478</b>	<b>1.286</b>	<b>1.701</b>	<b>1.800</b>
65	12.474	1.286	1.700	1.800
89	12.468	1.285	1.700	1.797
113	12.464	1.285	1.700	1.796
137	12.464	1.284	1.699	1.795
169	12.464	1.283		1.795

converges to less than 1% for all materials studied here.

## B.4 Results and Discussion

The dielectric band structures are calculated for Si and Ar and presented in Figure B.1. As stated in Section B.1 an external potential can be expressed in the form of dielectric eigenpotentials or, generally, any arbitrary potential of a given symmetry can be decomposed into eigenpotentials of the same symmetry [40]. Thus, screened potentials inside the cell are given by a set of dielectric eigenpotentials reduced by screening factors, eigenvalues of  $\epsilon_n^{-1}(\mathbf{q})$ , equation (B.5). The induced charge density can be presented in

**Table B.4:** Smallest inverse eigenvalues of  $\epsilon_{\mathbf{G}\mathbf{G}'}^{-1}(\mathbf{q} \rightarrow 0)$ . The number in brackets indicates the degeneracy

	$\epsilon_1^{-1}$	$\epsilon_2^{-1}$	$\epsilon_3^{-1}$	$\epsilon_4^{-1}$
Si	0.071	0.398	0.517(2)	0.537
Ar	0.384	0.476	0.508(2)	0.723

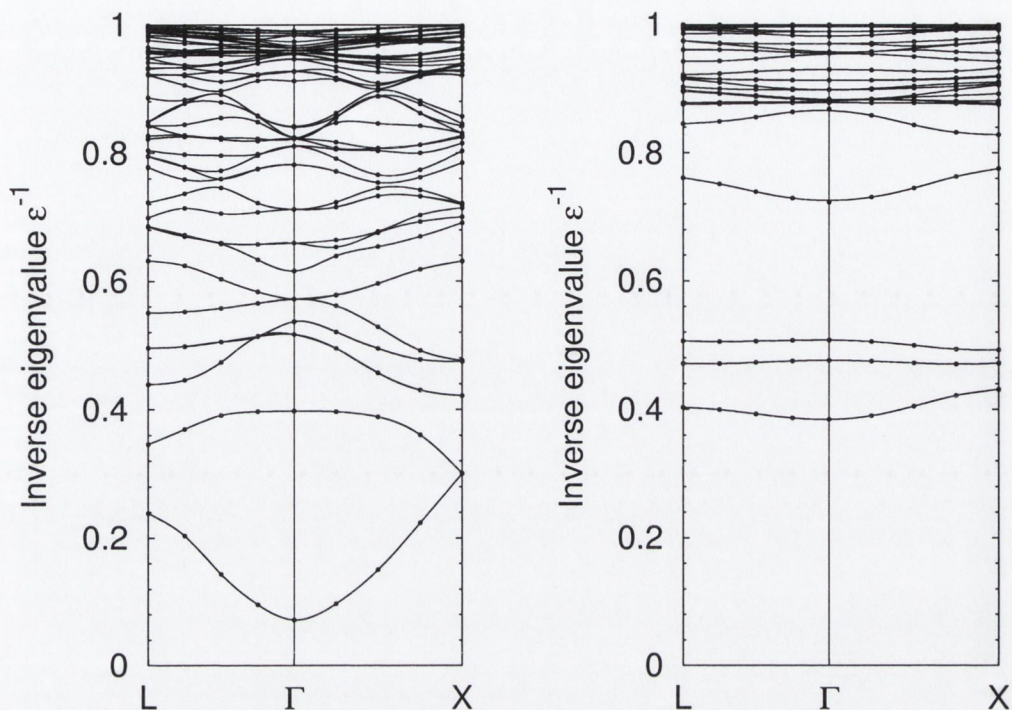


**Figure B.1:** DBS for bulk Si (left) and FCC Ar (right)

real space as a set of eigenfunctions of the response function,  $P(\mathbf{q})$  [121].

Several of the most screened dielectric eigenpotentials and response eigenfunctions, at the  $\mathbf{q} \rightarrow 0$  limit, for Si and FCC Ar are shown in Figures B.2-B.4. These are presented as contour plots; positive values are indicated by solid lines and negative values by dashed lines. The corresponding eigenvalues are tabulated in Table B.4.

The most screened eigenpotential in silicon with eigenvalue  $\varepsilon_1^{-1} = 0.071$  has a bond-centred dipolar character, (top-left panel, Figure B.2) . The arrow on the panel indicates the dipole direction on the bond. The response eigenfunction for this mode has a similar character to the eigenpotential, with an extra node on atomic sites (Figure B.3, top-left panel). The next mode is approximately monopolar and atom-centred, in both, the eigenpotential and the response eigenfunction, but changes sign on going from one atomic site to the other, (bottom-left panels, Figures B.2, B.3). It can be interpreted as one in which charge is transferred between atomic centers. Two panels on the right correspond to  $\varepsilon_3^{-1} = 0.517$  and  $\varepsilon_4^{-1} = 0.537$  eigenvalues and they are the most screened transverse

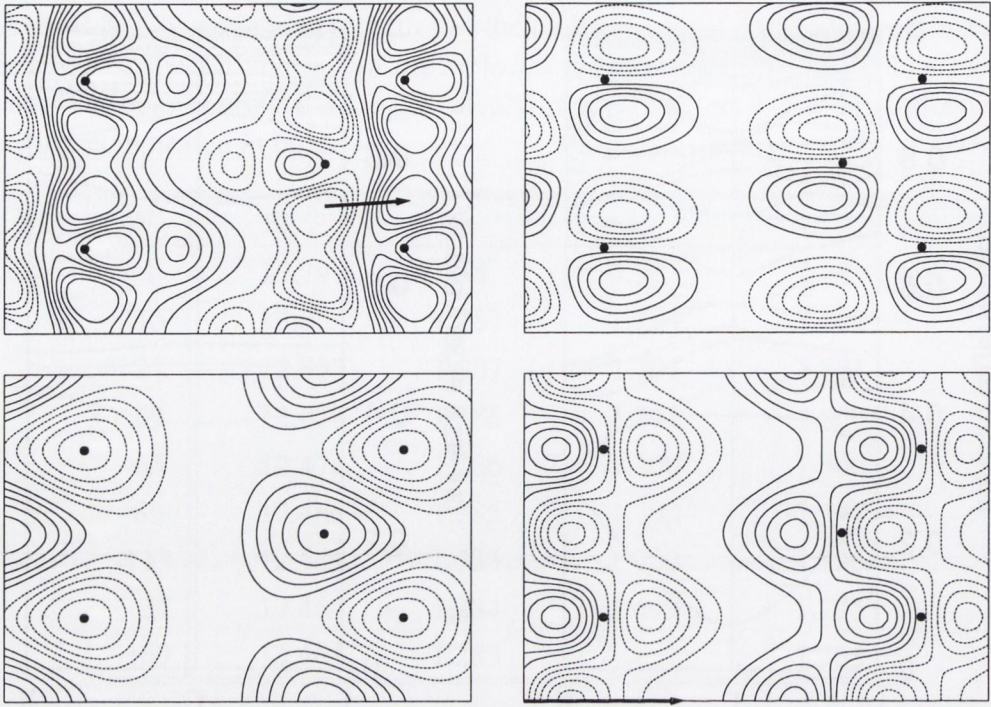


**Figure B.2:** First four the most screened dielectric eigenpotentials for Si at  $\mathbf{q} \rightarrow 0$ , plotted in  $[01\bar{1}]$  plane, conventional cell. Atomic sites are indicated by circles and an arrow on the bottom-right panel indicate  $\mathbf{q}$  direction.

(T) and longitudinal (L). Eigenpotentials and the response eigenfunctions also show the same pattern for this mode.

The DBS of Ar (Figures B.1, right) shows that four eigenpotentials in Ar are the most important in screening. The most screened eigenpotential,  $\varepsilon_1^{-1} = 0.384$ , and response eigenfunction are monopolar, atom-centred functions (top panels, Figures B.4). In this mode the charge expands and contracts almost spherically in response to an external potential of that symmetry. The next two modes have dipolar longitudinal (L) character which corresponds to  $\varepsilon_2^{-1} = 0.476$  (middle panels, Figures B.4) and doubly degenerate transverse (T) with eigenvalue  $\varepsilon_3^{-1} = 0.508$  (bottom panels, Figures B.4). The fourth eigenpotential is longitudinal, dipolar in character and atom-centered with a radial node on bonds (not shown).

The most important eigenpotentials and response eigenfunctions in the two solids are similar in character and consist of the monopolar and dipolar functions located either

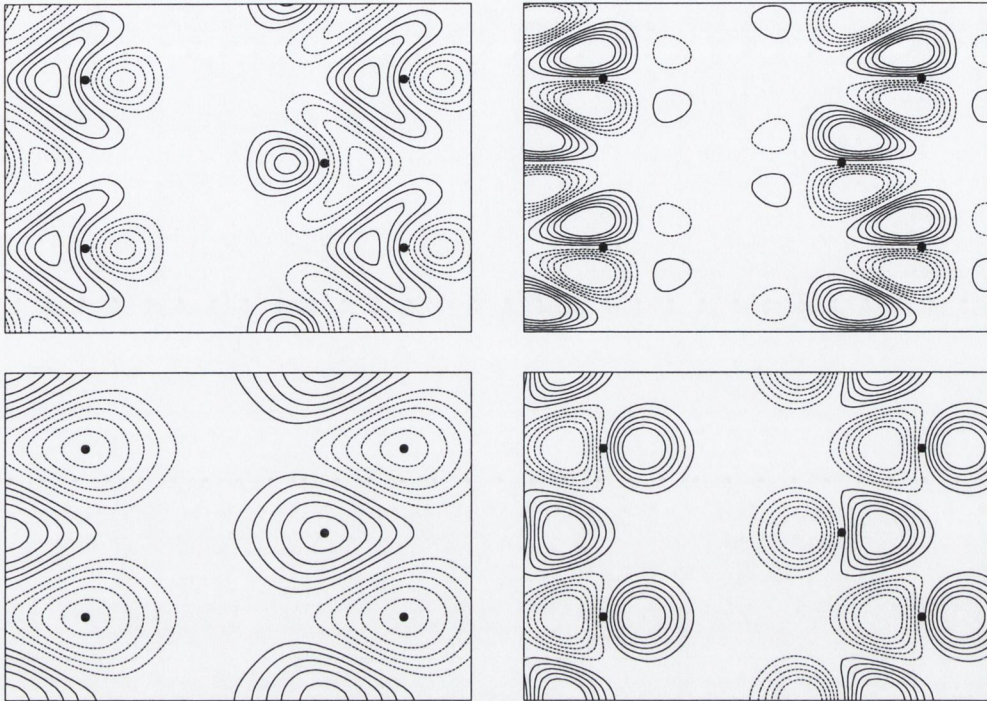


**Figure B.3:** The response eigenfunctions which correspond to eigenpotentials displayed at Figure B.2

on atom centres (Ar, Si) or bond centres (Si). That lends credence to the *ansatz* of the discrete dipole model which locates the dipole polarisabilities located on bond or atom sites.



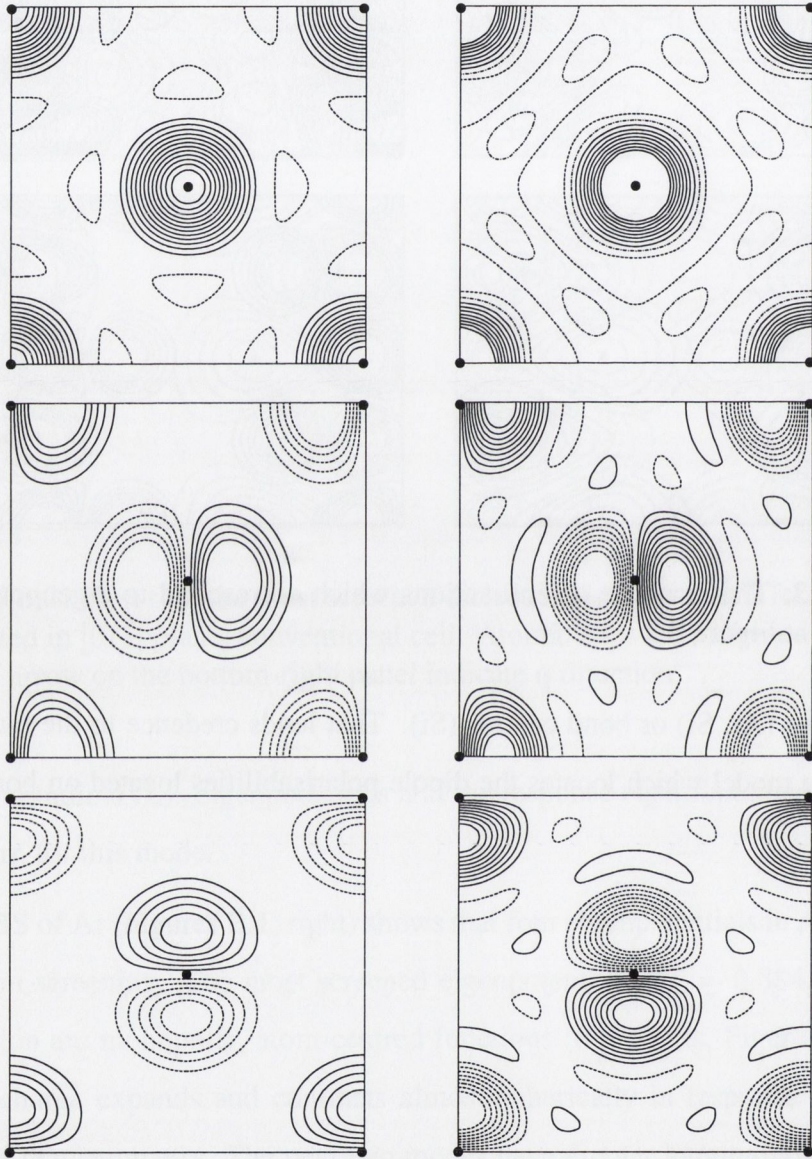


**Figure B.4:** Three the most screened dielectric eigenpotentials (left) and corresponding response eigenfunctions (right) calculated at  $\mathbf{q} \rightarrow 0$  for FCC Ar and plotted in [001] plane, conventional cell

# Appendix C

## Gaussian Orbital Basis Set

### C.1 Optical Properties and GO Basis Set

As was discussed in Chapters 3 and 4 we adopt the Linear Combination of Atomic Orbitals (LCAO) approach to expand the single-particle wave functions,  $\psi_i(\mathbf{r}, \mathbf{k})$ . In this approach,  $\psi_i(\mathbf{r}, \mathbf{k})$  is defined as a linear combination of single-particle Bloch functions,  $\phi_\mu(\mathbf{r}, \mathbf{k})$

$$\psi_i(\mathbf{r}, \mathbf{k}) = \sum_{\mu} a_{\mu i}(\mathbf{k}) \phi_{\mu}(\mathbf{r}, \mathbf{k}). \quad (\text{C.1})$$

Each  $\phi_\mu(\mathbf{r}, \mathbf{k})$  is expanded over the crystal lattice vectors,  $\mathbf{R}$  and defined in terms of atomic orbitals,  $\varphi_\mu(\mathbf{r})$

$$\phi_{\mu}(\mathbf{r}, \mathbf{k}) = \sum_{\mathbf{R}} \varphi_{\mu}(\mathbf{r} - \mathbf{A}_{\mu} - \mathbf{R}) e^{i\mathbf{k}\cdot\mathbf{R}}. \quad (\text{C.2})$$

The atomic orbitals,  $\varphi_\mu$  are given as the Gaussian Type Functions (GTF). A single exponent can be used for each  $\varphi_\mu$ , however it is more efficient to use the linear combination of individually normalised Gaussians, known as a contraction, where the Gaussians are grouped into shells of a same type i.e.  $s$ ,  $p$ ,  $d$ -type

$$\varphi_{\mu}(\mathbf{r} - \mathbf{A}_{\mu} - \mathbf{R}) = \sum_j^{n_G} d_j G[a_j; \mathbf{r} - \mathbf{A}_{\mu} - \mathbf{R}]. \quad (\text{C.3})$$

The construction and use of an appropriate basis set constitutes a critical factor in most *ab initio* calculations, but is particularly important within the Gaussian orbital framework. There is no single criterion that may be used to construct an adequate (complete) Gaussian orbital basis set. A basis which minimises the total energy of the ground state

may be sufficient for most physical applications, however this is a weak criterion for constructing virtual states and for calculation of many-body effects such as self-energy or dielectric function. Assuming that the accurate calculation of the the optical properties requires at least a reasonable value for the total energy we have chosen a few all-electron different Gaussian orbital basis sets and a pseudopotential (PP) basis set (for silicon) created from  $s$ ,  $p$  and  $d$ -type primitives.

A look at the eigenenergies will give us additional criteria and suitability of particular basis sets. As the index,  $n$ , of the conduction band increases, the energy  $E(n)$  of that state would be expected to approach the theoretical free electron result given by,

$$E(n) = \frac{1}{2} \left( \frac{6\pi^2}{V} \right)^{\frac{2}{3}} n^{\frac{2}{3}}, \quad (\text{C.4})$$

because electrons occupying energy states far above the band gap tend to become delocalised and their wavefunctions become free electron-like.  $V$  indicates the volume of the primitive cell.

Figures C.1-C.3 show how different basis sets satisfy the condition (C.4). The figures illustrate the problem of incompleteness that arises when a Gaussian orbital basis set is used. The number of effective conduction band states in the calculation of the optical properties is limited by the number of states which lie below the free-electron line, and the sum over states in Equations (3.36) and (5.8) can be truncated at that limit ('cut-off' index). So according to Figure C.1 there are only about 10 conduction bands that contribute to the sums for the smallest highly optimised basis set 42 AO, about 22 for 52 AO basis set and so on. There are 45 effective virtual states for the largest 88 AO basis set for silicon.

To increase the number of effective conduction bands one should describe the correct multi-nodal character of the higher bands (i.e.  $4d, \dots 5f, \dots$ etc.). This can be done by including  $f$  and  $g$ -type functions into the basis set as well. As an alternative, we added an extra set of orbitals located at interstitial sites to the basis. This improves the flexibility of the basis set through the cell and attempts to reproduce the highly nodal structure of the free-electron eigenstates. However, this type of set is found to be difficult to optimize and sometimes is difficult to converge during the self-consistent DFT or HF calculation.

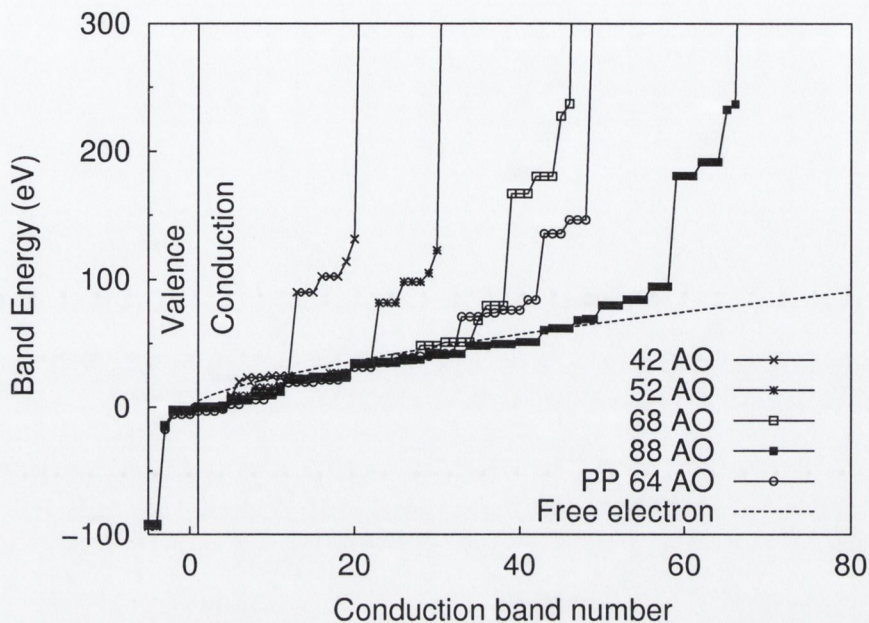


**Figure C.1:** Dependence of energy eigenvalues on conduction band number for different basis sets for Si. The energies shown are eigenvalues at  $\Gamma$  point and the zero level is aligned with bottom of the valence band. The labels in the plot indicate numbers of atomic orbitals (AO) available for particular basis set. Label PP stands for pseudopotential basis set

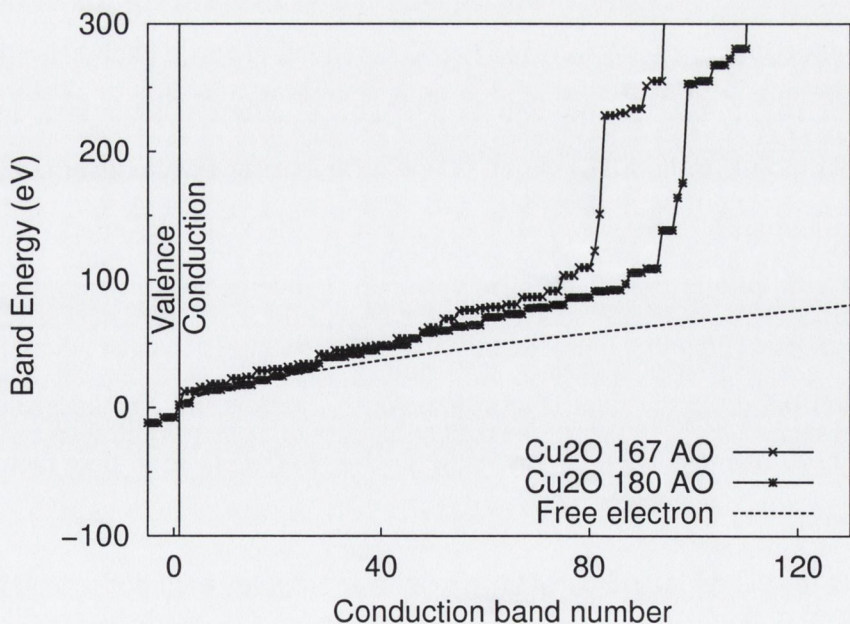


**Figure C.2:** Dependence of energy eigenvalues on conduction band number for different basis sets for  $\text{Cu}_2\text{O}$  (see Figure C.1).

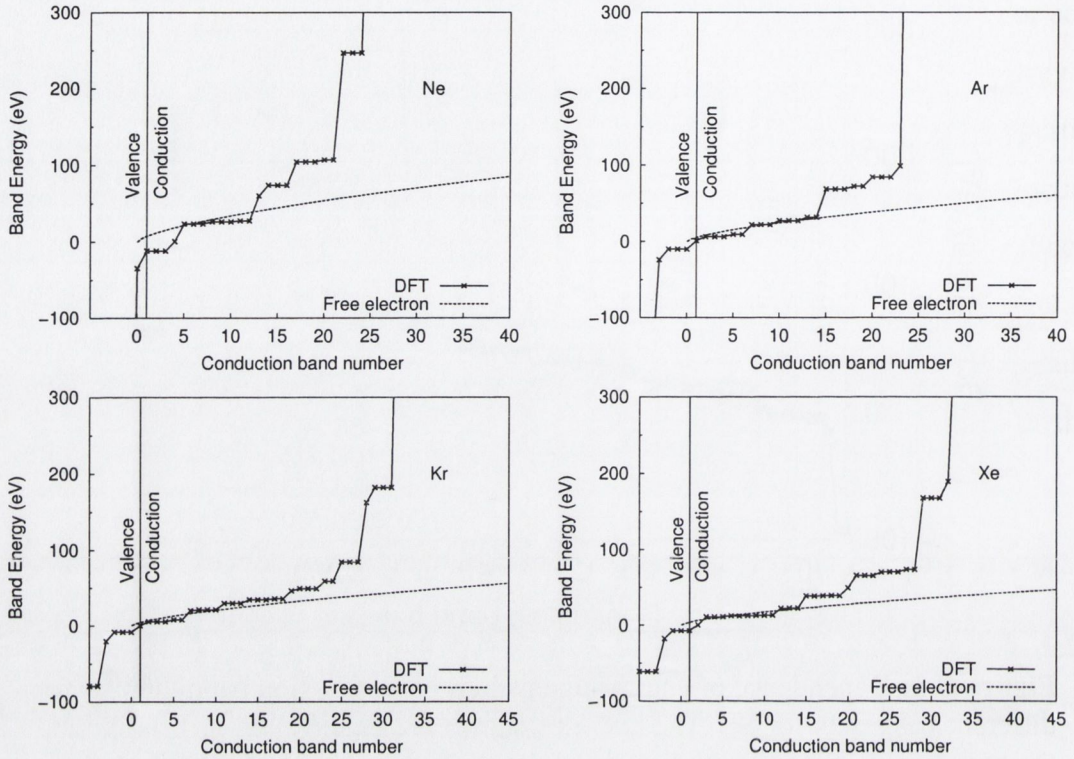


**Figure C.3:** Energy eigenvalues vs. conduction band number for the RGS.

To examine this further, we calculated the RPA dielectric matrix (5.8) as a function of number of conduction bands for Si using two different all electron basis sets: the highly optimised, labeled 52 AO and the largest, 88 AO set. These calculations are carried out using 256  $k$ -point in the FBZ, which is not sufficient for fully converged dielectric matrix and optical spectra, however in the context of the  $GW$  self-energy calculation with plasmon-pole model this mesh gave sufficient convergence to generate plasmon-pole parameters (see Chapters 3 and 4). Also, it has been suggested elsewhere [6] to use this mesh when the dielectric matrix is calculated in order to obtain the plasmon-pole parameters. Thus this mesh was used in Section 4.1.3 for the plasmon-pole factors and is used here as well.

The results for the dielectric constant,  $\epsilon_0$  (with local fields included), head of the dielectric matrix,  $\epsilon_{00}$ , one 'wing' element  $\epsilon_{111,000}$  and 'body' element  $\epsilon_{111,111}$  are presented on Figures C.4 and C.5. Again, these figures confirm that only states which lie below the free-electron ('cut-off') line (see Figure C.1) contribute to the calculation of the optical

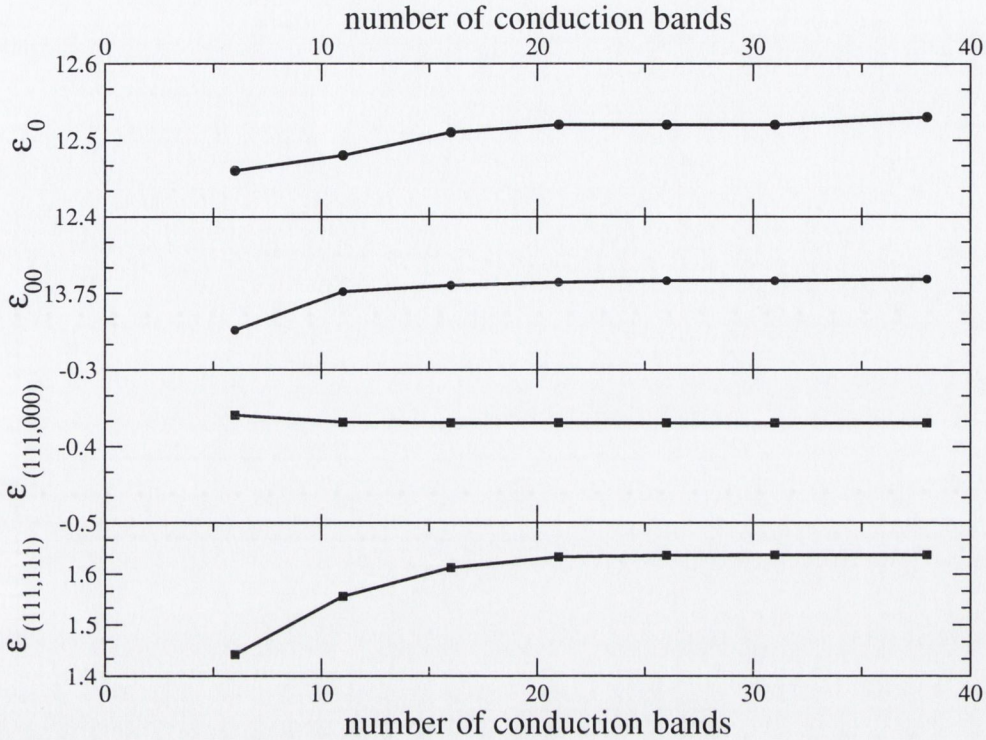


**Figure C.4:** Dielectric constant,  $\epsilon_0$  and some selected dielectric matrix elements for Si as a function of number of conduction bands for 52 AO all electron basis set.

properties. Figure C.4 illustrates relatively poor convergence of the dielectric constant, and dielectric matrix elements with respect to the number of conduction bands in the region below the 'cut-off' index, which is 20 for 52 AO basis set (see Figure C.1). So highly optimised basis sets, such as 52 AO or 42 AO, which are more than sufficient for calculation of many ground state properties, are not adequate for the calculation of the optical properties when virtual states are summed. This is not surprising, since there are very few effective unoccupied states, which contribute in summation of the dielectric matrix and self-energy.

Some improvement was achieved with the 88 AO basis set, which is generated by adding interstitial functions. Figure C.5 shows good convergence of dielectric constants and matrix elements for about 30 conduction bands taken into calculation. Also, the direct and fundamental gap was converged for only 30 conduction bands used in the summation (3.36), and the results are close to the plane wave results (see Section 4.1.3

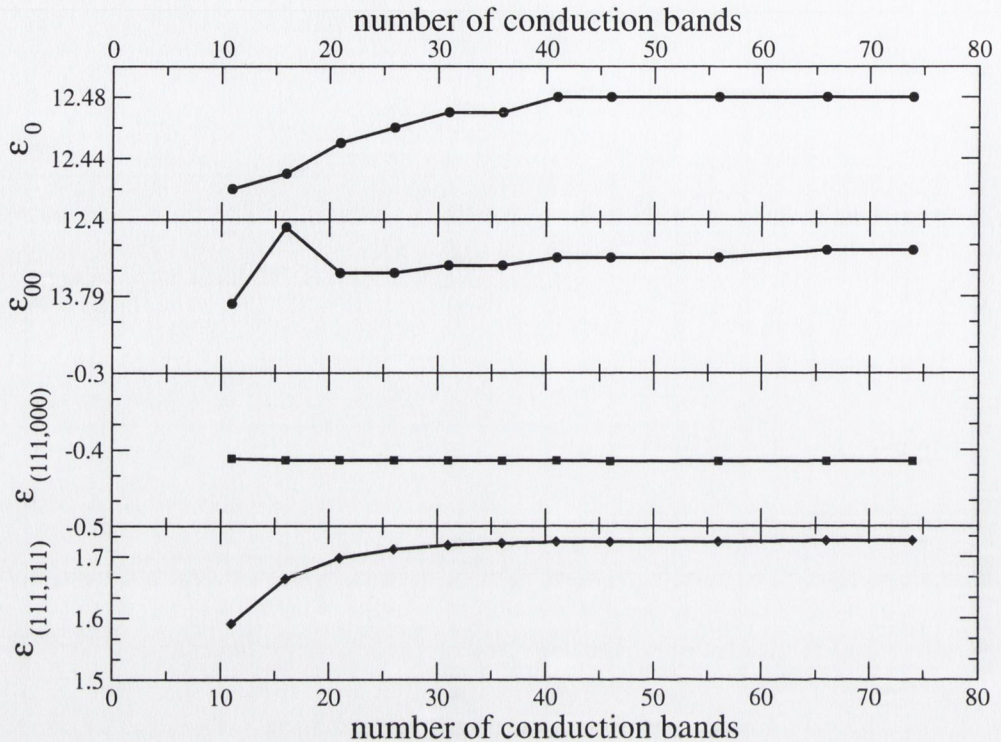


**Figure C.5:** As Figure C.4 for the largest, 88 AO all electron basis set for Si.

and Figure 4.2). The two largest basis sets, all-electron labeled 88 AO and pseudopotential, PP 64 AO have only 45 and 35 effective virtual states, respectively, however they showed up as sufficient to obtain the *GW* quasiparticle band-structure that agrees well with highly converged plane-wave calculations, Section 4.1.3.

According to the analysis we made for silicon, and Figures C.1 and C.3, one can conclude that there are only about 100 effective conduction bands which we used for  $\text{Cu}_2\text{O}$ , 30 for Ne and Ar, and 45 for Kr and Xe.

## C.2 Optimisation and Basis Set Tables

We highlighted the importance of using a large and good quality basis set for calculation of optical properties in the previous section. Extreme care must be taken when using newly developed or altered basis sets. In each case, the basis set should be tested thoroughly before use.

There are several resources where basis sets can be found, and most of them are usu-

ally sufficient for most purposes for ground state calculations. The Pople STO-nG are built into CRYSTAL95/98 code and they can be printed out and altered. The wide range of basis sets can be ordered from:

Basis Set Database [122] at:

<http://www.emsl.pnl.gov/forms/basisform.html>.

In addition, many different basis sets are offered at the CRYSTAL development homepage at:

[http://www.crystal.unito.it/Basis\\_Sets/ptable.html](http://www.crystal.unito.it/Basis_Sets/ptable.html),

and Mike Towler's CRYSTAL resources page at:

<http://www.tcm.phy.cam.ac.uk/~mdt>

Standard basis sets found in any of these resources or taken from the CRYSTAL95/98 data base must be altered for the calculation of the optical properties. To generate an improved set with extended set of states one must use the following procedure:

1. The outermost valence shells have to be uncontracted and their exponents optimised with respect to the total energy and to the band gap. Optimisation was done by hand in this work.
2. Polarisation functions should be added, if not already present, and outermost functions reoptimised.
3. If the number of basis functions is still not sufficient, 'ghost' orbitals can be added interstices. This could increase the number of basis functions dramatically, depending on the point group. Care should be taken when choosing coordinates for the new orbitals. This set should be reoptimised.
4. As a final check, the *GW* band structure should be calculated using the keyword **QP\_BANDS** in the `smexciton` executable (see Appendix A.1.4). A poor basis set will very often result in either too large or too small *GW* quasiparticle corrections of the DFT (or HFA) band structure.



A comprehensive guide to the use and optimisation of the basis sets in CRYSTAL95 can be found in [123].

**Notation:** Basis set are referred to by the number of Gaussian primitives in each contraction. A dash separates the core functions from the valence functions and polarisation functions are indicated by brackets. 'X[spd]' denotes a ghost atom with *s*, *p* and *d* orbitals.

### Silicon

All-electron basis sets used for silicon have been already used and documented in [42] with following notation:

42 AO	8-1111G
52 AO	8-1111G(d)
68 AO	8-1111G(d)+X[sp]
88 AO	8-1111G(d)+X[spd]

Pseudopotential basis set, PP 64 AO for Silicon is generated using Hay and Wadt Large core built in the CRYSTAL95/98 code and *s*, *p*, and *d* orbitals, each with decay constants 0.18, 0.4 and 0.8 in atomic units.

### Cu<sub>2</sub>O

8-411(d)/864-4111(d) - basis set with 167 atomic orbitals

Fractional coordinates - O: (0.25, 0.25, 0.25); Cu: (0, 0, 0)

8	5	OXYGEN BASIS
0	0	8 2.0 1.0
8020.0		0.00108
1338.0		0.00804
255.4		0.05324
69.22		0.1681
23.90		0.3581
9.264		0.3855
3.851		0.1468
1.212		0.0728

0	1	4	8.0	1.0	
49.43			-0.00883		0.00958
10.47			-0.0915		0.0696
3.235			-0.0402		0.2065
1.217			0.379		0.347
0	1	1	0.0	1.0	
0.470			1.0		1.0
0	1	1	0.0	1.0	
0.170			1.0		1.0
0	3	1	0.0	1.0	
0.45			1.0		
29	8		COPPER BASIS		
0	0	8	2.0	1.0	
398000.0			0.000227		
56670.0			0.001929		
12010.0			0.01114		
3139.0			0.05013		
947.2			0.17031		
327.68			0.3693		
128.39			0.4030		
53.63			0.1437		
0	1	6	8.0	1.0	
1022.0			-0.00487		0.00850
238.9			-0.0674		0.06063
80.00			-0.1242		0.2118
31.86			0.2466		0.3907
13.33			0.672		0.3964
4.442			0.289		0.261
0	1	4	8.0	1.0	
54.7			0.0119		-0.0288
23.26			-0.146		-0.0741
9.92			-0.750		0.182
4.013			1.031		1.280
0	1	1	0.0	1.0	
1.582			1.0		1.0
0	1	1	0.0	1.0	
0.559			1.0		1.0
0	3	4	10.0	1.0	
48.54			0.031		
13.55			0.162		
4.52			0.378		
1.47			0.459		

```

0 3 1 0.0 1.0
0.430 1.0
0 3 1 0.0 1.0
0.230 1.0

```

8-411(d)/864-4111(sp<sup>d</sup>) set with 180 atomic orbitals is added an extra *s* and *p* type functions on Cu sites with decay constant 0.25. The oxygen basis and the other functions of the copper basis are identical to those above.

### Neon

Durand pseudopotential basis set is used for Ne with following configuration for valence electrons and polarisation functions:

```

0 1 3 8.0 1.0
19.00 -0.1094 0.1244
 4.530 -0.1289 0.5323
 1.387 1.0 1.0
0 1 1 0.0 1.0
 1.537 1.0 1.0
0 1 1 0.0 1.0
 0.437 1.0 1.0
0 1 1 0.0 1.0
 0.247 1.0 1.0
0 3 1 0.0 1.0
 1.5 1.0
0 3 1 0.0 1.0
 0.4 1.0

```

### Argon

```

86-11111(dd)
18 9
0 0 8 2.0 1.0
135320.0 0.000225
19440.0 0.00191
 4130.0 0.01110
 1074.0 0.04989
  323.4 0.1703
  111.1 0.3683
   43.4 0.4036
   18.18 0.1459

```

0	1	6	8.0	1.0		
324.8			-0.00763		0.00820	
73.0			-0.0829		0.0605	
23.71			-0.1046		0.2115	
9.138			0.2540		0.3765	
3.930			0.695		0.3967	
1.329			0.399		0.186	

0	1	1	8.0	1.0		
0.2			1.0			1.0
0	1	1	0.0	1.0		
0.39			1.0			1.0
0	1	1	0.0	1.0		
1.4			1.0			1.0
0	1	1	0.0	1.0		
14.0			1.0			1.0
0	3	1	0.0	1.0		
0.2			1.0			
0	3	1	0.0	1.0		
0.39			1.0			
0	3	1	0.0	1.0		
0.79			1.0			

## Krypton

Basis set generated at [122] of type STO-6G, with added interstitial functions 'X[spd]' at (0.5,0.5,0.5).

36	11					
0	0	6	2.0	1.0		
28853.7364400					0.00916360	
5290.30099100					0.04936149	
1480.03557300					0.16853830	
508.43216470					0.37056280	
197.43908780					0.41649153	
81.3163196					0.13033408	
0	1	6	8.0	1.0		
2425.79644800			-0.01325279		0.00375970	
480.12842440			-0.04699171		0.03767937	
149.22355640			-0.03378537		0.17389674	
57.41168085			0.25024179		0.41803643	
24.93393212			0.59511725		0.42585955	
11.42904540			0.24070618		0.10170830	

0	1	6	8.0	1.0		
128.49657660				-0.00794313		-0.00713936
37.00047197				-0.07100264		-0.01829277
14.55321200				-0.17850269		0.07621621
6.65131252				0.15106351		0.41450986
3.31013216				0.73549148		0.48896215
1.69995829				0.27605931		0.10588165

0	3	6	10.0	0.0		
128.49657660				0.00663343		
37.00047197				0.05958178		
14.55321200				0.24019496		
6.65131252				0.46481147		
3.31013216				0.34340923		
1.69995829				0.05389057		

0	1	6	8.0	0.0		
8.80866625				0.00377506		-0.00705207
2.83432530				-0.05585965		-0.05259505
1.21100984				-0.31929460		-0.03773450
0.60388718				-0.02764780		0.38747730
0.32595180				0.90491990		0.57916720
0.18124828				0.34062580		0.12218170

0	1	1	0.0	1.0		
5.83432530				1.0		1.0

0	1	1	0.0	1.0		
1.21100984				1.0		1.0

0	1	1	0.0	1.0		
0.60388718				1.0		1.0

0	1	1	0.0	1.0		
0.32595180				1.0		1.0

0	3	1	0.0	1.0		
0.8				1.0		

0	3	1	0.0	1.0		
0.2				1.0		

0	2					
0	1	1	0.0	1.0		

0.5				1.0		1.0
0	3	1	0.0	1.0		

0.3				1.0		
-----	--	--	--	-----	--	--

**Xenon**

976633-11111(dd)+X[spd]

54	13				
0	0	9	2.0	1.13768	
3796580.0				0.0000487	
555987.0				0.0003934	
119804.0				0.0022931	
30861.1				0.01113	
8935.91				0.04616	
2853.77				0.153675	
1014.17				0.349145	
404.235				0.430543	
170.404				0.202905	
0	1	7	8.0	1.15818	
10735.9				-0.000275	0.001075
2493.21				-0.0061041	0.0097891
767.941				-0.050989	0.057466
274.67				-0.146855	0.218886
111.819				0.104336	0.459944
52.219				0.572975	0.461107
25.4397				0.484459	0.223164
0	1	6	8.0	1.18824	
231.531				0.0065159	-0.01352
91.7816				-0.025451	-0.068249
38.1398				-0.316576	0.0045716
17.3959				-0.047196	0.837103
8.1913				0.897682	1.32771
3.92195				0.474729	0.471369
0	3	6	10.0	1.0	
414.512				0.014096	
123.928				0.097746	
46.6214				0.31137	
19.5093				0.469409	
8.79497				0.297241	
3.93506				0.05124	
0	1	3	8.0	1.0	
9.48423				-2.60248	-0.099033
5.43822				-0.639355	0.304635
2.54876				5.68511	0.701398
0	3	3	10.0	1.0	
7.19406				0.227881	
2.88277				0.576082	
1.1781				0.40614	

0	1	1	8.0	1.0
2.29001	1.0			1.0
0	1	1	0.0	1.0
1.196936	1.0			1.0
0	1	1	0.0	1.0
0.633874	1.0			1.0
0	1	1	0.0	1.0
0.256598	1.0			1.0
0	1	1	0.0	1.0
0.196936	1.0			1.0
0	3	1	0.0	1.0
0.7	1.0			
0	3	1	0.0	1.0
0.442072	1.0			
0	2			
0	1	1	0.0	1.0
0.2	1.0			1.0
0	3	1	0.0	1.0
0.45	1.0			

# Bibliography

- [1] L. Hedin, Phys. Rev. **139** (1965).
- [2] M. S. Hybertsen and S. G. Louie, Phys. Rev. Lett. **44**, 1418 (1985).
- [3] M. S. Hybertsen and S. G. Louie, Phys. Rev. B **34**, 5390 (1986).
- [4] F. Aryasetiawan and O. Gunnarsson, Rep. Prog. Phys. **61**, 237 (1998).
- [5] M. M. Rieger, L. Steinbeck, I. D. White, H. N. Rojas and R. W. Godby, Computer Phys. Commun. **117**, 211 (1999).
- [6] M. Rohlfing, P. Krüger and J. Pollmann, Phys. Rev. B **48**, 17791 (1993).
- [7] M. Rohlfing, P. Krüger and J. Pollmann, Phys. Rev. B **52**, 1905 (1995).
- [8] G. Strinati, Phys. Rev. B **29**, 5718 (1984).
- [9] W. Hanke and L. J. Sham, Phys. Rev. B **12**, 4501 (1975).
- [10] W. Hanke and L. J. Sham, Phys. Rev. Lett. **43**, 387 (1979).
- [11] S. Albrecht, L. Reining, R. Del Sole and G. Onida, Phys. Rev. Lett. **80**, 4510 (1998).
- [12] M. Rohlfing and S. G. Louie, Phys. Rev. Lett. **81**, 2312 (1998).
- [13] M. Rohlfing and S. G. Louie, Phys. Rev. B **62**, 4927 (2000).
- [14] D. R. Hartree, Proc. Comb. Phil. Soc. **24**, 89, 111, 426 (1928).
- [15] V. Fock, Z. Phys. **61**, 126 (1930).



- [16] P. Hohenberg and W. Kohn, Phys. Rev. **136** (1964).
- [17] W. Kohn and L. Sham, Phys. Rev. **140** (1965).
- [18] R. O. Jones and O. Gunnarsson, Rev. Mod. Phys. **61**, 689 (1989).
- [19] R. Dreizler and R. Gross, *Density Functional Theory* (Springer, Berlin, 1990).
- [20] C. O. Almbladh and von Barth, Phys. Rev. B **31**, 3231 (1985).
- [21] G. Mahan, *Many-Particle Physics* (Plenium Press, New York, 1990).
- [22] L. Hedin and L. Lundqvist, *Solid State Physics* (Academic Press, New York, 1969).
- [23] V. R. Sanders, R. Dovesi, C. Roetti, M. Causà, N.M. Harrison, R. Orlando, C. M. Zicovich-Wilson, *CRYSTAL98 User's Manual*, Torino (1998).
- [24] H. N. Rojas, R. W. Godby and R. J. Needs, Phys. Rev. Lett. **74**, 1827 (1995).
- [25] F. Aryasetiawan and O. Gunnarsson, Phys. Rev. B **49**, 7219 (1994).
- [26] R. Dovesi, V. R. Sanders, C. Roetti, M. Causà, N.M. Harrison, R. Orlando, E. Aprà, *CRYSTAL95 User's Manual*, Torino (1996).
- [27] S. L. Adler, Phys. Rev. **126**, 413 (1962).
- [28] W. Hanke, *Advances in Physics* **27**, 287 (1978).
- [29] M. S. Hybertsen and S. G. Louie, Phys. Rev. B **35**, 5585 (1987).
- [30] M. S. Hybertsen and S. G. Louie, Phys. Rev. B **35**, 5602 (1987).
- [31] A. J. Forsyth, T. W. Josefsson and A. E. Smith, Phys. Rev. B **54**, 14355 (1996).
- [32] G. E. Engel and B. Farid, Phys. Rev. B **46**, 15812 (1992).
- [33] M. Ehrnsperger and H. Bross, J. Phys.: Condens. Matter **9**, 1225 (1997).
- [34] S. Baroni and R. Resta, Phys. Rev. B **33**, 7017 (1986).

- [35] R. Hott, Phys. Rev. B **44**, 1057 (1991).
- [36] R. W. Godby, M. Schlüter and L. J. Sham, Phys. Rev. B **37**, 10159 (1988).
- [37] B. I. Lundqvist, Phys. Kondens. Mater **6**, 206 (1967).
- [38] W. von der Linden and P. Horsch, Phys. Rev. B **37**, 8351 (1988).
- [39] G. E. Engel and B. Farid, Phys. Rev. B **47**, 15931 (1993).
- [40] A. Baldereschi and E. Tosatti, Solid State Commun. **29**, 131 (1979).
- [41] D. L. Johnson, Phys. Rev. B **9**, 4475 (1974).
- [42] C. D. Hogan, *Localized Basis Approach to Many-Body Effects and Dielectric Response*, Ph.D. thesis, University of Dublin, Ireland (2000).
- [43] M. S. Hybertsen and S. G. Louie, Phys. Rev. B **37**, 2733 (1988).
- [44] G. Baym and L. P. Kadanoff, Phys. Rev. **124**, 287 (1961).
- [45] H. J. de Groot, P. A. Bobbert and W. vab Haeringen, Phys. Rev. B **52**, 11000 (1995).
- [46] U. von Barth and B. Holm, Phys. Rev. B **54**, 8411 (1996).
- [47] F. Bechstedt, K. Tenelsen, B. Adolph and R. Del Sole, Phys. Rev. Lett. **78**, 1528 (1997).
- [48] R. Del Sole and R. Girlanada, Phys. Rev. B **54**, 14376 (1996).
- [49] A. Schindlmayr and R. W. Godby, Phys. Rev. Lett. **80**, 1702 (1998).
- [50] P. A. M. Dirac, Proc. Cambridge Phil. Soc. **26**, 376 (1930).
- [51] J. P. Perdew and A. Zunger, Phys. Rev. B **23**, 5048 (1981).
- [52] J. P. Perdew and Y. Wang, Phys. Rev. B **45**, 13244 (1992).
- [53] P. J. Hay and W. R. Wadt, J. Chem. Phys. **82**, 270 (1985).

- [54] W. R. Wadt and P. J. Hay, *J. Chem. Phys.* **82**, 284 (1985).
- [55] J. C. Barthelat and P. Durand, *Gazz. Chim. Ital.* **108**, 225 (1978).
- [56] in *Numerical Data and Functional Relationship in Science and Technology*, edited by K.-H. Hellwege and O. Madelung (Springer, Berlin, 1982), vol. 17a and 22a of *Landolt-Börnstein, New Series, Group III*.
- [57] Ruhemann and Simon, *Z. Physk. Chem. Leipzig* p. 389 (1931).
- [58] D. G. Henshaw, *Phys. Rev.* **111**, 1470 (1958).
- [59] D. R. Sears and H. P. Klug, *J. Chem. Phys.* **37**, 3002 (1962).
- [60] H. J. Monkhorst and J. D. Pack, *Phys. Rev. B* **13**, 5188 (1976).
- [61] F. Gygi and A. Baldereschi, *Phys. Rev. B* **34**, 4405 (1986).
- [62] B. Arnaud and M. Alouani, *Phys. Rev. B* **62**, 4464 (2000).
- [63] V. Sanders, *Methods in Computational Physics* (Reidel, 1983).
- [64] J. E. Ortega and F. J. Himpsel, *Phys. Rev. B* **47**, 2130 (1993).
- [65] W. E. Spicer and R. C. Eden, in *Proc. 9<sup>th</sup> Int. conf. on the Phys. of Semiconductors*, edited by S. M. Ryvkin (Hanka, Moskow, 1968), vol. 17a, p. 68.
- [66] D. Stranb, L. Ley and F. J. Himpsel, *Phys. Rev. Lett.* **54**, 142 (1985).
- [67] R. Hulten and N. G. Nilsson, *Solid State Commun.* **18**, 1341 (1976).
- [68] N. Hamada, M. Hwang and A. J. Freeman, *Phys. Rev. B* **41**, 3620 (1990).
- [69] S. Lebègue, B. Arnaud, M. Alouani and P. E. Bloechl, *Phys. Rev. B* **67**, 155208 (2003).
- [70] M. L. Tiago, S. Ismail-Beigi and S. G. Louie, arXiv:cond-mat/0307181 v1 (2003).

- [71] N. C. Bacalis, D. A. Papaconstantopoulos and W. E. Pickett, *Phys. Rev. B* **38**, 6218 (1988).
- [72] W. E. Pickett and C. S. Wang, *Phys. Rev. B* **30**, 4719 (1984).
- [73] A. B. Kunz and D. J. Mickish, *Phys. Rev. B* **8**, 779 (1973).
- [74] K. F. Niebel and J. A. Venables, in *Rare Gas Solids*, edited by M. L. Klein and J. A. Venables (Academic Press, London, 1976), p. 571.
- [75] M. Runne and G. Zimmerer, *Nucl. Instr. and Meth. in Phys. Res. B* **101**, 156 (1995).
- [76] N. Schwentner, F.-J. Himpsel, V. Savle, M. Skibowski, W. Steinmann and E. E. Koch, *Phys. Rev. Lett.* **34**, 528 (1975).
- [77] B. Sonntag, in *Rare Gas Solids*, edited by M. L. Klein and J. A. Venables (Academic Press, London, 1976), pp. 1022–1117.
- [78] E. Ruiz, S. Alvarez, P. Alemany and R. A. Evarestov, *Phys. Rev. B* **56**, 7189 (1997).
- [79] A. F. Wells, *Structural Inorganic Chemistry* (Clarendon Press, Oxford, 1984), 3rd ed.
- [80] Ch. Uihlein, D. Fröhlich and R. Kenklies, *Phys. Rev. B* **23**, 2731 (1981).
- [81] G. M. Kavoulakis, Y.-C. Chang and G. Baym, *Phys. Rev. B* **55**, 7593 (1997).
- [82] L. Kleinman and K. Mednick, *Phys. Rev. B* **21**, 1549 (1980).
- [83] J. P. Dahl and A. C. Switendick, *J. Phys. Chem. Solids* **27**, 931 (1966).
- [84] J. Robertson, *Phys. Rev. B* **28**, 378 (1983).
- [85] W. Y. Ching, Y.-N. Xu and K. W. Wong, *Phys. Rev. B* **40**, 7684 (1989).
- [86] U. Müller, *Inorganic Structural Chemistry* (Wiley, Chichester, 1993).

- [87] R. Restori and D. Schwarzenbach, *Acta Crystallogr. Sec B* **42**, 201 (1986).
- [88] R. W. G. Wyckoff, *Crystal Structures*, vol. 1 (Wiley, New York, 1965).
- [89] J. Ghijsen, L. H. Tjeng, J. van Elp, H. Eskes and M. T. Czyzyk, *Phys. Rev. B* **38**, 11322 (1988).
- [90] J. D. Jackson, *Classical Electrodynamics* (Wiley, 1975), 2nd ed.
- [91] J. Lindhard, *Mat.-fys. Medd.* **28**, 8 (1954).
- [92] N. Wiser, *Phys. Rev.* **129**, 62 (1963).
- [93] H. Ehrenreich and M. L. Cohen, *Phys. Rev.* **115**, 786 (1959).
- [94] A. Baldereschi and E. Tosatti, *Phys. Rev. B* **17**, 4710 (1978).
- [95] A. L. Fetter and J. D. Walecke, *Quantum Theory of Many-Body Systems* (McGraw-Hill Inc., New York, 1971).
- [96] W. Hanke and L. J. Sham, *Phys. Rev. B* **21**, 4656 (1980).
- [97] R. Del Sole and E. Fiorino, *Phys. Rev. B* **29**, 4631 (1984).
- [98] Z. Levine and D. Allan, *Phys. Rev. B* **43**, 4187 (1991).
- [99] M. Rohlfing, *Habilitationsschrift zur Erlangung der Lehrberechtigung im Fach Physik, Westfälischen Wilhelms-Universität Münster* (2000).
- [100] B. Arnaud and M. Alouani, *Phys. Rev. B* **63**, 085208 (2001).
- [101] D. E. Aspnes and A. A. Studna, *Phys. Rev. B* **27**, 985 (1983).
- [102] G. Gilat and L. J. Raubenheimer, *Phys. Rev.* **144**, 390 (1966).
- [103] W. Andreoni, M. Altarelli and F. Bassani, *Phys. Rev. B* **11**, 2352 (1974).
- [104] W. Andreoni, F. Perrot and F. Bassani, *Phys. Rev. B* **14**, 3589 (1976).
- [105] J. Hermanson, *Phys. Rev.* **150**, 660 (1966).

- [106] U. Rössler and O. Schütz, *Phys. Stat. Solidi B* **65**, 1973 (1966).
- [107] M. Altarelli and B. F. Bassani, *J. Phys. C* **4** (1971).
- [108] H. H. v. Grünberg and H. Gabriel, *J. Chem. Phys.* **103**, 6040 (1995).
- [109] G. Grosso, L. Martinelli and G. Pastori Parravicini, *Solid State Commun.* **25**, 435 (1978).
- [110] L. Martinelli and G. Pastori Parravicini, *J. Phys. C* **10** (1977).
- [111] V. Saile and E. E. Koch, *Phys. Rev. B* **20**, 784 (1979).
- [112] P. Laporte, J. L. Subtil, U. Asaf, S. Wind and I. T. Steinberger, *Phys. Rev. Lett.* **45**, 2138 (1980).
- [113] P. Laporte, J. L. Subtil, R. Reininger, V. Saile, S. Bernstroff and I. T. Steinberger, *Phys. Rev. B* **35**, 6270 (1987).
- [114] A. C. Sinnock and B. L. Smith, *Phys. Rev.* **181**, 1297 (1969).
- [115] J. Chen, Z. Levine and J. W. Wilkins, *Appl. Phys. Lett.* **66**, 1129 (1995).
- [116] V. Olevano and L. Reining, *Phys. Rev. Lett.* **86**, 5962 (2001).
- [117] J. D. Nuttall, T. E. Gallon, M. G. Devey and J.A. D. Matthew, *J. Phys. C* **8**, 445 (1975).
- [118] M. Springer, F. Aryasetiawan and K. Karlsson, *Phys. Rev. Lett.* **80**, 2389 (1998).
- [119] R. Kouba, A. Taga, C. Ambrosch-Draxl, L. Nordström and B. Johansson, *Phys. Rev. B* **64**, 184306 (2001).
- [120] E. Anderson, Z. Bai, C. Bischof, S. Blackford, J. Dongarra, J. Du Croz, A. Greenbaum, S. Hammarling, A. McKenney and D. Sorensen, *LAPACK User's Guide*, Philadelphia (1999).

- [121] S. Galamić-Mulaomerović, C. D. Hogan and C. H. Patterson, *Phys. Stat. Sol.* **188**, 1291 (2001).
- [122] *Extensible computational chemistry environment basis set database version 4/17/03 as developed and distributed by the molecular sciences laboratory which is part of the pacific northwest laboratory*, P.O. Box 999, Richland, Washington (2003).
- [123] M. Towler, *The use and optimization of Gaussian basis set in periodic Hartree-Fock calculations*. (University of Torino, 1995).